UNIVERSITAT
ROVIRA I VIRGILI

Catalytic Ammonia Oxidation on Noble Metal Surfaces: A Theoretical Study

Gerard Novell Leruth

Departament de Química Física i Inorgànica

Memòria presentada per optar al
títol de Doctor en Química

UNIVERSITAT
ROVIRA I VIRGILI
Departament de Química Física i Inorgànica
C/Marcel·lí Domingo, s/n
43007 Tarragona

Josep Manuel Ricart Pla, Catedràtic de Química Física, del Departament de Química Física i Inorgànica de la Universitat Rovira i Virgili i **Javier Pérez-Ramírez** Professor d'Investigació ICREA i Responsable de Grup a l'Institut Català d'Investigació Química (ICIQ)

Fem constar que la present memòria, que porta per títol:

"Catalytic Ammonia Oxidation on Noble Metal Surfaces: A Theoretical Study"

ha estat realitzat sota la nostra direcció al Departament de Química Física i Inorgànica, en el programa de doctorat en Química Teórica y Computacional de la Universitat Rovira i Virgili pel llicenciat en Química D. **Gerard Novell Leruth** per a obtenir el grau de Doctor en Química.

Tarragona, Novembre de 2008

Prof. Josep Manuel Ricart Pla

Prof. Javier Pérez-Ramírez

A la memòria d'Antoni Novell Bofarull

"Jo ja he demostrat tot el que tenia que demostrar,

ara et toca a tu"

Antoni Novell Bofarull

Agraïments

Amb la publicació d'aquesta tesi he arribat al final d'un camí. Aquest camí no l'he fet tot sol per lo que haig d'agrair a moltes persones que m'han acompanyat durant aquests anys. Cadascú d'ells ha contribuït d'alguna manera, be directament o indirectament.

Per començar he d'agrair a la Universitat Rovira i Virgili per brindar-me l'oportunitat de realitzar aquesta tesi mitjançant una beca de recerca i també a l'Institut Català d'Investigació Química (ICIQ) per l'ajuda econòmica rebuda els últims mesos en el marc del projecte "*Diseño de Catalizadores para una Química Sostenible: Una Aproximación Integrada*" (INTECAT) (CSD2006-0003) pertanyent al Programa Consolider-Ingenio 2010. També cal esmentar el suport financer del Ministerio de Educación y Ciencia (CTQU2005-08459-C02 y CT2006-01562/PPQ) i al Govern Català (2005SGR-00104).

Especialment als directors de tesi, Prof. Josep Manel Ricart Pla i Prof. Javier Pérez Ramírez, per la seva paciència, dedicació i comprensió tant a l'hora de dirigir la tesi, com en el pla personal.

Continuaré amb els membres del departament de Química Física i Inorgànica. Prof. Rosa Caballol, Prof. Josep Maria Poblet, Dra. Mar Reguero, Dr. Carles Bo, Dr. Juan Igual, Dra. Anna Clotet, Dr. Coen de Graaf, Dr. Antoni Rodrigez, Dr. Xavier López i Dr. Jordi Carbó, per l'ajuda que m'han brindat. Així com tots els companys del departament, tant els que han compartit el despatx com Dr. Alfred Gil, Dra. Ana Valcárcel, Dr. Francisco Ample, Dr. Benjamí Martorell i Alberto Roldan, per les discussions i el bon ambient mantingut tots aquest anys. Tanmateix, no vull treure importància a la resta de companys; Dr. José Gracia, Dr. Josep Mª Campanera, Dr. Elias Daura, Dr. Joan Miquel Maestre, Dr. Elena Rodrígez, Dra. Esther Bordas, Dra. Isabel Gómez, David Taratiel, Núria Queralt, Susana Romo, Jorge Fernández, Nadya Antonova, Alex Domingo, Yannick Mercier, Ramón Valencia, Laia Vila, Igor Negodaev i Mireia Segado per tot lo que hem compartit. També als tècnics de l'àrea, els informàtics José Ortiz, Elisenda Mas i Joan Iglesias per mantenir el maquinari a punt i per l'ajuda a l'hora de programa scripts i a la Mª José Romero per l'ajuda a l'hora d'impartir les practiques al laboratori. Gràcies a ells he pogut desenvolupar i finalitzar aquesta tesi.

Agrair al Prof. R. A. Van Santen, Prof. H. Niemantsverdriet, Dr. D. Curulla, Dr. W. K. Offermans, Dr. C. Popa, Dr. D. Torres per les llargues discussions de química i a tots els que hem van fer més agradable la estada a Eindhoven. Així com el suport financer rebut per part de la Comunitat Europea a través del projecte HPC-Europa per poder realitzar l'estada a la Technische Universiteit Eindhoven (TUE).

Als professors del curs interuniversitari de Química Teòrica i Computacional realitzat a Girona per intensificar els coneixements necessaris per realitzar aquesta tesi i els futurs treballs. Per descomptat, a tots els companys per la convivència i amistat durant el curs.

A la família, Antoni Novell, Christiane Leruth, José Antonio Batán per inculcar-me els valors, el gust per l'estudi i el cuc per el món científic. Per moltes coses més, com per l'orgullosos que estan de mi, estar al meu costat a les dures i les madures. Christiane Leruth, José Antonio Batán per estar avui aquí i estan sempre. A Antoni Novell per que no esta i es la persona que més li agradaria estar. A Katia Novell, oncles, cosins i demés pel suport durant tots aquest anys. Als amics per ser com son. Per últim a Rocío Carrera i a la seva família, però sobretot a la Rocío per aguantar, suportar i confiar en mi en tot moment.

A tots, GRACIES.

Contents

1 Introduction **1**
1.1 Background 1
1.2 Objectives 7

2 Theory **9**
2.1 Born-Oppenheimer approximation 9
2.2 Density Functional Theory 10
2.3 The exchange-correlation functional 13
2.4 Modeling a surface 14
2.5 Bloch's theorem and the plane wave basis set 16
2.6 Using pseudopotentials. The PAW method 17
2.7 The VASP code 17
2.8 Vibrational frequencies 18
2.9 Transition state search 19
2.10 Chemical kinetics 23

3 Characterization of NH_x Species on Pt(100) and Pt(111) **27**
3.1 Introduction 28
3.2 Computational details 30
3.3 Results and discussion 31
3.4 Conclusions 49

4 Ammonia Dehydrogenation on Platinum Group Metals **51**
4.1 Introduction 52
4.2 Computational details 54
4.3 Results and discussion 56
4.4 Microkinetics 66
4.5 Energy relationships 69

4.6 Conclusions 70

5 Ammonia Oxidation on Pt(100) 73
5.1 Introduction 74
5.2 Computational details 76
5.3 Results and discussion 78
5.4 Conclusions 98

6 Concluding remarks 99

References 103

Resum 113
Antecedents històrics 113
Objectius 117
Conclusions 118

Chapter 1

Introduction

1.1 Background

The term catalysis was introduced in 1836 by Berzelius to describe "*the property of some substance to awake affinities, which are asleep at a particular temperature, by their mere presence and not by their own affinity*". Nowadays, the definition of catalysis is the one that proposed Ostwald (1894) based on the reaction rate: "*catalysis is the acceleration of a slowly preceding chemical reaction through the presence of a foreign substance, which may participate intermediately but is not consumed by the reaction*".

The production of nitric acid (Ostwald process; Nobel prize 1909) is one of the most important industrial processes, together with the synthesis of ammonia (Haber-Bosh process; Nobel prizes 1918 and 1931, respectively), the synthesis of Fisher-Tropsch, the polymerization of Ziegler-Natta (Nobel prizes 1963) or the oxidation of sulphur dioxide in the production of sulphuric acid, among other.[1] The Ostwald process was one of the first catalytic processes introduced at industrial scale.

The reaction was discovered and patented by Kuhlmann in 1838,[2] but it was not until 1906 when Ostwald and Brauer designed an industrial process applying the reaction of ammonia oxidation. Obviously, this process would have not been possible without the existence of the Haber-Bosh process, since one of the reactants of the Ostwald process is ammonia, the product of the mentioned process. The first stage of the Ostwald process is the catalytic ammonia oxidation. It is one of the most studied and fastest reactions. It is estimated that the contact time between the reagents (NH_3 and O_2) with the

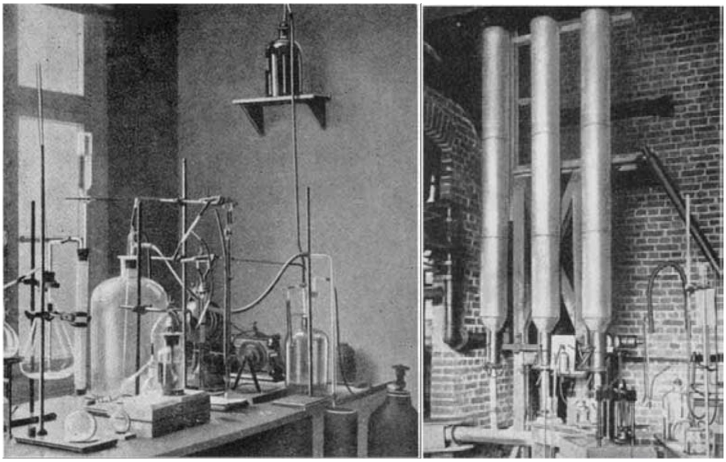

Figure 1.1: Left: Lab device used by Ostwald to investigate the ammonia oxidation. Right: Pilot plant reactor constructed by Ostwald and Brauer, 1904. Figures extracted from L.B. Hunt, Platinum Metals Rev., 1958.

catalyst (Pt/Rh) is approximately of 1 microsecond, obtaining NO, N_2, N_2O and H_2O.

The problem of the original Ostwald process was the large amount of platinum necessary to carry out the reaction. Very soon, K. Kaiser of the Technische Hochschule in Charlottenburg patented the utilization of platinum gauzes, and since then, it has been improved the catalyst yield using Pt/Rh alloys, moreover Pd is also used to recover the lost Pt during the catalyst life.[3] Nowadays, the composition is approximately 95% of Pt and 5% of Rh, although this proportion can vary with the price of the metals in the international market. The composition of the catalyst changes during the process because of Pt loss and increases the composition in Rh (segregation). Another change on the surface is the formation of cauliflowers (Figure 1.1).[4]

Many years were dedicated to the study of this reaction, to improve and understand it, as reflected in the bibliography (Figure 1.3). Around 1910s, when the Ostwald process started, there were already several publications, mainly about the development of different catalysts, which tried to improve the process yield. A major change in the catalyst occurred in the 1930s, when the beneficial effect of rhodium addition, precisely between 5% and 10%, to the platinum gauzes was discovered.[3] This discover was made by DuPont (Hansforth and Tilley, 1934).[5] From then it has not been changed the platinum/rhodium re-

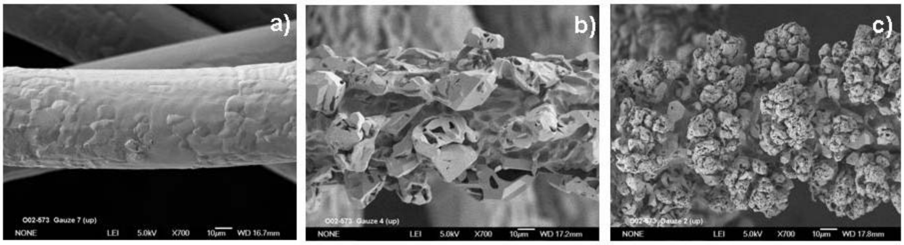

Figure 1.2: Commercial gauze at different times of the ammonia oxidation process; a) fresh gauze, b) faceted gauze, and c) cauliflowered gauze. Courtesy of Javier Pérez-Ramírez.

lation. Another interesting point is the recovery of the platinum that gets lost during the reaction. This generated more publications in the 60s. Until the new techniques associated to the current surface science and the computational methods did not appear, the publications have not increased again about this subject.

Thus, it is a process that still remains open to the discussion, for the proposed mechanisms, the improvement of the catalyst, the intermediate species or the simple understanding of the process of the whole reactivity related to the process.

During many years were made it a large quantity of experiments at very diverse work conditions. All these studies have brought a lot of information about the process or parts of this. In some cases they bring information about the behaviour of the catalyst, other the possible adsorbed species on the surface or the kinetics of the implied reactions, etc. There are three main types of experiments. The first type are the experiments made at Ultra High Vacuum (UHV) that contributed to the nature of adsorbed species, for example the NH_x species. In this group, there are many techniques and examples, as are Thermal Desorption Spectroscopy (TDS), Electron Energy Loos Spectroscopy (EELS), Auger's Electron Spectroscopy (AES) or Low Energy Electron Diffraction (LEED), etc.[6–13] These techniques are normally carried out on monocrystals, in conditions of ultra high vacuum and many times using some specific reactions. For this reason, the obtained data cannot be extrapolated to the industrial conditions, although they bring important information of the adsorbed species and their reactivity in determinate conditions. The second group of experiments to emphasize are the ones carried out with microreactors. These experiments usually analyze the products of outlet at

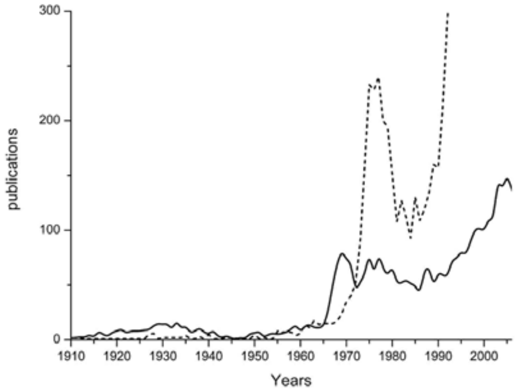

Figure 1.3: Published works related to catalyzed ammonia oxidation (black line) and catalytic nitric oxide decomposition (dashed line) interest per year. This chart is based on the database of SciFinder.

different conditions of temperature, pressure and inlet reagents. Mainly, they have been used to know the yield of the catalyst. The data obtained can be used to adjust a kinetic model as it has been done by Rebrov *et al.*[14] These experiments give us information about the catalyst behavior as a function of the operation conditions of the microreactor. Finally it is necessary to stress the Temporary Analysis of Products (TAP) technique,[15–19] taht analyzes the products of outlet in function of time with respect to a inlet pulse of reagents. This technique brings information about the kinetics of reaction, since it provides us information of the outlet products and the proportion of these against time. Each experiment explains a part of the process. Thus, the experiments carried out on crystals in ultra high vacuum (UHV) bring information about the adsorbed species and their reactivity, but they make it in conditions that are far away from the ones found in the industrial process, i.e. atmospheric pressure and with amorphous materials. The existence of this difference in material and pressure (so called materials gap and pressure gap)[19,20] difficults the extrapolation of the results to the real processes. TAP permits studies at higher pressures but do not reach the operation pressure of industrial reactor (1-12 bar), in spite of eliminating the material gap, because the industrial catalyst can be used directly.[19] Computational methods bring information about the different processes that are produced on the catalyst surface, being

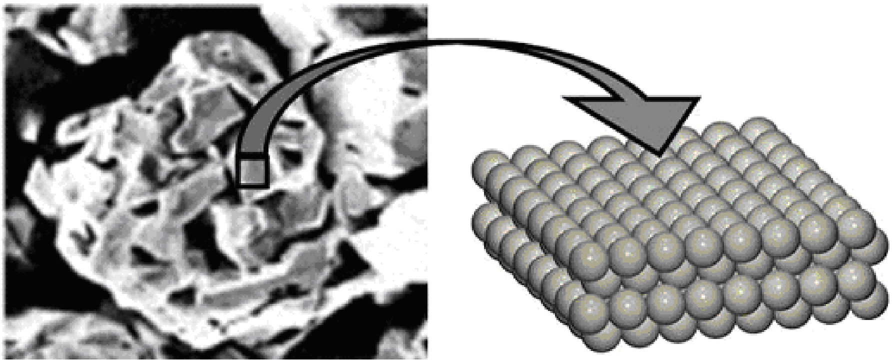

Figure 1.4: Representation of the real catalyst and the surface model.

able to unravel the reactivity of each species on the surface and determin the transition states. Thus, it can be studied all possible reaction paths, and to discriminate the minimum energy path way of the global reaction. It is equivalent to have the important fragments of the process in relation to the surface. The surface model is generally an ideal crystal, which the material gap is not erased with. As a matter of fact, with the state of the art calculation methods and the power of the current computers, a model of the real catalyst could be generated, although at a high computational cost, far from the goals of this thesis.

Although the calculation is carried out in strict vacuum and at the absolute zero of temperature, the obtained results can be used to extrapolate to atmospheric pressure and work temperature using the statistic thermodynamics and to predict the most stable intermediate species, the possible rate determining step, to elucidate the global kinetics, and the behaviour of the reaction depending on the initial conditions. To understand these phenomena and to extrapolate the results to the pressures of the real process, we can solve the system of kinetic equations of all elementary steps from results of the quantum mechanics methods. This system can be solved in different ways, one of them is based on Montecarlo methods, but we have used a classical way. Using the Transitional State Theory (TST) we convert the obtained data from the Density Functional Theory (DFT) to the classical kinetic equations as it is explained in the following chapter. The solution of this system brings us great information about the reagents and products in gas phase and the species on the surface depending on the reaction time. This information can discriminate the important elementary reactions and permits one to obtain the mechanism of the process.

This reaction is very complex for the great number of implied variables, how it can be the catalyst surface. During the process the composition of the catalyst changes, since lost the Pt and enriches in Rh (segregation). This chemical change entails a physical change, the surface area increases until the cauliflowers formation.[4] According to the surface composition, the catalyst has an activity, selectivity, and a determinate conversion. Another variable to take into account are the reaction condition, at specific temperature and pressures of the reactants inlet one obtaining different distributions of products.

Because of the reaction complexity, the information that provides the experiments is limited by the reaction conditions. The computational methods present us information based on a model, by this reason the results obtained are limited to the used model. The opportunity that the DFT methods offer us is the possibility to design all necessary models to describe all moments of the process and add all different variables previously appointed.

As already commented in the analysis of the publications, the ammonia oxidations process is still under discussion. One of the points of discussion is the reaction mechanism. During many years three possible mechanisms have been sustained to describe the process. In this thesis we have studied the three possible mechanisms, as we will see later.

1. Mechanism of nitroxyl (HNO), described by Andrussow:[21]
   - $NH_3 + O_2 \rightarrow HNO(a) + H_2O$
   - $2\ HNO(a) + 1/2\ O_2 \rightarrow 2\ NO + H_2O + 2\ *$
   - $HNO(a) + NH_3 \rightarrow N_2H_4(a) + H_2O$
   - $N_2H_4(a) + 1/2\ O_2 \rightarrow 2\ N_2 + H_2O + *$
   - $HNO_3(a) + NH_3 \rightarrow NH_4NO_3(a)$
   - $NH_4NO_3(a) \rightarrow N_2O + 2\ H_2O + *$
2. Mechanism of hydroxylamine (NH_2OH), described by Bodenstein:[22]
   - $NH_3 + O(a) \rightarrow NH_2OH(a)$
   - $NH_2OH(a) + O_2 \rightarrow HNO_2(a) + H_2O$
   - $HNO_2(a) + O_2 \rightarrow HNO_4(a)$
   - $HNO_4(a) \rightarrow NO + O_2 + OH(a)$
   - $NH_2OH(a) + O(a) \rightarrow HNO(a) + H_2O + *$
   - $NH_2OH(a) + HNO(a) \rightarrow N_2 + 2\ H_2O + 2\ *$

- $HNO(a) + HNO(a) \rightarrow N_2O + H_2O + 2$ *

3. Mechanism of imide (NH), described by Raschig and Zawadzki:[23, 24]

- $NH_3 + O(a) \rightarrow NH(a) + H_2O$
- $NH(a) + O(a) \rightarrow HNO(a) +$ *
- $NH(a) + NH_3 \rightarrow N_2H_4(a)$
- $HNO(a) + NH_3 \rightarrow N_2H_4(a) + {}^1/_2\, O_2$
- $N_2H_4(a) + O_2 \rightarrow N_2 + 2\, H_2O +$ *

1.2 Objectives

The goals that have been risen in this thesis are:

1. Structural study of the adsorption of the species NH_x (x=0-3) on the (100) and (111) surfaces of platinum. This study includes the geometry and the adsorption site, the electronic properties, the influence of the coverage and the relative stability of the species.
    (a) Study of the temperature and the pressure effect on the adsorption of ammonia on Pt(100) and Pt(111).
    (b) Spectroscopic analysis of the NH_x species (x=0-3) adsorbed on Pt(100) and Pt(111).
    (c) Study of the dissociation reaction of the species NH_x (x=0-3) on the previous surfaces.
2. A comparative study of the ammonia dehydrogenation on the (100) and (111) faces of platinum, rhodium and palladium. We emphasize the determination of rate coefficients of the different steps.
3. Study of the ammonia oxidation on Pt(100).
    (a) Characterization of all adsorbed species (NH_3, NH_2, NH, O, OH, H_2O, NH_2, HNO, NOH, N_2, NO, N_2O).
    (b) Study of the oxygen assisted dehydrogenation.
    (c) Study of the hydroxyl assisted dehydrogenation.
    (d) Comparison of the results with the (111) surface.

(e) Analysis of the feasibility of the proposed mechanisms in the literature.

(f) Study of the final products (NO, N_2, N_2O, H_2O).

(g) Microkinetic analysis of the global process and identification of the rate determining step.

These are the fundamental contents of this thesis, although some points are still open. The study of rhodium and Pt/Rh alloys is still unresolved and must be finished, because this would approximate us more to the industrial process. The results could also be translated to a reactor model, and to improve its design. We could simulate the TAP experiments and increase the knowledge of this technique to facilitate the analysis of the results. A long way to go still remains open, not only with theoretical, but also experimental works. The purpose of this thesis is to give a step to understand and to improve the process of ammonia oxidation.

Chapter 2

Theory

2.1 Born-Oppenheimer approximation

The Schrödinger equation, developed by the physicist Erwin Schrödinger in 1925-26, is the key equation of quantum mechanics. All properties of a system can be derived by solving this equation. For a system composed of N electrons and M nuclei, the equation is expressed as:

$$\widehat{H}\Psi_n\left(\{\vec{r}_i\}\left\{\vec{R}_\mu\right\}\right) = E_n\Psi_n\left(\{\vec{r}_i\}\left\{\vec{R}_\mu\right\}\right) \tag{2.1}$$

where $\widehat{H}$ is the time-independent Hamiltonian, Ψ_n is the wave function of the system associated to the energy level E_n (n accounts for the quantization of the system) and $\vec{r}_i$ and $\vec{R}_\mu$ are the spatial coordinates of the electrons and the nuclei, respectively. All properties of the electrons-nuclei system are described by equation 2.1. By solving this equation we could, therefore, obtain all the physical and chemical properties of the system (except for relativistic effects), however, this equation is too complex to be solved. For this reason, to solve the Schrödinger equation, several approximations are needed. A common way to simplify this complex equation, universally accepted in electronic structure theory, is the separation of the nuclear and the electronic motion, this is the so-called Born-Oppenheimer approximation.[25]

This approximation is based on the difference mass between nuclei and electrons. For example the hydrogen atom is 1.836 times heavier than an electron. Therefore it is possible to consider nuclear and electronic motion as independent. The electrons follow nuclei instantaneously during its motion. We can then rewrite the expression for the Hamiltonian as:

$$\widehat{H} = \widehat{T}_{nuc} + \widehat{H}_{el} \tag{2.2}$$

The electronic Hamiltonian $\widehat{H}_{el}$ depends parametrically on nuclear positions $\left(\vec{R}_{\mu}\right)$: the nuclear coordinates appear in the electronic Hamiltonian, but derivatives respect to these coordinates do not. Therefore, the electronic problem can be solved for nuclei, which are momentarily fixed in space.

$$\widehat{H}_{el}\left(r,R\right)\psi_{el}\left(r,R\right) = E_{el}\left(R\right)\psi_{el}\left(r,R\right) \tag{2.3}$$

R and r are the total set of nuclear and electronic coordinates. The total wave function can then be approximated as a product

$$\Psi_{BO}\left(r,R\right) = \psi_{nuc}\left(R\right)\psi_{el}\left(r,R\right) \tag{2.4}$$

where the nuclear wave function $\psi_{nuc}\left(R\right)$ is a solution of the equation

$$\left\{\widehat{T}_{nuc}\left(R\right)E_{el}\left(R\right)\right\}\psi_{nuc}\left(R\right) = E\psi_{nuc}\left(R\right) \tag{2.5}$$

The separation of the electronic and nuclear wave function evidently simplifies the resolution of the Schrödinger equation. Determining the total wave function of the nuclei and electrons system is reduced to determining the total electronic wave function. Nevertheless, for any chemical interesting system, the electronic part of the problem is still too difficult to be treated exactly.

First-principles quantum chemical methods are proposed to solve ab initio ('from scratch') the electronic Schrödinger equation. Ab initio methods include wave function methods (e.g. Hartree-Fock (HF), Perturbation theory (PT), Configuration Interaction (CI) theory, coupled Cluster Methods (CC)) and Density Functional Theory (DFT) methods.[26–30]

DFT methods are the best choice for the computational demands-accuracy ratio of transition metal surfaces. DFT has therefore been used for the calculations in this thesis.

2.2 Density Functional Theory

A big step towards resolving electronic Hamiltonian was established by Thomas and Fermi[28, 29] in the mid 1920s. They established that the energy of a homogeneous electron gas is a function of its electronic density. In 1964, Hohenberg and Kohn[30] showed that this principle can be generalized to any kind of electronic system and established the basis of Density Functional Theory (DFT).

For a system of N electrons and M nuclei, the electronic Hamiltonian can be written as

$$\widehat{H} = \widehat{T} + \widehat{V} + \widehat{W} \tag{2.6}$$

The first term in equation (2.6), $\widehat{T}$, is the kinetic energy arising from the motion of electrons, the second term is the potential energy of the nuclear-electron attraction, $\widehat{V}$, and the third term is the electron-electron repulsion, $\widehat{W}$. Hohenberg and Kohn proven that the ground-state molecular energy, the wave function, and all other molecular properties are uniquely determined by the exact electron density, $\rho(\vec{r})$. Consequently, the central focus of DFT is the electronic density, ρ, rather than the wave function, ψ. For a system of N electrons the density function, $\rho(\vec{r})$, is defined by

$$\rho(r) = N \int \cdots \int |\psi|^2 \, dr_1 dr_2 \cdots dr_N \tag{2.7}$$

where ψ is the electronic wave function of the system. Then

$$\int \rho(r) \, dr = N \tag{2.8}$$

DFT is based on the two Hohenberg-Kohn theorems:

Theorem 1:

The external potential $\widehat{V}$ is a unique functional of ρ; because V fixes the Hamiltonian, the particle ground state is a unique functional of ρ. Therefore, there is a direct relationship between the electronic density and the energy (and its individual parts).

$$E[\rho] = T[\rho] + V[\rho] + W[\rho] \tag{2.9}$$

$$V[\rho] = \int \rho(r) \, v(r) \, dr \tag{2.10}$$

Theorem 2:

For a trial density $\rho(\vec{r})$, such as $\rho(\vec{r}) \geq 0$ and, $\int \rho(r)\,dr = N, E_0[\rho_0] \leq E[\rho]$. In other words, the energy of the system $E[\rho]$ reaches a minimum value E_0 for the exact density ρ_0. This is the so-called variational principle.

If we take a closer look at equation (2.9), we can separate the $W[\rho]$ functional into two contributions: the classic interaction between two charge densities (Coulombic interaction) and a second term that contains the non-classical parts (eq. 2.11).

$$W\left[\rho\right] = \frac{1}{2}\iint \frac{\rho\left(\vec{r}_1\right)\rho\left(\vec{r}_2\right)}{r_{12}} d\vec{r}_1 d\vec{r}_2 + W_{NCL}\left[\rho\right] = W_{CL}\left[\rho\right] + W_{NCL}\left[\rho\right] \quad (2.11)$$

The complete energy functional can be expressed as

$$E\left[\rho\right] = T\left[\rho\right] + V\left[\rho\right] + W_{CL}\left[\rho\right] + W_{NCL}\left[\rho\right] \quad (2.12)$$

In equation (2.12) only the $V\left[\rho\right]$ and $W_{CL}\left[\rho\right]$ terms are known. To solve the problem of the kinetic energy functional, this term is split into two contributions: $T_S\left[\rho\right]$ and $T_C\left[\rho\right]$. The former is expressed as a one-particle approach (2.13) and the latter, still unknown, contains the difference between the real functional and the one particle term.

$$T_S\left[\rho\right] = \frac{1}{2}\sum_i \left\langle \psi_i \left| \nabla^2 \right| \psi_i \right\rangle \quad (2.13)$$

The equation (2.12) can be rewritten as follows

$$\begin{aligned} E\left[\rho\right] = T_S\left[\rho\right] + T_c\left[\rho\right] + V\left[\rho\right] + W_{CL}\left[\rho\right] + W_{NCL}\left[\rho\right] = T_S\left[\rho\right] + V\left[\rho\right] \\ + W_{CL}\left[\rho\right] + E_{XC}\left[\rho\right] \end{aligned} \quad (2.14)$$

where the $E_{XC}\left[\rho\right]$ or exchange-correlation functional contains all the unknown terms (all the many-body interactions).

Unfortunately, the Hohenberg and Kohn theorems do not tell us how to calculate E_0 from ρ since the exact form of the functional is not known. Kohn and Sham[31] proposed an indirect approach to this functional. In the Kohn-Sham method, the exact ground state can be found from the Kohn-Sham orbitals,

$$\rho\left(r\right) = \sum_i \left|\psi_i\left(r\right)\right|^2 \quad (2.15)$$

The Kohn-Sham orbitals are obtained from the one-electron Kohn-Sham equations

$$\int_S^{KS} \psi_i = \varepsilon_i \psi_i \quad (2.16)$$

where $\int_S^{KS}$ is

$$\int_S^{KS} = -\frac{1}{2}\nabla^2 - \int \frac{\rho\left(\vec{r}_2\right)}{r_{12}} d\vec{r}_2 + \sum_i \frac{Z_\mu}{r_{1\mu}} + v\left(r\right) \tag{2.17}$$

These equations are solved iteratively. Thus, a guess density is proposed, which is used to build the $\int_S^{KS}$, then the set of equations a resolved (2.16) and a new density obtained, which is used to build a second $\int_S^{KS}$, until self-consistency is reached. No one knows what the exact functional $E_{XC}\left[\rho\right]$ is. Finding the analytical expression of the exchange-correlation term is a major task in DFT. Some approximate functionals have been proposed.

2.3 The exchange-correlation functional

To describe $E_{XC}\left[\rho\right]$, two approximations are generally used: the Local Density Approximation (LDA) and the Generalized Gradient Approximation (GGA). LDA is based on a model called uniform electron gas.[28] This approximation assumes that the charge density varies slowly throughout a molecule so that a localized region of the molecule behaves like an uniform electron gas. The exchange-correlation energy is then expressed as a function of the exchange-correlation functional per particle of an uniform electron gas,

$$E_{XC}^{LDA}\left[\rho\left(r\right)\right] = \int \rho\left(r\right) \varepsilon_{XC}\left[\rho\left(r\right)\right] dr \tag{2.18}$$

The energy functional accounts for the local value of ρ at each point in space regardless of any other point. Vosko, Wilk and Nusair (VWN)[32] reported the first analytic expression for the correlation term within this approximation. GGA adds an additional term to the LDA exchange-correlation energy. Gradient corrections are introduced to allow exchange-correlation functional to vary (the density gradient is taken into account). $E_{XC}\left[\rho\right]$ is expressed as

$$E_{XC}^{GGA}\left[\rho\left(r\right)\right] = \int f_{XC}\left(\rho\left(r\right), \left|\nabla\rho\left(r\right)\right|\right) \rho\left(r\right) dr \tag{2.19}$$

There are many exchange-correlation expressions in the literature, for example, Perdew (P86), Becke (B86, B88), Perdew-Wang (PW91), Laming-Termath-Handy (CAM) and Perdew-Burke-Enzerhof (PBE) deal with the exchange while Perdew (P86), Lee-Yang-Parr (LYP), Perdew-Wang (PW91) and Perdew-Burke-Enzerhof (PBE) deal with the correlation.[33–39]

There is a third class of functionals in DFT called hybrid functionals, such as the popular B3LYP[40] exchange-correlation functional. These include the exact exchange energy as a contribution from the exact exchange. This approach has extensively proven its accuracy for many systems, although they are more time-demanding than non-hybrid exchange-correlation functionals because of the calculation of the two-electron integrals in the exact exchange.

We use the PW91 exchange-correlation functional for all the calculations of this thesis because of its good description of metallic systems and chemisorption thereon.[41]

2.4 Modeling a surface

The real catalyst used in ammonia oxidation processes consists of gauzes of platinum and rhodium alloy with surface defects. Modelling this complex structure at the molecular level is impossible at present. We simplify the model, reaching a model of metal crystal. But an infinite metal crystal has an infinite number of atoms. This implies that the wave function has to be calculated for each of the infinite number of electrons and the basis set in which the wave function is expressed will be also infinite. Ammonia oxidation reactions are performed mainly on the surface, therefore, we are essentially interested in metal surfaces. These systems can be modelled by two different approaches: the so-called cluster model approach,[42, 43] and the periodic slab model approach.[42, 44]

Modeling a periodic system

The finite models have extensively proven their ability to describe local properties.[45–47] The slab model is based on the band-structure theory. A bi-dimensional slab is formed by periodically repeating the geometry of the system on the x and y axes. In the z axis, the periodicity is broken with a vacuum space to create the surface (see Figure 2.4).

This periodic approach has some advantages compared to the cluster model. For example, it correctly describes materials with perfect faces as crystalline surfaces, making possible to study non local properties. Another advantage of supercell models is that they are well suited for studying the influence of the adsorbates coverage on the surface. However, to study low coverage situations with slab models we need using large supercells, with a concomitant increase in computational costs.

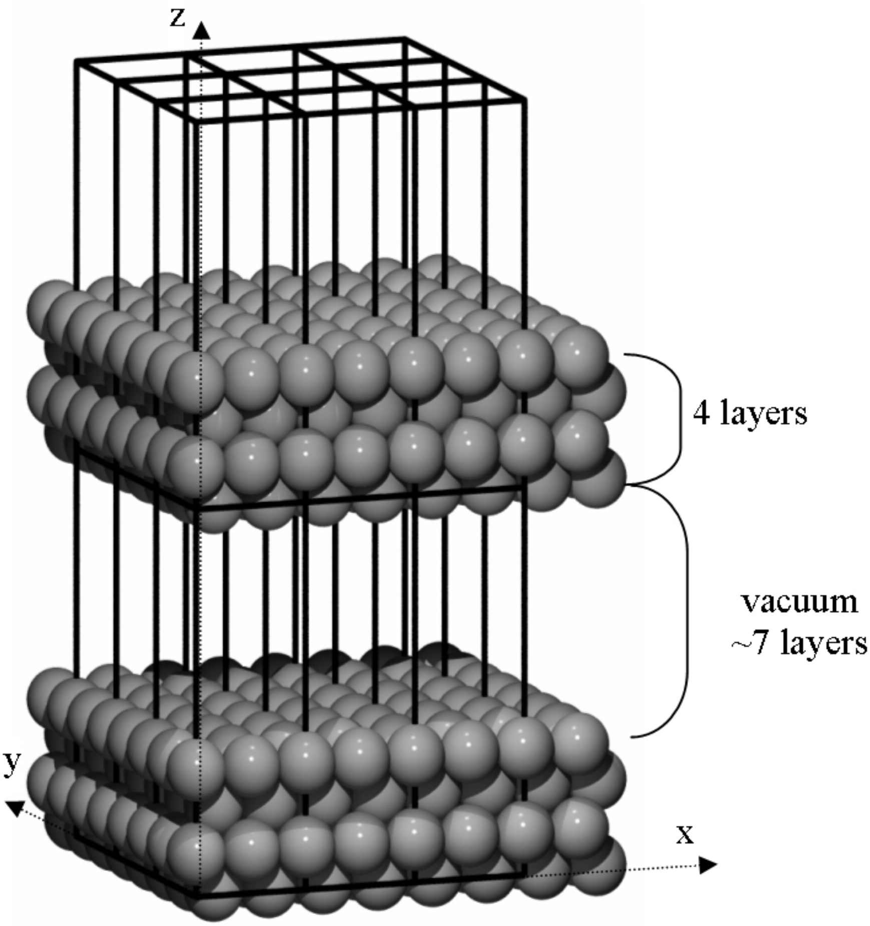

Figure 2.1: Sketch of the slab model.

2.5 Bloch's theorem and the plane wave basis set

In a perfect metallic crystal, atoms are arranged in a regular way. The periodic units of the system are all equal and can be obtained by repeating a unit cell. The definition of this unit cell is not unique. It is possible to choose the unit cell with the smallest volume, the one with the best symmetry properties. Bloch's theorem uses the periodicity of the crystal to reduce the infinite number of one-electron wave functions to be computed to the number of electrons in the unit cell of the crystal. Then we can express the one-electron wave functions as the product of a cell periodic part and a wave-like part (Bloch functions).

$$\psi_{n,\vec{k}}\left(\vec{R}\right) = \exp i\left(\vec{k}\cdot\vec{R}\right)\phi_{nBAND,\overrightarrow{k}}\left(\vec{R}\right) \tag{2.20}$$

where $\psi_{n,\vec{k}}\left(\vec{R}\right)$ is the wave function of the periodic system, $\vec{R}$ is the position in the crystal, $\vec{k}$ is a vector in the crystal reciprocal space and $\phi_{nBAND,\vec{k}}\left(\vec{R}\right)$ is a function associated with an energetic level for a periodical system (band) *nBAND*. The difficulty is then translated from the real to the reciprocal space. The infinite number of electrons is now mapped onto the problem of expressing the wave function in terms of an infinite number of reciprocal space vectors within the first Brillouin zone, $\vec{k}$. Unfortunately, we can not manage an infinite number of $\vec{k}$. We can resolve this problem by sampling the Brillouin zone at special sets of k-points. The k-points sample can be calculated by various methods, the most popular being the Monkhorst-Pack method,[48] the Cunningham method,[49] and the Chadi-Cohenmethod.[50] The total wave function at each k-point can be expressed in terms of a discrete planewave basis set (3D-Fourrier series).

$$\psi_{n,\vec{k}}\left(\vec{R}\right) = \sum_{g} a_{n\,BAND,\overrightarrow{g},\overrightarrow{k}} \exp i\left(\vec{g}+\vec{k}\right)\vec{R} \tag{2.21}$$

In principle this set is infinite but we can consider it converged for large values of $\left|\vec{g}+\vec{k}\right|$. Introducing a plane-wave energy cut-off $\left|\vec{g}+\vec{k}\right| \leq G_{cut-off}$ reduces the basis set to a finite size. This energy cut-off value depends on every system. Therefore, it is necessary to test the convergence of the energy to take a correct value of the cut-off. Additionally, the use of plane-waves forces us to express the vacuum with the same accuracy as the regions of high electronic density. A large number of plane waves are habitually needed.

Using pseudopotentials reduces the $E_{cut-off}$ and, consequently, the size of the expansion.

2.6 Using pseudopotentials. The PAW method

Working with transition metals involves treatment with a large number of electrons, so the computational time increases exponentially as the system size increases. One way to tackle this problem is to consider that the chemical bond does not depend on the core electrons. Really, only the bonding energy is affected by the average electrostatic potential generated in the vicinity of the core. The plan is then to model the core electrons and their interaction with the other electrons. The concept of pseudopotential was introduced by Fermi and Hellmann who, in the 1930s, proposed solving the Schrödinger equation for the valence electrons in the subspace orthogonal to the core electrons. This concept was extended and led to the development of pseudopotential methods such as norm-conserving pseudopotentials,[51] ultra-soft pseudopotentials (US-PP),[52] and the Projector Augmented Wave (PAW) method.[53] The PAW method was introduced by Blöchl in 1994.[53] It is built on projector functions that allow the complicated wave functions to be mapped onto 'pseudo' wave functions, which are easier to be treatten computationally. With this method, we model the core electrons taking the difference between the exact wave function and a pseudo-wave function obtained and neglecting the core electrons. The Schrödinger equation is then expressed as

$$\tau * H\tau\tilde{\Psi} = E\tau * \tau\tilde{\Psi} \tag{2.22}$$

where $\tilde{\Psi}$ is pseudo wave function and τ is the operator of transformation that connects the exact wave function (Ψ) and the pseudo-wave function (Ψ). In DFT, we solve the Schrödinger equation to determine the pseudo-wave functions. Projectors then enable us to obtain the exact density, as long as the basis set expansion is complete. The PAW method has extensively proven its high performance for studying molecules, surfaces and solids. We used these pseudopotentials to perform the calculations in this work.

2.7 The VASP code

The VASP (Vienna Ab initio Simulation Package), a program developed by G. Kresse, J. Furthmüller and J. Hafner,[54–58] has been used for all calculations in this thesis. This code applies DFT to periodical systems, using plane waves and pseudopotentials. VASP includes an optimized set of US-PP and PAW pseudopotentials for all elements of the periodic system. In VASP, the Kohn-Sham equations are solved self-consistently with an iterative matrix diagonalization combined with the Broyden/Pulay mixing method[59, 60] for charge density. Combining these two techniques makes the code very efficient, especially for transition metal systems that present a complex band structure around the Fermi level. Algorithms implemented in VASP to optimize geometry are based on the conjugate gradient scheme, the block Davidson scheme or a residual minimization scheme (RMM). These algorithms work as follows: they calculate the electronic ground state for a given geometry, calculate forces, and then predict a new geometry based on the calculated forces. These steps are then repeated until an energy convergence criterion is reached. A special algorithm is the quasi-Newton, where the energy criterion is ignored and only the forces are minimized. The Hamiltonian is determined in pieces in direct and reciprocal space. Fast Fourier Transformations (FFT) are used to switch from direct to reciprocal space and vice versa. This allows for partial diagonalization. The number of k-points in the irreducible part of the Brillouin zone is crucial for accurately integrating the properties computed. The k-points sample is usually calculated by the program using the Monkhorst-Pack method.[48] To improve the convergence regarding the k-points sampling, several techniques can be used: the linear tetrahedron method, smearing methods such as finite temperature approaches or improved functional form (Methfessel and Paxton method,[61] and finite methods such as gaussian or Fermi smearing). Transition state structures and energies can also be found by various techniques (NEB, Dimer method, Lanczos) implemented in the VASP code. Frequencies and normal modes can also be computed with this code.

2.8 Vibrational frequencies

Molecules adsorbed on metal surfaces are highly complex, whose details cannot be predicted from the molecular structure and reactivity corresponding to the gas phase. Establishing the mechanisms of microscopic surface reactions requires determining precisely the structure of molecules adsorbed. Among the large number of analytical methods used in surface science, vibrational spectroscopy is commonly used to investigate heterogeneous catalysis.[62–64] The most common techniques are the RAIRS and HREELS. We can find detailed and accurate descriptions of these techniques in the references.[65–67]

Vibrational analysis provides useful information on adsorbate structure, and preferred ways to link the site adsorption.[68] It is also essential to find the zero-point energy correction and to calculate partition functions to obtain macroscopic properties such as enthalpy, entropy or kinetic coefficients, among others.

The calculation of the vibrational frequencies is usually done under the harmonic approximation, obtaining the matrix of force constants for later diagonalization. Vibrational frequencies and the corresponding normal modes (VNM) were computed within the harmonic approach using the VASP code. We greatly simplified the vibrational treatment by neglecting the coupling between surface phonons and adsorbate vibrations. This freezes the surface coordinates. In VASP, the Hessian dynamical matrix is built with the finite differences of the first derivatives from the total energy by geometrical perturbation of the optimized Cartesian coordinates.

2.9 Transition state search

To study the reactivity of a system it is necessary to determine its energetic pathway. Determining minima and transition states is necessary to build this reaction pathway. Consequently, it is required to identify the possible intermediates and transition states. At minima (reactants, products and intermediates) and transition states, the first derivatives of the energy (forces) must be zero. However, the transition states, i.e. the first order saddle points, must be a maximum in one direction, the one that connects the reactant and the product minima, and minimum in all the other directions, i.e. the second derivative of the energy respect to the reaction coordinate is negative but in all the other directions it is positive.[69] The localization of the transition state is essential to understand the energetics of a chemical reaction. Jónsson *et al.* developed the two transition state search algorithms implemented in VASP and used during this thesis the Nudged Elastic Band (NEB) method and the Dimer method.[70–72]

Nudged elastic band method

The Nudged Elastic Band (NEB) is a method to find saddle points and minimum energy paths between known reactants and products. With this method, several images or states of the system are connected to trace out a sort of path. Two points in the configuration space are needed (initial and final states). First, a set of images ({R0, R1, R2 ... RN}, N-1 replicas) between the initial and final states, typically in the order of 4–20, is obtained by linear interpolation (Figure 2.9). This is the most important step in the method: the initial

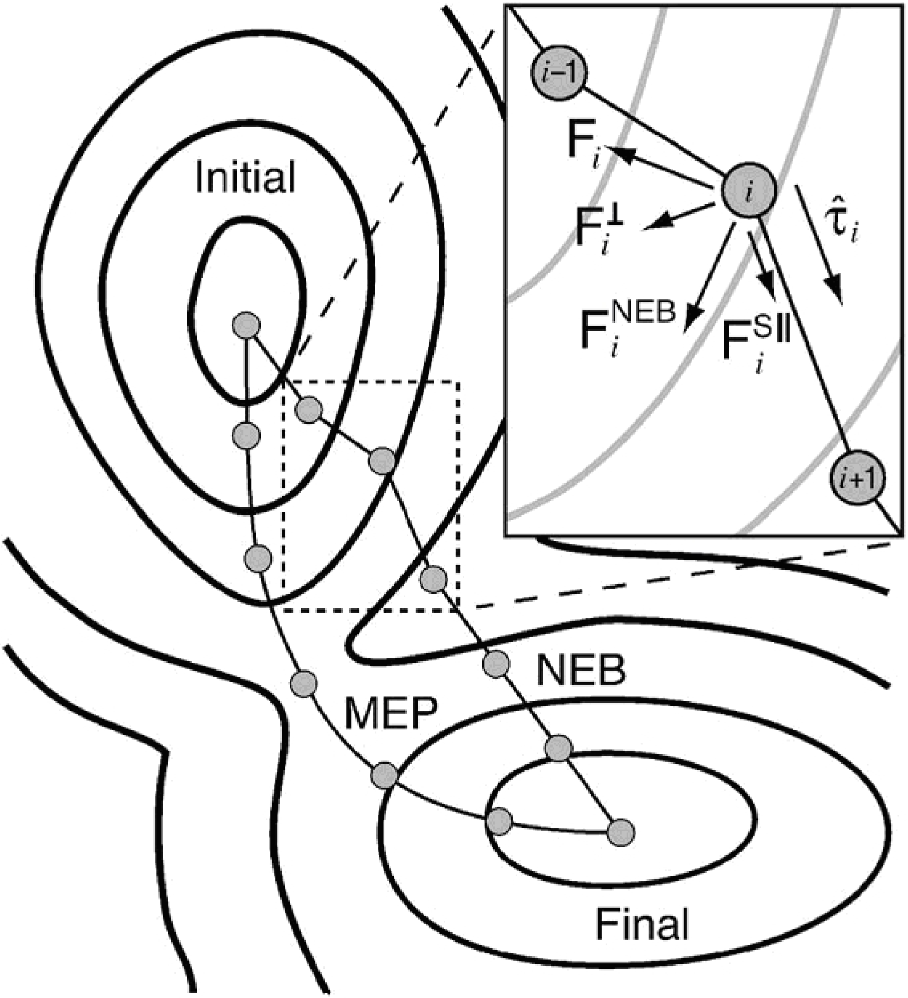

Figure 2.2: Two components make up the nudged elastic band force F^{NEB}: the spring force $F_i^{S\|}$, along the tangent $\hat{\tau}_i$, and the perpendicular force due to the potential $F_i^{\perp}$. The unprojected force do to the potential F_i is also shown for completeness.

guess has to be good enough to converge with a realistic Minimum Energy Path (MEP). With the NEB method, the N-1 images are optimized regarding all degrees of freedom except that of the reaction pathway. A spring constant is added to ensure the continuity of the path. The total force on an atom is the sum of the true force perpendicular to the local tangent and the spring force along the local tangent. The projection of the parallel component of the true force acting on the images and the perpendicular component of the spring force are cancelled.

$$F_i = F_i^S \big|_{\parallel} - \nabla E\left(R_i\right)\big|_{\perp} \tag{2.23}$$

The two projections are

$$\nabla E\left(R_i\right)|_{\perp} = \nabla E\left(R_i\right) - \nabla E\left(R_i\right)\hat{\tau}_i \big|_{\parallel} - \nabla E\left(R_i\right)\big|_{\perp} \tag{2.24}$$

and

$$F_i^S = k\left(\left|R_{i+1} - R_i\right| - \left|R_i - R_{i-1}\right|\right)\hat{\tau}_i \tag{2.25}$$

Here, E is the energy of the system, k is the spring constant and τ_i the normalized local tangent at the image i. The above definition of the spring force ensures the constant spacing of the images. The program will run each image simultaneously and communicate the forces at the end of each ionic cycle to compute the force acting on each replica. The minimization of the forces acting on the images would bring the NEB to MEP. Usually the number of images in NEB is too small for the length of the path and none of the images lies near the transition state at the end of the minimization process. The saddle point energy needs to be estimated by interpolation. The CI-NEB[71] was developed to cope with this problem. After several runs with the NEB, the highest energy image is identified ($imax$). This image is specifically treated and the force acting on it is now calculated as

$$F_{imax} = -\nabla E\left(R_{imax}\right)| + 2\nabla E\left(R_{imax}\right)|_{\parallel} \tag{2.26}$$

where $2\nabla E\left(R_{imax}\right)|_{\parallel}$ is twice the opposite of the true force parallel to the local tangent. The highest energy image is no longer affected by the spring forces. The minimization of this force leads to a rigorous convergence to the first order saddle point.

The Dimer method

Initially, the Dimer method[70] involves working with two images (replicas, R1 and R2) of the target system (n atoms); actually only an initial geometry

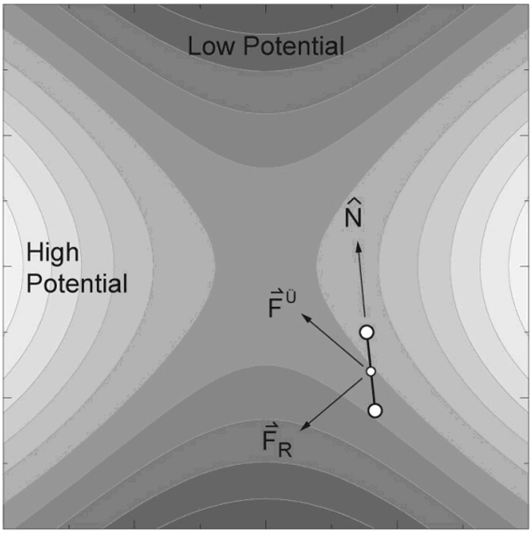

Figure 2.3: The effective force $F^{\dagger}$ acting on the center of the dimer is the true force F_R with the component along the lowest curvature mode $\hat{N}$ inverted. In the neighborhood of a saddle point, the effective force points towards the saddle point.

and an initial direction of the dimer are necessary. This pair of images is called dimer. These two replicas have almost the same 3n coordinates, but are displaced a small distance from a common midpoint, center of the dimer. The first order saddle point search algorithm involves moving the dimer uphill on the potential energy surface. There are two parts to each move: rotating and translating the dimer. Each time the dimer is translated, it has to be rotated in order to find the lowest curvature mode (lowest energy orientation). A rotational force $\vec{F}_R$ is defined which is the difference in the force on the two replicas. Minimizing the energy regarding this rotational force aligns the dimer with the lowest curvature mode (see Figure 2.9). The saddle point is at a maximum along the lowest curvature direction. As well as being rotated, the dimer has to be translated and moved up the potential energy surface. The net force acting on the center of the dimer tends to pull it towards a minimum. To avoid this, an effective force on the dimer is defined. In this modified force, the true force due to the potential acting in the midpoint of the dimer is defined as the opposite of the component along the dimer. Minimizing this force brings the dimer to the first order saddle point.

In this thesis the NEB method was used in combination with the Dimer method to determine the transition states. Normally, after a few iterations with the NEB, we obtained a rough estimate of the shape of the MEP. We then chose the two images with the highest energy to be the starting point for the Dimer method. Our results were refined until the value of the forces with the quasi-Newton algorithm implemented in VASP were negligible. Finally, we verified the transition states identified by vibrational frequency analysis, yielding a single imaginary frequency. This imaginary frequency has to be consistent with the reaction path under study.

2.10 Chemical kinetics

Chemical kinetics deals with the rate of chemical reactions and with how the rate depends on factors such as concentration and temperature. This study is important in proving the mechanisms of chemical processes. Kinetic studies cover a very wide range, from several points of view, such as the life time of the reactant, the time it takes to be consumed, the distribution of the products, and the determining of the rate.

A chemical reaction can be written in general as

$$aA + bB + \cdots \rightarrow \cdots + yY + zZ \tag{2.27}$$

where the lowercase (a,b. . . y,z) is the stoichiometric coefficient and the shift (A,B,. . .) are reactants and (Y,Z,...) products. The rate of reaction is defined as the disappearance rate of the reactants, or the formation rate of products:

$$r = \frac{1}{a}\frac{d\,[A]}{dt} = \cdots = \frac{1}{z}\frac{d\,[Z]}{dt} \tag{2.28}$$

where $[X]$ is the concentration of component X. For elemental bimolecular reactions the reaction rate can be expressed by an equation of the form

$$r = k\,[A]^a\,[B]^b \tag{2.29}$$

where k is the rate coefficient, and a, b are the independent of the concentration and the time. The rate coefficient can be correlated with the activation energy through the empirical equation of Arrhenius.

$$k = A\exp\left(\frac{-E_{act}}{k_bT}\right) \tag{2.30}$$

where A is the pre-exponential factor, E_{act} is the activation energy and k_B is the Boltzmann constant. The Reaction Rate theories are capable of predicting the reaction rate, in particularly the value of the pre-exponential factor. Collision theory, Transition State theory, and the RRKM theory are the most known rate theories.[73, 74] In this thesis we have used Transition State Theory to obtain these rate coefficients and simulate the concentrations in terms of time. This information is crucial for establishing the mechanism and the rate-determining step.

The theory of reaction rates, which was published almost simultaneously by H. Eyring[75] and by M. G. Evans and M. Polanyi[76] in 1935, is referred nowadays as conventional transition-state theory (CTST).[74] The treatment of the rates of surface reactions by CTST involves knowledge of the activation energies and of the partition functions for reacting species and activated complexes. The rate equation for a general reaction, derived by the methods of CTST is

$$k = \frac{k_B T}{h}\frac{q_{\#}}{q_R}\exp\left(\frac{-E_{act}}{k_B T}\right) \tag{2.31}$$

where $q_{\#}$ is the partition function of transition state and q_R is the partition function of reactive/s. Partition functions depend on temperature, hence the rate depends on time, temperature and concentration. In particular, the species on the surface only have vibrational partition functions, because of the lose of freedom grades. The partition functions is studied in statistical thermodynamics (for greater understanding of this functions we refer to P.W. Atkins' *Physical Chemistry*[77] and Levin's *Quantum Chemistry*[78]). In some cases, if we develop the general equation and apply some reaction conditions, the result can be expressed as a function of the adsorption equation.[74, 79] Thus:

$$r = \frac{p}{\left(2\pi m k_B T\right)^{1/2}} A_{cat}\theta_*^n \tag{2.32}$$

where A_{cat} is the Area of surface and θ_* is the coverage of free sites. Normally, the mechanism is enclosed by some simple reactions, describing a system of ordinary differential equations (ODE system). In this system it is necessary to insert an equation that denotes the free sites of surface. Thus:

$$\theta_* = 1 - \sum n\theta_{ads} \tag{2.33}$$

where 1 reveal the total free sites and θ_{ads} the coverage of adsorbed species. This equation converts the ODE system in a Differential-Algebraic equation system (DAE system). It is necessary use a mathematical package to numerically resolve the DAE system for any given initial conditions. The results led to the temporary evolution of each species as a function of a determinate temperature and initial conditions of the process. The microkinetic analysis of the reaction network reveals the mechanism of the process. If all possible reactions were included in the reaction network and then some of the reactions were eliminated, it would be possible to see the effect of the reactions in the network. By iterating the microkinetic analysis, we obtain the simple reaction network and reveal the mechanism of the process.[80]

Chapter 3

Characterization of NH_x Species on Pt(100) and Pt(111)

Periodic density functional theory (DFT) calculations using plane waves have been performed to systematically investigate the adsorption and relative stability of ammonia and its dehydrogenated species on Pt(100) and Pt(111). Different adsorption geometries and positions have been studied, and in each case, the equilibrium configuration has been determined by relaxation of the system. The vibrational spectra of the various ammonia fragments have been computed, and band assignments have been compared in detail with available experimental data. The adsorption of NH_3 (on top) and NH_2 (bridge) is more favorable on Pt(100) than on Pt(111), while similar adsorption energies were computed for NH (hollow) and N (hollow) on the three surfaces. The remarkably lower adsorption energy of NH_2 over Pt(111) as compared with Pt(100) (the difference being 0.7 eV) can be related to different geometric and electronic factors associated with this particular intermediate. Accordingly, the type of platinum surface determines the most stable NH_x fragment: Pt(100) has more affinity for NH_2 species, whereas NH species are preferred over Pt(111).

This chapter is based on the following publication:
G. Novell-Leruth, A. Valcárcel, A. Clotet, J. M. Ricart, J. Pérez-Ramírez; *J. Phys. Chem. B*, *2005*, 109, 18061.

3.1 Introduction

Ammonia is oxidized over platinum gauzes to form NO as the first step in the industrial production of nitric acid, a process that has been in industrial scale for over 80 years. This reaction is one of the highest temperature (1073-1173 K) and shortest contact time (10^{-3}-10^{-4} s) processes in the chemical industry and typically yields 95-97% of NO and only 3-5% of byproducts (N_2O and N_2).[3,15] Academic interest in the reaction lies in the challenge of elucidating details of the reaction mechanism and kinetics of product formation. Experimental assessment of the surface chemistry related to ammonia oxidation is intricate with currently available techniques due to the demanding experimental conditions of temperature and pressure and the very fast kinetics of the reaction, which make the identification of elementary steps and key reaction intermediates difficult. Hence, kinetic models have been typically derived by using a number of global steps whose rates were described by empirical rate models.[14]

Application of modern surface science techniques in UHV over platinum single crystals in a broad temperature range (300-1700 K),[81–88] and more recently, the Temporal Analysis of Products (TAP) reactor over commercial Pt and Pt-Rh gauzes at 973-1173 K[16–18] have provided insights into the mechanism of the high-temperature ammonia oxidation. These investigations demonstrated that the oxidation is initiated by the dehydrogenation of the ammonia molecule. This process is effectively catalyzed by adsorbed oxygen atoms and leads to reactive NH_x fragments (eq. 3.1). These fragments ultimately end in reaction products by further H stripping, O transfer into NH_x intermediates, and coupling of N species.

$$NH_3 + (3-x)\,O \rightarrow NH_x + (3-x)\,OH \tag{3.1}$$

Despite detailed studies, a generally accepted atomic-level description of the process of NH_3 adsorption as well as the systematic characterization of the key intermediate NH_x species has not been achieved as yet. This information would set the required basis for deriving solid microkinetic models able to predict the dynamic and steady-state performance of noble metal gauzes in industrial ammonia burners. As a matter of fact, the structure of the preferred NH_x intermediate(s) in ammonia oxidation has been the subject of animated discussions for a long time and still remains unsolved. Surface science studies using TPD (thermal programmed desorption), HREELS (high resolution electron energy loss spectroscopy), AES (Auger electron spectroscopy), and LEED (low energy electron diffraction) techniques in ultrahigh vacuum have shown that NH_2 and NH species are intermediates in ammonia oxidation on the Pt(100) and Pt(111) surfaces.[85,87] HREELS and TPR (temperature programmed reaction) studies also identified NH_2 species as the intermediate in the reaction of Hads and NO on the Pt(100)-1×1 and -hex surfaces.[6,89] Sun *et al.*[7] using HREELS and detected various NH_x species on Pt(111) upon electron bombardment of molecularly adsorbed ammonia. These authors reported that surface NH_2 species were dominant below room temperature. Dissociation of these species occurs in the temperature range of 300-400 K, and NH becomes the main surface species. On further heating, NH dissociates and gas-phase N_2 is formed.

Theoretical ab initio approaches based on quantum chemical principles can further contribute to a rational description of the complex ammonia oxidation process. Despite outstanding theoretical studies dealing with the synthesis of ammonia over a number of surfaces,[90,91] a systematic study of the adsorbed NH_x species on Pt(100) using state-of-the-art periodic models has not been reported. Fahmi and van Santen[92] studied the adsorption and activation of NH_3 on Pt(111) using small cluster models with 4 and 6 platinum atoms. Illas *et al.*[93] studied the adsorption of NH_3 on Pt(111) by also using cluster models and the hybrid B3LYP functional, not considering any dehydrogenated product. Jennison *et al.*[94] applied a periodic model and local density approximation (LDA). The properties of adsorbed NH_x species on Pt(111) and Pt(100)-(1×1) were also studied by the semiempirical method of interacting bonds.[95] Michaelides and Hu[96] and Baerns *et al.*[97] obtained the reaction barriers and enthalpy changes for the hydrogenation/dehydrogenation of NH_x species on Pt(111), but unfortunately, the adsorption geometries and energies of the starting and final adsorbates were not provided. Very recently, Ford *et al.*[98] studied a variety of atomic and molecular species, including NH_x, adsorbed on Pt(111).

This paper reports periodic density functional theory (DFT) calculations in order to systematically characterize the geometry, site preference, and relative stability of ammonia and its dehydrogenated species (NH_x, x=0-3) on two representative platinum surfaces, Pt(100) and Pt(111). A detailed analysis of the simulated vibrational spectra of the different adsorbed species is also provided, including relevant comparisons with existing experimental spectroscopic data.

3.2 Computational details

The calculations have been performed in the framework of DFT using the Vienna Ab Initio Simulation Program (VASP).[54–56] This program solves the Kohn-Sham equations of the density functional theory with the development of the one-electron wave function in a basis of plane waves. The electron-ion interactions are described by the projector augmented wave (PAW) method.[99] The tight convergence of the plane-wave expansion was obtained with a cut-off of 400 eV. The generalized gradient approximation (GGA) has been used with the functional of Perdew and Wang.[100] For the adsorbed open-shell NH_x species (x=0-2), a nonpolarized spin formalism was applied because spin polarization effects proved to be negligible ($<10^{-4}$ eV).

Different unit cells have been considered: 1×1, $\sqrt{2}\times\sqrt{2}$, $\sqrt{3}\times\sqrt{3}$, 2×2, and 3×3 associated with molecular coverages of 1, 1/2, 1/3, 1/4, and 1/9 ML, respectively. The twodimensional (2D) Brillouin integrations have been performed on a 5×5×1 grid for all the unit cells. The correct convergence of the adsorption energy by using this density of k-points was evaluated. The Pt(100) and the Pt(111) surfaces have been modeled by a 2D slab in a three-dimensional (3D) periodic cell generated by introducing a vacuum width in the direction perpendicular to the surface of ca. 12 Å. The slabs contain four atomic metal layers, with the target molecule and atomic species (NH_3, NH_2, NH, N, or H) adsorbed on one side of the slab. The Pt-Pt interatomic distances have been optimized for the bulk, and the resulting calculated value (2.82 Å) was very close to that determined experimentally (2.77 Å).

The geometry optimization included all degrees of freedom of the adsorbate and the two uppermost metal layers, while the two lowest metal planes were kept fixed at the optimized bulk geometry. The adsorption energy (E_{ads}) was computed as the difference between the energy of the adsorbed molecule ($E_{adsorbate-surface}$) and the sum of the free surface ($E_{surface}$) and the corresponding gas-phase species ($E_{gas-phase\,molecule}$) energies according to eq.3.2.

$$E_{ads} = E_{adsorbate-surface} - E_{surface} - E_{gas-phase\,molecule} \tag{3.2}$$

A negative value of E_{ads} indicates an exothermic chemisorption process. To compare the relative stabilities of the different studied species, the adsorption energies have been recalculated with respect to the NH_3 molecule in the gas phase. This has been done by considering the energy of adsorbed NH_x and (3-x) H atoms without any interaction between them.

The vibrational frequencies and the corresponding normal modes were calculated within the harmonic approach. The block of the Hessian matrix corresponding to adsorbate atomic displacements was obtained by numerical differences of the analytical gradients. Only second derivatives of the energy were considered. This approximation should be taken into account when a comparison with experimental spectra is established because anharmonic effects can be especially important in the region of NH stretching modes.[101] The coupling between molecular vibrations and surface phonons was also neglected in order to simplify the spectral treatment. The dynamic dipole moments of the vibrational modes were computed in order to estimate the intensities of the RAIRS and HREELS spectra. For both RAIRS and the specular mode of HREELS spectra, only those vibrational modes that give rise to an oscillating dipole perpendicular to the surface are active. The derivatives of the dipole moment were calculated by finite differences from the same structures used in the frequency calculations by means of an external code especially developed for this purpose.[102] The absolute intensities of the energy losses normalized to the elastic peak intensity were evaluated following the formula of ref. 103. Then, to compare both types of spectra, EELS intensities were normalized to the most intense RAIRS feature in each system. The Nudged Elastic Band (NEB)[72] method, in combination with the Dimer method,[70] were used to determine the transition states.

3.3 Results and discussion

Adsorption of NH_3 on Platinum

As shown in Figure 3.3, ammonia adsorbs on top sites of both Pt(100) and Pt(111) surfaces, in agreement with previous theoretical studies of NH_3 adsorption on transition metals.[92, 93, 98, 103–105] All attempts to find a minimum of energy in the other symmetric sites led to the top one after complete optimization. The analysis of the molecular electrostatic potential of the Pt(111) surface showed[106] that the points with largest electron density and, therefore, with the largest Pauli repulsion, are located at the hollow sites and the most stable interaction occurs on the top site. The calculated N-Pt distance is 2.13 and 2.15 Å on Pt(100) and Pt(111), respectively, and the obtained N-H distances in the adsorbed NH_3 molecule (1.020 Å) hardly change with respect to those in the gas phase (1.024 Å).

The pyramidalization angle defined by the C_3 axis and one of the N-H bonds increases from 106.5° (gas-phase NH_3) to 110° (adsorbed NH_3). Similarly, the H-N-H-H dihedral angle increases from 113.4 to 122.4° upon adsorption. On the basis of these data, it can be concluded that ammonia chemisorbs

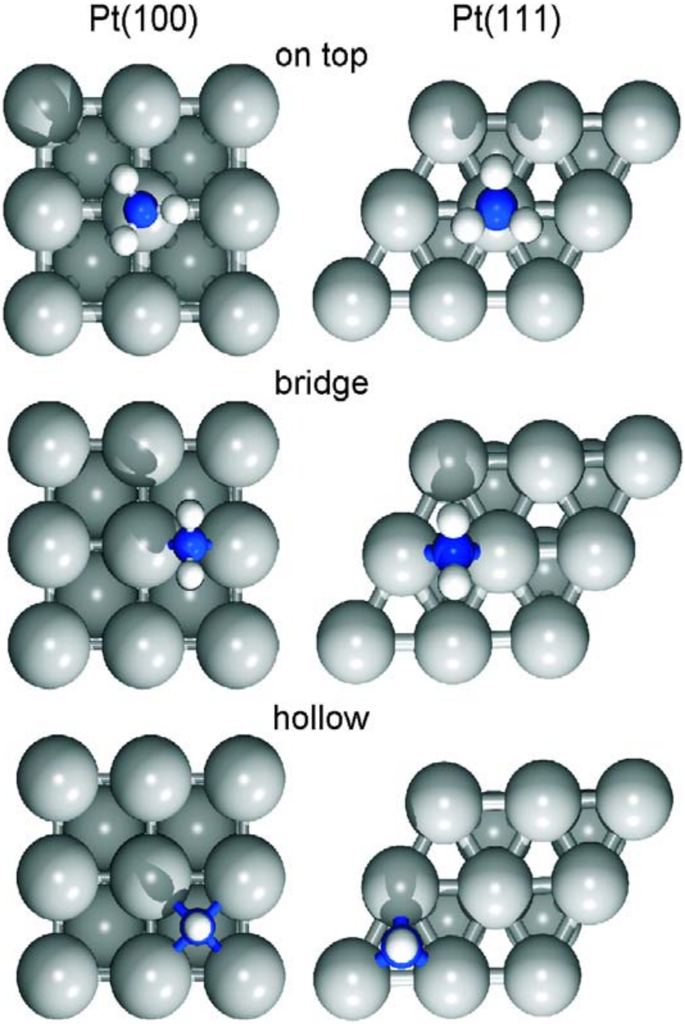

Figure 3.1: Adsorbed NH_x (x=3-1) on top, bridge, and hollow positions on Pt(100) and Pt(111) surfaces.

Table 3.1: Adsorption energies for NH_3 adsorbed on top of Pt(100) and Pt(111). The numbers in parentheses are adsorption energies expressed per surface metal atom.

		E_{ads} / eV	
unit cell	coverage	Pt(100)	Pt(111)
1×1	1 ML	physisorbed	physisorbed
$\sqrt{2}\times\sqrt{2}$	1/2 ML	-0.57 (-0.29)	
$\sqrt{3}\times\sqrt{3}$	1/3 ML		-0.66 (-0.22)
2×2	1/4 ML	-0.89 (-0.22)	-0.75 (-0.19)
3×3	1/9 ML	-1.10 (-0.12)	-0.97 (-0.11)

on Pt(100) or Pt(111) without significantly altering its structure with respect to the gas-phase molecule, i.e., the adsorption is a nonactivated process.

The effect of coverage on the adsorption energy for NH_3 on Pt(100) is presented in Table 3.1. Coverages of 1/9, 1/4, 1/2, and 1 ML were investigated using 3×3, 2×2, $\sqrt{2}\times\sqrt{2}$, and 1×1 unit cells, respectively. In general, the adsorption energy of NH_3 decreases when increasing the coverage. The repulsive interactions are small between 1/9 and 1/4 ML, attending to the small energy difference between these two coverages (0.21 eV). The energy difference between coverages of 1/4 and 1/2 ML increases 0.32 eV. From these data, the repulsive energy per NH_3 molecule can be determined as 0.05 eV at 1/4 ML and 0.13 eV at 1/2 ML. At 1 ML, the system is not stable. In fact, the NH_3 molecule is physisorbed in the 1×1 cell and interacts with the metal surface through one of its H atoms, the Pt-H distance being 2.92 Å. Any attempt to place the molecule closer to the Pt surface was proved unsuccessful.

To eliminate artificial effects arising from the model, the 1 ML coverage was also analyzed considering two NH_3 molecules in a $\sqrt{2}\times\sqrt{2}$ unit cell. As shown in Figure 3.3. Adsorption energy of the different species on Pt(100) and Pt(111). Energy computed with respect to $NH_3(g)$. for Pt(100), the optimized geometry leads to one NH_3 molecule adsorbed in its most stable adsorption mode (on top) but slightly tilted, and the other molecule interacts with the former via its nitrogen atom. The computed adsorption energy of the two NH_3 molecules is -0.87 eV. This represents a significant extra stabilization of 0.29 eV with respect one NH_3 molecule adsorbed in a $\sqrt{2}\times\sqrt{2}$ unit cell plus one NH_3 molecule in the gas phase. This is consistent with the existence of two forms of adsorbed ammonia above a certain coverage: α-NH_3, which saturates at 1/4 ML, and β-NH_3, which is weakly bonded to α-NH_3 layer via one of its hydrogen atoms.[87, 94, 107] The calculation of adsorption energies per surface

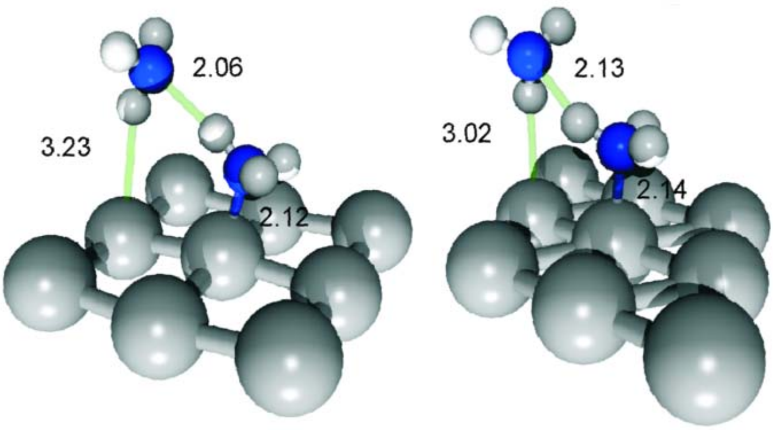

Figure 3.2: NH_3 adsorbed at 1 ML (one ammonia molecule per 1×1 unit cell) on Pt(100) (right) and Pt(111) (left). Two ammonia molecules are shown, one is adsorbed on top (α-NH3), and the other is physisorbed (β-NH3). Only a fragment of the first layer of the surface is displayed. Relevant distances (in Å) are given.

metal atom, given by the numbers in parentheses in Table 3.1, leads to the conclusion that the most stable adsorbed phase for ammonia at 0 K occurs around 1/2 ML on Pt(100).

The adsorption of NH_3 on Pt(111) presents clear similarities with that of Pt(100). In this case, the 3×3, 2×2, $\sqrt{3}\times\sqrt{3}$, and 1×1 unit cells were computed to consider coverage effects. The adsorption energy decreases from -0.97 to -0.66 eV upon increasing the coverage from 1/9 ML (3×3) to 1/3 ML ($\sqrt{3}\times\sqrt{3}$). The 1 ML coverage (one NH_3 per 1×1 unit cell) led to physisorbed ammonia as for Pt(100). Attending to the adsorption energy per surface metal atom, the most favored coverage on Pt(111) is 1/3 ML, albeit the energy differences are smaller than those on Pt(100). In fact, the 1/3 ML and 1/4 ML coverages are quasi-equivalent because the obtained energy difference is within the accuracy of the computational method. Our calculations also corroborate the existence of a weakly adsorbed NH_3 species on Pt(111). The optimization of two NH_3 molecules in a $\sqrt{3}\times\sqrt{3}$ unit cell originated an adsorption structure similar to the one obtained on Pt(100) (see Figure 3.3). The adsorption energy of this system is -0.85 eV. This adsorption structure is then 0.20 eV more stable than one adsorbed NH_3 in a $\sqrt{3}\times\sqrt{3}$ cell plus one ammonia molecule in the gas phase.

The computed adsorption energies (E_{ads}) of NH_3 are comparable with values in the literature, -1.15 eV (Pt_{10} cluster model, B3LYP functional[93]), -1.21 and -1.13 eV (Pt_4 and Pt_6 cluster models, respectively, BP functional[92]), and -0.9643 and -0.78 eV[98] on Pt(111) (slab model, 0.5 ML, PBE and PW91 functionals, respectively). Notice that cluster models represent a zero coverage situation and usually lead to an overestimated adsorption energy with respect to the ideal surface. The correspondence with those obtained experimentally is also reasonable: -1.1 eV from collision-induced desorption[108] for Pt(111), and the same value was estimated for Pt(100) from TPD at 0.3 ML.[87]

The effect of pressure and temperature on the NH_3 surface coverage was also analyzed using an approximate method,[109–113] where the gas phase plays the role of a reservoir in equilibrium with the substrate and the adsorbed phase. The adsorption Gibbs free energy per surface metal atom for the reaction

$$Pt\,(S_0) + n\,NH_3\,(gas) = adsorbed\,NH_3\,(S_n) \tag{3.3}$$

was computed using

$$\begin{aligned}\Delta G^0 = \mu^0\,(S_n) - \mu^0\,(S_0) - \mu^0\,(NH_3) = E\,(0\,K)\\ - RT\ln\left[{}^{q(S_n)}\!/_{q(S_0)q(NH_3)^n}\right]\end{aligned} \tag{3.4}$$

In this expression, $\mu^0\,(S_n)$ and $\mu^0\,(S_0)$ are the chemical potentials of the covered surface and the clean surface, respectively, $E\,(0\,K)$ is the electronic energy variation for the adsorption process (E_{ads}) per surface metal atom, including the zero point energy (ZPE), and q are the corresponding partition functions. Assuming that the changes in the vibrational density of states for the surface are negligible (i.e., $q\,(S_n) \approx q\,(S_0)$),[110] the former expression can be simplified by:

$$\Delta G = E_{ads} + \Delta ZPE + RT\ln\left(q\,(NH_3)\right) - RT\ln\left({}^{P(NH_3)}\!/_{P^0}\right) \tag{3.5}$$

Figure 3.3 shows the free Gibbs energy for the adsorption of ammonia on Pt(100) as a function of the temperature for different coverages (0.11, 0.25, and 0.5 ML) and pressures. The two selected pressures are representative of UHV conditions (10-12 atm) and industrially relevant flow conditions (1 atm). From this diagram, the desorption temperature of adsorbed ammonia can be estimated, assuming that decomposition into N_2 and H_2 does not occur.

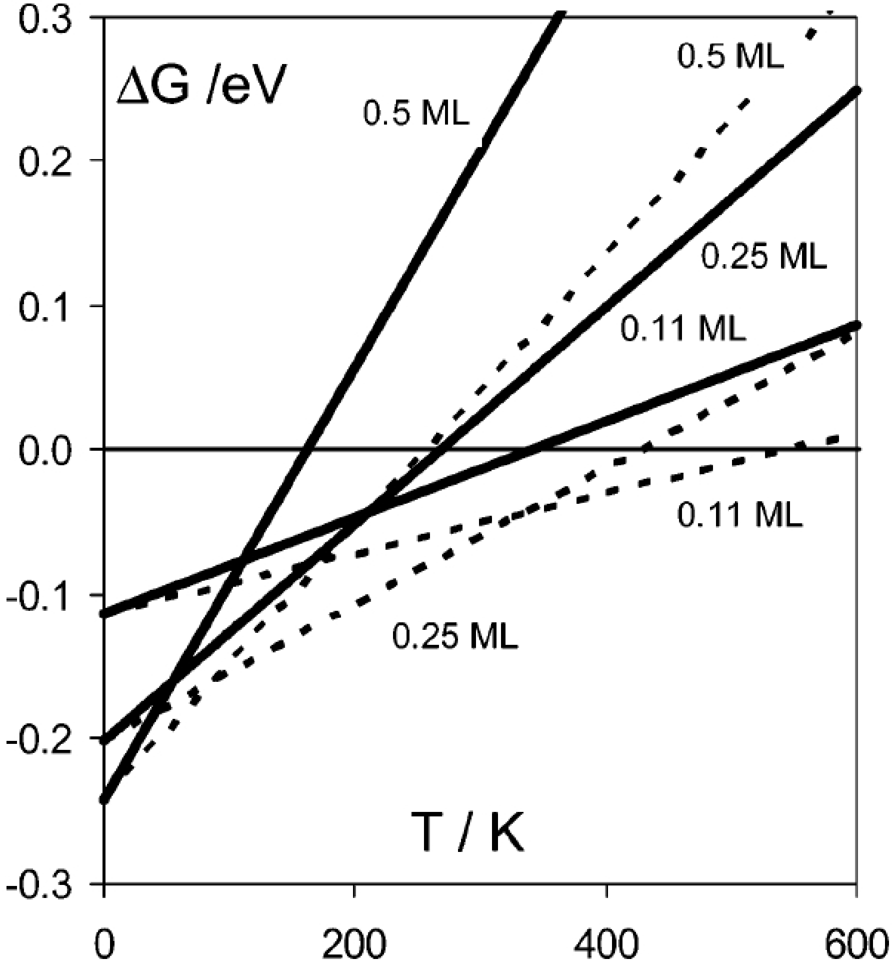

Figure 3.3: Variation of the Gibbs free energy for the adsorption of NH_3 as a function of the temperature for different coverage (0.5, 0.25, and 0.11 ML) of NH_3 adsorbed on Pt(100). Two pressures have been selected: typical pressure in UHV studies (10^{-12} atm, solid line) and flow conditions (1 atm, dashed line).

The maximum desorption temperature at UHV conditions is ca. 350 K for a low ammonia coverage (0.11 ML). This calculation agrees well with the thermal desorption spectra of 0.1 ML of ammonia over Pt(100), showing a peak centered at 350-370 K10 that shifts to lower temperature when increasing the coverage. At 1 atm, the desorption temperature increases to about 550 K. The same trends are found for Pt(111), which are not shown for the sake of conciseness.

Adsorption of NH_x fragments

Table 3.2 shows the adsorption energy of the NH_3 molecule and the various ammonia fragments (NH_x, x=0-2) on Pt(100) and Pt(111) at 0.25 ML. For the sake of comparison, we also included the adsorption energy of the H atom.

For NH_2, two stable adsorption sites were found: top and bridge. Zemlyanov at al.[6] suggested that the bridge adsorption site is the preferred position on Pt(100). Our calculations clearly support the experimental findings. In fact, the top site is less stable by 0.99 eV on Pt(100) and 0.47 eV on Pt(111). NH and N fragments adsorb preferentially on hollow sites (Figure 3.3). This adsorption site is the only stable position for NH and N on Pt(111) and N on Pt(100) at 0.25 ML. On the other hand, for NH adsorbed on the 100 surface, we also found a minimum on the bridge site.

NH_3 and NH_2 re more strongly adsorbed on Pt(100) than on Pt(111), whereas NH and N are slightly more stable on Pt(111). These differences are quite significant (see Table 3.2). However, for a proper comparison, we have to take into account the effect of the second metal layer, which may be important especially for species adsorbed on hollow sites. In fact, the adsorption energy of NH adsorbed on Pt(111) is 0.40 eV larger on fcc than on hcp positions. As the 4-fold hollow site of the Pt(100) surface has one Pt atom directly below (second metal layer), this position is similar to the hcp one for the 111 surface. Thus, if the adsorption energy of NH on Pt(100) is compared to the one on the hcp site of Pt(111), the former is more stable. The picture for N is rather similar. The difference in adsorption energy is drastically reduced if one compares the hollow site of the Pt(100) surface with the hcp site of Pt(111) (the difference is only 0.11 eV).

The different stability of NH_2 on Pt(100) and Pt(111) deserves particular attention. The difference in the adsorption energy between both surfaces is of 0.67 eV, i.e., 0.4 eV larger than the differences for NH_3 or NH (see Table 3.2). The adsorption energy is the sum of three contributions: distortion energy of the adsorbed molecule, distortion energy of the surface, and interaction energy of adsorbate-surface. In general, the metal atoms on the adsorption

Table 3.2: Adsoprtion energies (eV) of the different species at 0.25 M. Only true minima are shown. The energy was computed with respect to the corresponding species in the gas phase and with respect to NH_3 in gas phase, considering the NH_x species and (3-x)H atoms adsorbed without interaction between them (in parentheses). The first column is the energy diference between NH_x +(3-x)H nd NH_3 in gas phase.

	gas phase				
	NH_3	NH_2	NH	N	H
	0.00	4.98	9.40	13.10	
			Pt(100)		
ontop	-0.89	-2.15 (-0.06)			-2.68
bridge		-3.14 (-1.05)	-3.81 (-0.16)		-2.88
hollow			-4.01 (-0.37)	-4.40 (0.06)	-2.52
			Pt(111)		
ontop	-0.75	-2.00 (0.22)			-2.72
bridge		-2.47 (-0.24)			-2.71
fcc			-4.24 (-0.34)	-4.80 (0.04)	-2.75
hcp			-3.84 (0.05)	-4.51 (0.33)	-2.70

site move upward with a concomitant increase of the Pt-Pt bond distances. For Pt(100), the Pt-Pt distance increases from 2.82 to 2.98 Å, whereas for the Pt(111) surface, it increases by only 0.02 Å. Thus, the 100 surface strongly adapts the Pt-Pt bridge in order to better accommodate the NH_2 species. This distortion is associated with the energy cost required to reach a certain adsorption geometry. However, the stronger distortion of the Pt-Pt bond in the adsorption on Pt(100) is not linked to a higher energy requirement. In fact,the energy distortion of the surface is 0.1 eV higher for Pt(111) (0.25 eV) than for Pt(100) (0.15 eV). The energy required to distort the NH_2 fragment from its gas-phase geometry to the adsorption one is equal for both Pt(100) and Pt(111) and very small (only 0.08 eV). Thus, the higher energy distortion of the surface results in a higher energy interaction on Pt(111), but this only accounts for 0.1 eV. Obviously, when the molecule absorbs on the metal surface, new bonds are created. To take into account the new bonds formed, we considered a NH_4^+ molecule with two hydrogen atoms at the same position as those of the adsorbed NH_2 fragment and the other two at the same site as the Pt atoms. We obtained an energy difference of 0.21 eV between the structure mimicking the minimum on Pt(100) and the one on Pt(111), being more stable the “Pt(100)-

minimum". The higher stability of the structure on Pt(100) can be ascribed to the fact that the angle Pt-N-Pt is closer to the tetrahedral angle on Pt(100) than that on Pt(111). Thus, we can consider this energy as an estimate of the distortion of the molecule. This contribution reduces the difference in interaction energy to only 0.36 eV.

In addition, the analysis of the projected density of states (PDOS) can provide insights into the different adsorption energies from an electronic viewpoint. Figure 3.3 shows the PDOS on the atomic orbitals of the N atom and the surface metal atoms. For NH_2 on Pt(100), the relevant orbitals are the p_y and p_z of N and the d_{yz} of Pt. On Pt(111), the orbitals involved in the adsorption are the p_x and p_z of N and d_{xz} of Pt. This difference is merely associated with the different construction of the supercell model. On both metal surfaces, the p_z orbital of N evidences a intense peak around 7.5 eV below the Fermi level and very small contributions at other energies within the band. Actually, the bonding states are just pushed to the bottom of d-band, which indicates that the interaction between the p_z orbital and the d-band is relatively weak. The situation with the p_y (p_x) orbital is rather different. The interaction with the d-band splits the p_y (p_x) orbital into two broadened levels: a bonding (below the Fermi level) and an antibonding one (above the Fermi level), with a gap in between. The position of the bonding and antibonding contributions as well as the separation from each other is a measure of the strength of the adsorbate-surface interaction. The gap is slightly larger on the Pt(100) surface (5.83 eV) than on Pt(111) (5.70 eV), as expected from the calculated adsorption energies. Moreover, the contributions of the d_{yz}(d_{xz}) states above the Fermi level decrease in the order Pt(100) $>$ Pt(111), in agreement with the reduced adsorbatesurface interaction on Pt(111).

The adsorption energy of the NH_x species with respect the same species in the gas phase increases in the order $NH_3 < NH_2 < NH < N$ for both metal surfaces (Table 3.2). Obviously, this reference reflects the increasing instability of each one of these species in the gas phase. A more appropriate reference is NH_3 in the gas phase for all the fragments, considering the adsorbed NH_x species and (3 - x)H atoms without interaction between them (Table 3.2 and Figure 3.3). These results clearly evidence that adsorbed $NH_2 + H$ is considerably more stable than adsorbed NH_3 on Pt(100), while the contrary occurs on Pt(111). This finding strongly suggests that the dehydrogenation of ammonia on platinum is surface sensitive. Differently, the adsorption energy of the NH and N fragments is remarkably similar over both platinum surfaces. In view of the relative stability of the different ammonia fragments, it can be tentatively suggested that NH_2 is the predominant species during ammonia dehydrogenation on Pt(100). On Pt(111), NH is only slightly more stable than NH_2, and

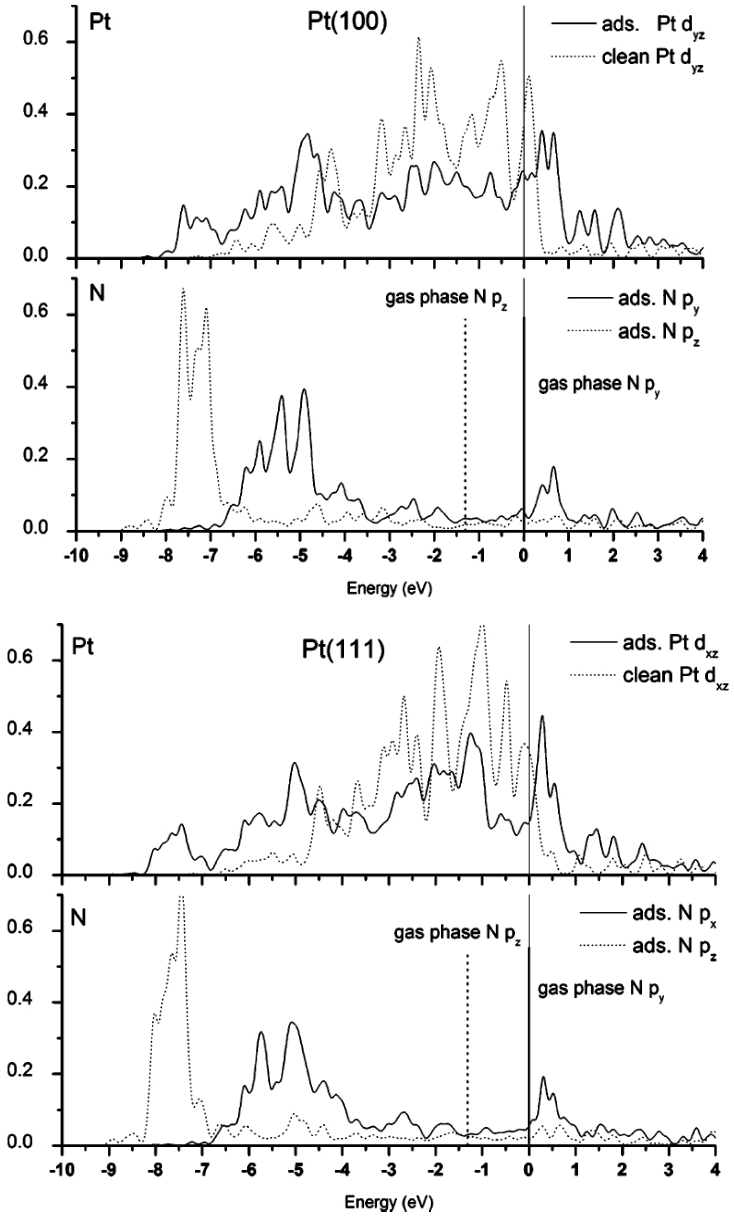

Figure 3.4: PDOS for selected orbitals of N and Pt corresponding to the adsorption of NH_2 on Pt(100) and Pt(111) surfaces.

UNIVERSITAT ROVIRA I VIRGILI
CATALYTIC AMMONIA OXIDATION ON NOBLE METAL SURFACES: A THEORETICAL STUDY
Gerard Novell Leruth
ISBN:978-84-692-1534-0/ DL:T-377-2009

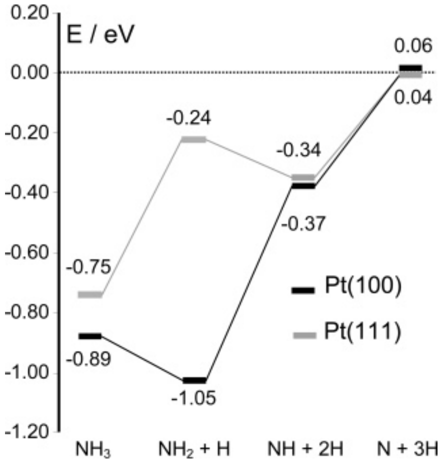

Figure 3.5: Adsorption energy of the different species on Pt(100) and Pt(111). Energy computed with respect to NH_3(g).

both NH and NH_2 species are expected to populate the catalyst surface in an equivalent manner.

Geometrical parameters of the different adsorbates are displayed in Table 3.3. The perpendicular distance from the N atom to the platinum surface decreases in the order $NH_3 > NH_2 > NH > N$ for both planes, which reflects the increasing interaction between the nitrogen fragments and the surface. In the case of NH and N, adsorbed on hollow position, this distance is larger on Pt(111) due to the more closed character this surface. With respect the N-Pt distances, they are similar in all the cases, although they are slightly larger on Pt(100) than on Pt(111) for NH and N. The N-H distance and the HNH angle (for NH_3 and NH_2) are also very similar in all cases (1.02 Å and 111°, respectively).

Although the aim of the present paper concerns only the structure and relative stability of the NH_x fragments, we have computed also the energy barriers for the different dehydrogenation processes. The present results are in a reasonable agreement with the theoretical data provided by Michaelides and Hu[96] and Baerns *et al.*[97] for the NH_x hydrogenation/ dehydrogenation reactions on Pt(111). As shown in Table 3.4 these barriers are rather high, in agreement with the experimental observation that NH_3 hardly dissociates on Pt below 400 K.[7,87,114]

Table 3.3: Geometrical parameters for adsorbed NH_x species on Pt(100) and Pt(111) at 0.25 ML. Z_N (Å) is the perpendicular distance of N to the metal surface. D_{M-Pt} (Å) is the distance to the first Pt neighbor. The N-H distances are 1.02 Å in all cases and the HNH angles are 111º for both NH_3 and NH_2.

	Pt(100)		Pt(111)	
species (site)	Z_N	D_{N-Pt}	Z_N	D_{N-Pt}
NH_3 (on top)	2.127	2.127	2.148	2.148
NH_2 (bridge)	1.426	2.062	1.521	2.088
NH (hollow / fcc)	0.913	2.179	1.071	2.009
N	0.758	2.108	1.005	1.957

Table 3.4: Energy barriers (in eV) for the process $NH_x(ads) \rightarrow NH_{x-1}(ads) + H(ads)$, (x=3-1). Values include the ZPE correction.

	surface	
elemantary step	Pt(100)	Pt(111)
$NH_3 \rightarrow NH_2 + H$	1.05	1.02
$NH_2 \rightarrow NH + H$	1.63	1.10
$NH \rightarrow N + H$	0.88	0.97

Analysis of the infrared spectra

In this section, we have analyzed the simulated infrared spectra of NH_x species on Pt(100) and Pt(111). Unfortunately, no infrared data of adsorbed NH_3 on Pt(100) is available in the literature. In fact, the only existing vibrational data were collected by Zemlyanov *et al.*,[6,89] who aimed at the identification of reaction intermediates formed in the reaction of NO with H_2 on Pt(100). For Pt(111), EELS and RAIRS (reflection absorption infrared spectroscopy) spectra were obtained by Mieher and Ho.[85] These authors assigned several features to NH_3, NH_2 , NH, and N following previous works of Sexton and Mitchell,[83] Gohndrone *et al.*,[114] and Bassignana *et al.*[115] Sun *et al.*[7] obtained a collection of HREELS spectra of NH_x fragments on Pt(111) by means of electron irradiation and heating. They suggested NH_2 and H are the dominant species after electron irradiation at low temperature, and NH after heating to room temperature. At 500 K, only atomic N was present on the surface.

Calculated harmonic frequencies and RAIRS and EELS intensities of the corresponding fundamental bands of NH_3, NH_2, and NH on Pt(100) and Pt(111) using a (2×2) unit cell are presented in Tables 3.5 and 3.6, respectively. Only frequencies above the Pt-NH_x-frustrated translation are reported because coupling effects between molecular vibrations and surface phonons were neglected and low-frequency vibrations are more importantly influenced by this assumption.

NH_3. In the N-H stretching region, and because of the adsorption mode of NH_3 on the Pt(100) surface, only the NH_3 symmetric stretching (3348 cm^{-1}, see Table 3.5) has an appreciable intensity on the RAIRS spectrum, but this band almost vanishes on the EELS spectrum. The frequencies associated with the degenerated stretching frequencies of free NH_3, not degenerated when adsorbed on the Pt(100) surface, present an intensity close to zero. This fact is related to the maintenance of an almost C_{3V} molecular symmetry of the adsorbate as the gas-phase molecule. In the N-H deformation region, the same effect is observed. Only the symmetric NH_3 deformation mode (umbrella) is observed. This band, at 1086 cm^{-1}, appears as the most intense band of the spectrum (10 times more intense than the NH_3 symmetric stretching mode in the RAIRS spectrum), and this difference is even enhanced in the EELS spectrum. Other nonforbidden modes could be observd: the NH_3 symmetric rocking at around 620 cm^{-1} and the Pt-NH_3 stretching at 348 cm^{-1}. However, these bands present a very low intensity. The computed spectrum for NH_3 on Pt(111), presented in Table 3.6, is very similar to that on Pt(100), suggesting that adsorption of ammonia is not structure sensitive. This is in line with previous results over a variety of platinum surfaces[114] and with the

Table 3.5: Computed frequencies (ω_e in cm^{-1}) for NH_x species on Pt(100) at 0.25 ML. RAIRS intensities in km·mol^{-1}. EELS intensities in arbitrary units (see text). Relevant experimental values are also show. Asymetric: as; symetric: s.

	vibrational mode	ω_e	I_{RAIRS}	I_{EELS}	exp.
NH_3	as stretching	3477	0.00	0.00	
	as stretching	3472	0.01	0.00	
	s stretching	3348	5.55	0.25	
	as deformation	1572	0.03	0.01	
	as deformation	1566	0.04	0.01	
	s deformation	1086	55.90	55.90	
	rocking	619	0.02	0.06	
	rocking	618	0.00	0.01	
	Pt-NH_3 stretching	348	0.04	0.36	
NH_2	as stretching	3479	0.00	0.00	3388
	s stretching	3379	1.05	0.05	3298
	scissoring	1467	24.60	11.85	1450
	wagging	838	0.00	0.00	825
	twisting	834	0.00	0.00	
	rocking	664	0.00	0.00	
	Pt-NH_2 stretching	491	0.00	0.00	480
NH_3	stretching	3363	13.64	0.61	3150
	deformation	895	0.00	0.00	910
	deformation	858	0.01	0.01	
	Pt-NH stretching	430	0.06	0.36	460

present results. The NH_3 symmetric stretch appears at 3331 cm^{-1}. This value is higher than those obtained experimentally. The difference can be attributed to anharmonicity, coverage, and coadsorbate-induced effects. In fact, Mieher and Ho[85] reported a value of 3146 cm^{-1}, whereas Sexton and Mitchell[83] assigned the band at 3240 cm^{-1} to the same mode. NH_3 adsorbs on a top site with C_{3v} symmetry, and accordingly, the asymmetric stretching modes, computed at 3470 cm^{-1}, are forbidden. However, Mieher and Ho[85] assigned a band at 3363 cm^{-1} to the degenerated asymmetric stretching modes. Sun *et al.*[7] obtained bands at 3214 and 3332 cm^{-1} with very low intensity, as our calculations predict. Only a very weak band at 3281 cm^{-1} appeared when temperature increased from 160 to 200 K, and almost disappeared at 300 K. This is an effect of surface coverage (vide infra). The NH_3 symmetric deformation was computed at 1063 cm^{-1}, with lower intensity than that of the corresponding band appearing on Pt(100). Experimental frequencies are located at 1170 cm^{-1},[85] and 1137 cm^{-1}.[83] Actually, after annealing the adsorbed system,[85] i.e., when some NH_3 decomposition occurs, this band appears in the interval of 1129-1194 cm^{-1}, so the observed frequencies vary due to coverage and coadsorption effects. The difference between experiment and the present results can be attributed to computational precision and/or coverage effects. In fact, a small imaginary frequency below 100 cm^{-1} was observed, which is related to the NH_3 torsion mode. As this mode is almost free, we have associated this imaginary frequency to the accuracy limit to describe the potential energy surface for ammonia rotation. This could be an artifact due to the proximity of neighboring molecules on a 2×2 unit cell. Therefore, we have computed ammonia frequencies for both platinum surfaces using a larger 3×3 unit cell. On Pt(111), the imaginary frequency disappears, whereas that on Pt(100) still remains, but with a lower frequency. The other frequencies do not change appreciably when a lower coverage is considered, except for the NH_3 deformation mode, which shifts up to a value close to that obtained experimentally (1134 and 1144 cm^{-1} for Pt(111) and Pt(100), respectively). The RAIRS intensity of this band is higher for the 3×3 unit cell than for the 2×2 cell, whereas EELS intensity is lower because coverage is explicitly included on the computed intensity. The evolution of the spectra of adsorbed NH_3 with temperature of Sun *et al.*[7] supports these effects, because some NH_3 desorbs above 140 K, as XPS results show. At 160-200 K, the NH_3 deformation band appears at 1088 cm^{-1}. This value compares well with the present computed band at 1063 cm^{-1}. Above 200 K, this band shifts to 1125 cm^{-1} and loses intensity (the computed band for the 3×3 unit cell is 1134 cm^{-1}). The other NH_3 peaks also attenuate. Finally, the calculated Pt-NH_3 stretching at 348 cm^{-1} matches well with the available values (355 cm^{-1},[85] 347 cm^{-1},[83] and

340 cm^{-1}.[7]

NH_2. For the Pt(100) surface, in the N-H stretching region, only the NH_2 symmetric stretching (3379 cm^{-1}) is visible in the RAIRS spectrum, having a moderate intensity. As for NH_3, this stretching band tends to vanish on the EELS spectrum. The forbidden NH_2 asymmetric stretching appears at a higher frequency and close to the NH_3 vibrations. The spectrum of adsorbed NH_2 is dominated by the scissoring band at 1467 cm^{-1}. NH_2 wagging, twisting, and rocking vibrations appear at 838, 834, and 664 cm^{-1}, respectively, with almost zero intensity. Finally, the band at 491 cm^{-1} is associated with the frustrated translation of the molecule, but it also has a very low intensity. So, from present calculations, the fingerprint of this species adsorbed on the Pt(100) surface is the scissoring mode in the mid-IR region, around 1470 cm^{-1}, this band being much more intense than the band appearing on the N-H stretching region.

The present values agree well with the HREELS investigations by Zemlyanov *et al.*[6] They found bands at 480 (broad), 825 (weak), 1450 (strong), 3298 cm^{-1} (medium), and 3388 cm^{-1} (medium) that were assigned to Pt-NH_2 stretching, NH_2 wagging, scissoring, symmetric stretching, and asymmetric stretching, respectively.

On Pt(111), the NH_2 asymmetric and symmetric stretching modes appear at 3470 and 3360 cm^{-1}, respectively, with very low intensity. The most intense peak corresponds to the NH_2 scissoring mode at 1454 cm^{-1} (only 13 cm^{-1} lower than the value obtained for Pt(100)). Mieher and Ho[85] assigned values of 1613 or 1774 cm^{-1} to the scissoring modes following studies on Ni(110).[115] Sun *et al.*[7] attributed the new features appearing, after electron irradiation, at 830, 1392, and 1555 cm^{-1} to the NH_2 rocking, wagging, and scissoring modes, respectively. According to the well-reproduced value on Pt(100) and assuming that coverage effects cannot change the frequency by 200 cm^{-1}, it can be concluded that the assignment of Mieher and Ho of the NH_2 scissoring mode is not correct. On the other hand, the band[7] at 1392 cm^{-1}, should be reassigned to the scissoring mode. Moreover, when Sun *et al.*[7] repeated the experiments using deuterated ammonia, the band at 1392 cm^{-1} shifted to 1051 cm^{-1}. This value matches the calculated scissoring mode for adsorbed ND_2 of 1076 cm^{-1}. NH_2 wagging, twisting, and rocking frequencies (780, 771, and 665 cm^{-1}, respectively) have low intensity, but they are slightly higher than those obtained for Pt(100), particularly for the rocking mode. It is not easy to assign the experimental band at 830 cm^{-1}.[7] Although the calculated value is slightly lower, it can be ascribed to the NH_2 wagging and not to the rocking mode. Note that the intensity is nearly zero, corresponding to the geometry of adsorbed NH_2 (C_2 axis normal to the surface). However, if the NH_2 species

Table 3.6: Computed frequencies (ω_e in cm^{-1}) for NH$_x$ Species on Pt(111) at 0.25 ML. RAIRS intensities in km·mol^{-1}. EELS intensities in arbitrary units (see text). Relevant experimental values are also show. Asymetric: as; symetric: s.

					experimental		
	vibrational mode	ω_e	I_{RAIRS}	I_{EELS}	ref. 83	ref. 85	ref. 7
NH_3	as stretching	3470	0.00	0.00	3299	3363	3332
	as stretching	3470	0.00	0.00			
	s stretching	3331	9.11	0.40	3242	3146	3214
	as deformation	1556	0.00	0.00	1597	1613	1533
	as deformation	1553	0.00	0.00			
	s deformation	1063	47.90	47.90	1137	1170	1088
	rocking	630	0.00	0.00			
	rocking	622	0.05	0.14	718	694	718
	Pt-NH_3 stretching	348	0.17	1.42	347	355	370
NH_2	as stretching	3470	0.02	0.00			
	s stretching	3360	0.04	0.00		3307	3250
	scissoring	1454	18.08	8.48		1613-1774	1555
	wagging	780	0.01	0.01			1392
	twisting	771	0.08	0.16			
	rocking	665	0.25	0.68			830
	Pt-NH_2 stretching	468	0.47	2.40			488
NH_3	stretching	3396	15.78	0.66		3307	3280
	deformation	819	0.01	0.01		1428	
	deformation	819	0.00	0.00			
	Pt-NH stretching	536	0.00	0.01			

were tilted on the surface, as proposed by Sun *et al.*, the intensity would be larger. In fact, interadsorbate interactions may lead to tilting, but they are not explicitly included in our calculations. Finally, the frustrated translation appears at 468 cm^{-1} (488 cm^{-1}),[7] which is lower than the value on Pt(100), corresponding to a lower interaction energy on this face.

NH. Among the possible fundamental bands, only the NH stretching mode, appearing at 3363 and 3396 cm^{-1} for Pt(100) and Pt(111), respectively, has a significant intensity. The expected active NH deformation modes, at 858-895 cm^{-1} for Pt(100) and 819 cm^{-1} for Pt(111), have very low intensity because the H atom moves almost parallel to the surface in the corresponding normal modes. The Pt-NH frustrated translation appears at 430 and 536 cm^{-1} for the 100 and 111 faces, respectively, with an increasing intensity from RAIRS to EELS spectrum. Frequencies are in agreement with available experimental data for Pt(100).[89] For Pt(111), Sun *et al.*,[7] annealing to a temperature above 200 K after electron irradiation, observed only a band at 3280 cm^{-1} that was attributed to the NH stretching frequency. This is in line with our results on adsorbed NH. For the same surface, Mieher and Ho[85] assigned the feature at 1428 cm^{-1} to the NH deformation mode. However, our calculations suggest that this band should be attributed to the NH_2 scissoring mode appearing at 1454 cm^{-1}. The band above 1600 cm^{-1}, assigned by Mieher and Ho to the NH_2 scissoring mode, could be tentatively reassigned to the first overtone of the NH deformation mode.

From the above results, one can conclude that the N-H deformation region of the spectra is essential to correctly assign the predominant species on the surface. The intensity of the deformation band increases as the H-N surface angle decreases, i.e., the NH_3 umbrella mode is more intense than the NH_2 scissoring mode and the very weak NH deformation (108.5, 124, and 180°, respectively for Pt(100)). The NH_x symmetric stretching mode is the other feature characterizing these species, less intense than the corresponding deformation mode except for the NH species. However, all the NH_x stretching modes lie on a narrow interval (3330-3480 cm^{-1}). The most intense N-H stretching should be associated with the NH species.

Our results also support the hypothesis that NH_2 is the main fragment on the surface when reacting NO with a hydrogenprecovered Pt(100) surface.[6] In the 800-1500 cm^{-1} region, only a strong feature is observed. The observed band at 1450 cm^{-1} matches very well with the computed deformation mode of NH_2 (1467 cm^{-1}). Clearly, NH_3 is not present on the surface, as the band around 1100 cm^{-1} does not appear in the experimental spectra. However, according to the vibrational data, NH could be also present on the surface, if one only regards the deformation region, because the NH deformation mode does not cause any variation of the dynamic dipolar moment. So, focusing only on this region, the existence of adsorbed NH species cannot be excluded. From the N-H stretching region, the theoretical frequency values cannot discard any species. All active modes present frequencies of a similar magnitude (3348, 3379, and 3363 cm^{-1} for NH_3, NH_2, and NH, respectively), whereas they have very different RAIRS intensities. Comparing the intensities of the deformation and stretching regions in the theoretical and experimental spectra, it can be concluded that both NH_2 and NH are present on Pt(100). Nevertheless, the different adsorption energy of NH_2 and NH provides strong evidence that NH is a minority on Pt(100).

On Pt(111), similar conclusions can be extracted. The N-H stretching region provides a limited information about the identity of adsorbed NHx species. The deformation region of the spectra is the most important one. Ammonia can be identified from the presence of an intense band around 1100 cm^{-1} due to NH_3 symmetric deformation. NH_2 can be characterized via the NH_2 scissoring mode around 1450 cm^{-1}. The presence of NH is supported by the first overtone of NH deformation, 1600-1700 cm^{-1}. Both NH and NH_2 species coexist on the surface when NH_3 dehydrogenation takes place. The calculated relative stabilities of NH_x species on the Pt(111) surface give additional support to the presence of the NH fragment. Our results are consistent with the evolution of NH_x species obtained after electron irradiation and posterior annealing, performed by Sun *et al.*[7] All NH_x species are formed by electron irradiation (bands at 1088, 1392, and 3280 cm^{-1} for NH_3, NH_2, and NH, respectively). After annealing, NH_2 species are the first to vanish (accordingly to our energetic results) because the peak at 1392 cm^{-1} is not observed. At the same time, the remaining NH_3 starts to desorb (the band at 1188 cm^{-1} shifts to 1133 cm^{-1}, i.e., the NH_3 coverage is reduced) and NH_2 dehydrogenates to NH (the band at 830 cm^{-1} losses intensity and the NH stretching band increases). At 400 K, only the adsorbed NH species exist on the surface, and it is completely removed around 500 K, leading to atomic nitrogen on the surface.

3.4 Conclusions

The geometry, site preference, and relative stability of adsorbed ammonia and its dehydrogenated fragments (NH_x, x=0-3) on both Pt(100) and Pt(111) surfaces have been computed using periodic slab DFT calculations. NH_3 and NH_2 are more stable on Pt(100) than on Pt(111), while NH and N exhibit similar stabilities. A remarkable difference was found for NH_2, being 0.7 eV more stable on Pt(100), suggesting that the dehydrogenation of ammonia on platinum is structure sensitive. This result can be of special relevance in the mechanism of ammonia oxidation over noble metal catalysts. Our vibrational analysis shows that the fingerprint of NH_x species is the N-H deformation region. From the bands in this region, one could identify if NH_3 or NH_2 are present on the surface (an intense band below 1200 cm^{-1} or a band above 1400 cm^{-1}, respectively). Although NH could be also identified from the deformation mode between 800 and 900 cm^{-1}, well separated from the NH_3 and NH_2 deformation modes, the low intensity of the corresponding band exclude a clear identification. The N-H stretching region could present some bands with low intensity (depending on the coverage), but the obtained values in this region are similar for all the species. In general, the vibrational spectra of the different species on the (100) and (111) faces of platinum only present minor changes.

Chapter 4

Ammonia Dehydrogenation on Platinum Group Metals

Periodic DFT calculations using plane waves have been applied to comparatively study the adsorption and decomposition of ammonia on the (111) and (100) surfaces of platinum-group metals (Pd, Rh, Pt). Different adsorption geometries and positions have been studied for NH_3 and its dehydrogenation intermediates (NH_x, x=0-2). On the six surfaces investigated, NH_3 adsorbs preferentially on top sites, NH_2 on bridge, and NH and N on hollow sites. However, the adsorption energies of the NH_x moieties differ considerably from one surface to another. All of the species adsorb more strongly on the (100) than on the (111) planes. Rh(100) provides the maximum stability for the various intermediates. The reaction energies, the structure of the transition states, and the activation barriers of the successive dehydrogenation steps ($NH_x \rightarrow NH_{x-1} + H$) have been determined, making it possible to compute rate coefficients at different temperatures. Our calculations have confirmed that ammonia decomposition over noble metal catalysts is structure sensitive. As a general trend, the first dehydrogenation step is rate determining, especially for Pd. In agreement with experiments, Rh is a better catalyst for NH_3 decomposition than are Pt and Pd. The former strongly stabilizes the highly dehydrogenated NH and N species and also leads to the lowest activation barriers. For the set of dehydrogenation reactions, a linear relationship between the transition

---

This chapter is based on the following publication:
G. Novell-Leruth, A. Valcárcel, J. Pérez-Ramírez, J. M. Ricart; *J. Phys. Chem. C*, *2007*, 111 (2), 860.

state potential energy and the adsorption energy of the final state has been obtained.

4.1 Introduction

Catalytic conversions involving ammonia are of great relevance in the chemical industry. Accordingly, the interaction of ammonia with metal surfaces (particularly Fe, Ni, Cu, Ag, Pt, Ir, or Ru) has been thoroughly investigated.[116] Many of these studies were primarily undertaken to gain insight into the synthesis of ammonia. However, other processes, such as the oxidation of ammonia in nitric acid production,[117] the reaction of ammonia with methane to produce HCN,[118] and more recently the decomposition of ammonia to produce high-purity H_2 for fuel cells,[119–121] are of high practical importance too. In particular, platinum-group metals (PGM) and their alloys are superior catalysts for ammonia oxidation to NO (Ostwald process) and in the synthesis of HCN via the $NH_3 + CH_4$ reaction in the absence (Degussa process) or presence (Andrussow process) of O_2. Experimental assessment of the surface chemistry related to these reactions is intricate due to the demanding conditions of temperature and pressure and the very fast kinetics, which make the identification of elementary steps and key reaction intermediates unfeasible. Application of surface science techniques in UHV over platinum single crystals in a broad temperature range (300-1700 K),[81–88] and more recently the Temporal Analysis of Products (TAP) reactor over commercial Pt and Pt-Rh gauzes at 973-1173 K,[16–18] have provided valuable insights into the mechanism of the high-temperature ammonia oxidation. These studies demonstrated that the oxidation is initiated by dehydrogenation of the ammonia molecule by adsorbed oxygen atoms, leading to reactive NH_x intermediates. According to the hydride mechanism, the latter fragments end up in reaction products by further H-stripping, O-transfer into NH_x intermediates (forming NO), and coupling of N-species (forming N_2 and N_2O). However, despite many dedicated studies, a generally accepted atomic-level description as well as a systematic characterization of intermediate NHx species has not been achieved as yet. This information sets the basis for deriving rational microkinetic models able to predict the performance of PGM catalysts in ammonia conversion. On Pt(111) and Pt(100) surfaces, TPDS, HREELS, AES, and LEED studies in ultrahigh vacuum have shown that NH and NH_2 species are intermediates in ammonia oxidation.[82, 84] HREELS and TPRS studies also identified NH_2 species in the reaction between H and NO on Pt(100)-(1×1).[6] The various NH_x fragments have been also evidenced on Pt(111) upon electron bombardment of molecularly adsorbed ammonia at 100 K.[7,8] These authors have reported that adsorbed NH_2 species are dominant at subambient temperature. Dissociation of these species occurs in the temperature range of 300-400 K, and NH becomes the main surface species. On further heating, adsorbed NH dissociates and N_2 desorbs. Yamada and Tanaka, using HREELS, have also detected NH_x species while exposing a c(2×2)-N overlayer on Pd(100),[9,10] $Pt_{0.25}Rh_{0.75}$(100),[11] and Rh(100)[12] to H_2. They have concluded that the main surface species is NH, which is in line with the results by Herceg *et al.*[13] The latter authors have investigated the formation and dissociation chemistry of NH species on Pt(111) by using RAIRS and TPDS techniques. Theoretical ab initio approaches based on quantum chemical principles can contribute to a rational description of the complex ammonia dehydrogenation process. Despite outstanding theoretical studies in the topic of ammonia synthesis over a number of surfaces,[90,91,122] only few theoretical works have systematically examined the fragmentation of adsorbed NH_x species on Pt(111),[97,123,124] Pd(111),[125] and Rh(111).[126] In fact, ammonia dehydrogenation studies over (100) surfaces are to the best of our knowledge not reported in the literature. Our recent work[123] assessed the adsorption and relative stability of ammonia and the resulting dehydrogenated NH_x species (x=0, 1, 2) on Pt(111) and Pt(100) surfaces using periodic slab DFT calculations. NH_3 and NH_2 were found to be more stable on Pt(100) than on Pt(111), while NH and N exhibited similar stabilities. A remarkable difference was found for NH_2, being ca. 68 kJ·mol^{-1} more stable on Pt(100). On the basis of this, it was suggested that the dehydrogenation of ammonia on platinum is structure sensitive. This theoretical prediction has been substantiated in recent experimental work by Vidal-Iglesias *et al.*,[127] showing that the electrocatalytic oxidation of ammonia takes place almost exclusively on Pt(100) sites. In line with this, Rosca and Koper[128] have reported very different electrocatalytic NH_3 oxidation activities between Pt(100) and Pt(111), and related the higher rate of N_2 production over Pt(100) with the stabilization of the NH_2 adsorbate. On Pt(100), NH and N adsorbed species are stabilized, and reaction practically does not occur. More recently, Offermans *et al.*[124] have provided by means of DFT new mechanistic and kinetic insights into the ammonia oxidation on Pt(111), including also the NH_x dehydrogenation reactions. Following our previous study,[123] this work systematically investigates the non-oxidative dehydrogenation of ammonia over PGM surfaces. The structure, stability, and reactivity of adsorbed NH_3, NH_2 , NH, N, and H species have been comparatively analyzed over the (100) and (111) surfaces of the Pt, Rh, and Pd. The analogies and differences presented here comprise a first requisite to subsequently approach the influence of oxygen in the reaction.

4.2 Computational details

Calculations were performed in the frame of DFT using the Vienna Ab Initio Simulation Program (VASP).[55,57] This program solves the Kohn-Sham equations of the density functional theory with the development of the one-electron wave function in a basis of plane waves. The electron-ion interactions were described by the projector augmented wave (PAW) method.[99] The tight convergence of the plane-wave expansion was obtained with a cutoff of 400 eV. The generalized gradient approximation (GGA) was used with the functional of Perdew and Wang.[100] We considered the 2×2 unit cell associated with a molecular coverage of 1/4 ML. The 2D Brillouin integrations were performed on a 5×5×1 grid. The correct convergence of the adsorption energy by using this density of k-points was evaluated. For adsorbed NH_x fragments (x=0-2), a nonpolarized spin formalism was used because spin polarization effects were found to be negligible. The (100) and the (111) metal surfaces were modeled by a two-dimensional slab in a three-dimensional periodic cell generated by introducing a vacuum width of ca. 12 Å in the normal direction to the surface. The slabs contained four atomic metal layers with the target molecule and atomic species (NH_3, NH_2, NH, N, and/or H) adsorbed on one side of the slab. The optimized metal-metal interatomic distances for the bulk were used to prevent false forces on the metal atoms. The resulting calculated values (2.82 Å Pt-Pt, 2.80 Å Pd-Pd, and 2.72 Å Rh-Rh) were indeed close to those determined experimentally (2.77, 2.75, and 2.69 Å, respectively).[129] The energy of the bare surfaces was calculated permitting relaxation of the two top layers. The geometry optimization included all degrees of freedom of the adsorbates and the two uppermost metal layers, while the two lowest metal planes were fixed at the optimized bulk geometry. The adsorption energy (E_{ads}) was computed as the difference between the energy of the adsorbed molecule ($E_{NH_x-surface}$) and the sum of the free surface ($E_{surface}$) and the corresponding gas-phase species ($E_{gas-phaseNH_x}$) energies according to eq 4.1.

$$E_{ads} = E_{NH_x-surface} - E_{surface} - E_{gas-phase\,NH_x} \tag{4.1}$$

A negative value of E_{ads} indicates an exothermic chemisorption process. To compare the relative stabilities of the different species, the adsorption energies were recalculated with respect to a common reference system: the NH_3 molecule in the gas phase (eq 4.2). We considered that the adsorbed NH_x species and (3 - x)H atoms do not interact; that is, they are separated by infinite distance.

$$E_{rel} = (E_{NH_x-surface} + (3-x)\,E_{H-surface}) \\ - ((4-x)\,E_{surface} + E_{gas-phase\,NH_x}) \quad (4.2)$$

Reaction energies for the successive $NH_x \rightarrow NH_{x-1} + H$ (x = 1-3) dehydrogenation steps were computed in two ways depending on the selection of the final state and are denoted as ΔE_1 and ΔE_2. In ΔE_1, the reaction products were coadsorbed on the same cell, whereas in ΔE_2 the NH_{x-1} fragment and the H atom were at infinite distance on the surface. The Dimer method[70] was used to determine the transition states. The obtained results were refined until a negligible value of the forces with the quasi-Newton algorithm implemented in VASP. A full vibrational analysis was conducted to check the validity of both the optimized geometries and the determined transition states. The dynamical matrix was obtained by numerical differentiation of the forces and diagonalized, providing the harmonic molecular frequencies and the normal modes. These calculations made it possible (4.1) to include the zero point energy, ZPE (eq 4.3),

$$ZPE = \sum_i (1/2)\, h\nu_i \quad (4.3)$$

where ν_i are the computed real frequencies of the system, and (4.2) to calculate the rate coefficients (k_v) for the different elementary steps during ammonia dehydrogenation using the transition state theory in the harmonic approach:

$$k_v = \frac{kT}{h}\frac{Z_{TS}}{Z_{IS}} e^{-\frac{E_a}{kT}} = k_0 e^{-\frac{E_a}{kT}} \quad (4.4)$$

where Z_{IS} andZ_{TS} are the partition functions in the initial and transition states, respectively. In this equation, E_a is the ZPE corrected activation energy, k_0 is the pre-exponential factor, and k and h are the Boltzmann and Planck constants, respectively. Because NH_3 adsorbed on top sites behaves as a nearly free 2D rotator, its lowest frequency mode was considered as a rotation in the calculation of the partition functions.[124]

UNIVERSITAT ROVIRA I VIRGILI
CATALYTIC AMMONIA OXIDATION ON NOBLE METAL SURFACES: A THEORETICAL STUDY
Gerard Novell Leruth
ISBN:978-84-692-1534-0/ DL:T-377-2009

4.3 Results and discussion

Adsorption of ammonia

Ammonia was systematically adsorbed on different sites for each surface, that is, top, bridge, and hollow for (100) and top, bridge, and hollow fcc or hcp for the (111) surfaces. Adsorbed NH_3 was found to be favored on top sites on all metal surfaces, bound via the N atom and with the H atoms pointing outward. Any attempt to find a minimum of energy in the other symmetric sites led to the on top site after complete optimization, in agreement with previous theoretical studies of ammonia adsorption on transition metals.[92, 93, 103–105] The adsorption energies are presented in Table 4.1. Results corresponding to the Pt surfaces were presented and discussed in a previous paper,[123] but are included here to establish a comprehensive comparison with the other platinum-group metals. The values obtained for NH_3 adsorbed on Rh(100) (-82 $\mathrm{kJ \cdot mol^{-1}}$, -73 $\mathrm{kJ \cdot mol^{-1}}$ ZPE corrected) and Rh(111) (-76 $\mathrm{kJ \cdot mol^{-1}}$, -66 $\mathrm{kJ \cdot mol^{-1}}$ ZPE corrected) are in line with the earlier results reported by Liu *et al.*[126] and by Frechard *et al.*[130] using similar methods and models, and the results for Pd are in good agreement with the experimentally determined heat of adsorption on Pd foils (-72 $\mathrm{kJ \cdot mol^{-1}}$).[131] The zero point energy correction reduces the value of the adsorption energy by 10 $\mathrm{kJ \cdot mol^{-1}}$. The adsorption energy on the (100) surface is always higher than that on the (111) surface for all of the metals, although the differences between the two planes over the same metal are relatively small ($<$12 $\mathrm{kJ \cdot mol^{-1}}$). The order of stability of adsorbed ammonia on the metals is Rh $>$ Pt $>$ Pd. Among all of the minima (Table 4.1), there are no significant differences in the metal-nitrogen distances (dM-N), which are about 2.15 Å, and the N-H distances (1.020 Å) do not change with respect to those in the gas phase (1.024 Å).

Adsorption of NH_x fragments

Table 4.1 shows the adsorption energies and geometrical parameters of the various NH_x fragments (x = 0-2) on their more stable adsorption site. The other sites lead to less stable adsorbed states or are not minima. All of the species chemisorb molecularly in a N-down orientation. NH_2 preferentially adsorbs on the bridge site, with the molecular C_2-axis perpendicular to the surface, whereas NH and N prefer the hollow sites on both (100) and (111) surfaces. The main difference is that the most stable adsorption site is the hollow hcp on Rh(111), whereas the hollow fcc is the preferred one on Pt(111) and Pd(111). However, the energy difference between the two hollow sites is

Table 4.1: Adsorption energies (in kJ·mol^{-1}) of the different fragments with respect to each species in the gas phase; Distance from N to the closest metal atom (d$_{M-N}$), N-H distance (d$_{N-H}$), and height from the surface layer (z) (distances in angstroms)

	Pt(100)	Pd(100)	Rh(100)	Pt(111)	Pd(111)	Rh(111)
			NH_3			
Site	top	top	top	top	top	top
E_{ads}	-76	-64	-82	-68	-55	-76
E_{ads}(ZPE)	-66	-56	-73	-58	-46	-66
d$_{M-N}$	2.13	2.17	2.15	2.16	2.18	2.15
d$_{N-H}$	1.02	1.02	1.02	1.02	1.02	1.02
z	2.13	2.17	2.15	2.15	2.17	2.15
			NH_2			
Site	bridge	bridge	bridge	bridge	bridge	bridge
E_{ads}	-300	-266	-321	-241	-235	-278
E_{ads}(ZPE)	-279	-248	-302	-221	-217	-260
d$_{M-N}$	2.06	2.06	2.06	2.09	2.07	2.08
d$_{N-H}$	1.02	1.02	1.02	1.02	1.02	1.02
z	1.42	1.45	1.52	1.52	1.51	1.59
			NH			
Site	hollow	hollow	hollow	fcc	fcc	hcp
E_{ads}	-378	-407	-489	-406	-387	-443
E_{ads}(ZPE)	-360	-390	-472	-385	-363	-426
d$_{M-N}$	2.18	2.12	2.13	2.01	1.99	2.01
d$_{N-H}$	1.03	1.03	1.03	1.02	1.03	1.02
z	0.91	0.81	0.93	1.07	1.08	1.19
			N			
Site	hollow	hollow	hollow	fcc	fcc	hcp
E_{ads}	-422	-486	-561	-467	-451	-516
E_{ads}(ZPE)	-417	-478	-544	-458	-441	-508
d$_{M-N}$	2.11	2.02	2.04	1.96	1.92	1.92
z	0.75	0.05	0.68	1.01	1.00	1.05
			H			
Site	bridge	hollow	hollow	fcc	fcc	fcc
E_{ads}	-276	-263	-275	-266	-281	-279
E_{ads}(ZPE)	-260	-257	-267	-252	-264	-260
d$_{M-H}$	1.76	1.99	2.01	1.87	1.81	1.86
z	1.02	0.34	0.60	0.86	0.79	0.96

rather small. On Rh the hcp site is the preferred one only by 2 kJ·mol^{-1} (NH) and 12 kJ·mol^{-1} (N). On Pt and Pd, the fcc is the preferred adsorption site by 38 and 18 kJ·mol^{-1} for NH and by 27 and 13 kJ·mol^{-1} for N, respectively. A small hcp-fcc energy gap suggests that both sites are populated to a similar extent. Besides, this fact shows that the second metal layer does not significantly influence the adsorption. We anticipate that the transition states will follow the same trends, and we took the most stable sites for further calculations. Our results for both preferred adsorption site and binding energy are in good agreement with data available in the literature: N on Rh(111), -521 kJ·mol^{-1}[132] and -493 kJ·mol^{-1};[133] N on Pt(100), -414 kJ·mol^{-1};[134] N on Rh(100), -548 kJ·mol^{-1};[134] NH_2, NH, N on Pt(111), -298, -387, and -449 kJ·mol^{-1}[124] or -221, -369, and -420, respectively;[98] NH_2, NH, N on Rh(111), -263, -423, and -473 kJ·mol^{-1}.[126] As observed for NH_3, the adsorption energies of the fragments (Table 4.1) are generally higher on the (100) surface than on the (111) surface for the different metal surfaces. As a general trend, the order of stability is Pd(111) $<$ Pt(111) $<$ Pd(100) $<$ Rh(111) $<$ Pt(100) $<$ Rh(100), although NH and N on Pt(100) are less stable than expected following this tendency, as discussed elsewhere.[123] The surface providing maximum stability to the adsorbed species is Rh(100). This is consistent with the general consensus that as the metal d occupancy increases, the covalent bonding ability of the metal surface decreases. For a particular species, the geometrical parameters are similar on Pd, Rh, and Pt. As expected, the equilibrium distance perpendicular to the surface decreases in the order $NH_3 > NH_2 > NH > N$, being smaller for the (100) surfaces than for the (111) surfaces (Table 4.1). It is interesting to note that in the case of Pd(100), N is coplanar with the surface. This draws parallels to other N/metal systems, such as N on Ni(100).[135]

Adsorption of H species

An accurate description of the adsorption properties of H is relevant to this study because the energy of the H-metal system is necessary to compute and compare the relative stabilities of the NH_x moieties (eq 4.2). Besides, the structure of the transition states can be strongly influenced by the different stability of atomic hydrogen on the various surface sites. Table 4.2 summarizes the present results. As it is well established in the literature,[136–139] the hollow fcc is always the most stable adsorption site for H on the (111) surfaces. In the case of Pt(111), all of the sites are energy minima. On the other hand, on Pd(111) the top and bridge sites are second-order and first-order stationary points, respectively, and on Rh(111) the bridge site is a saddle point. In all of the cases, the difference between hcp and fcc sites is very small (<4 kJ·mol^{-1}),

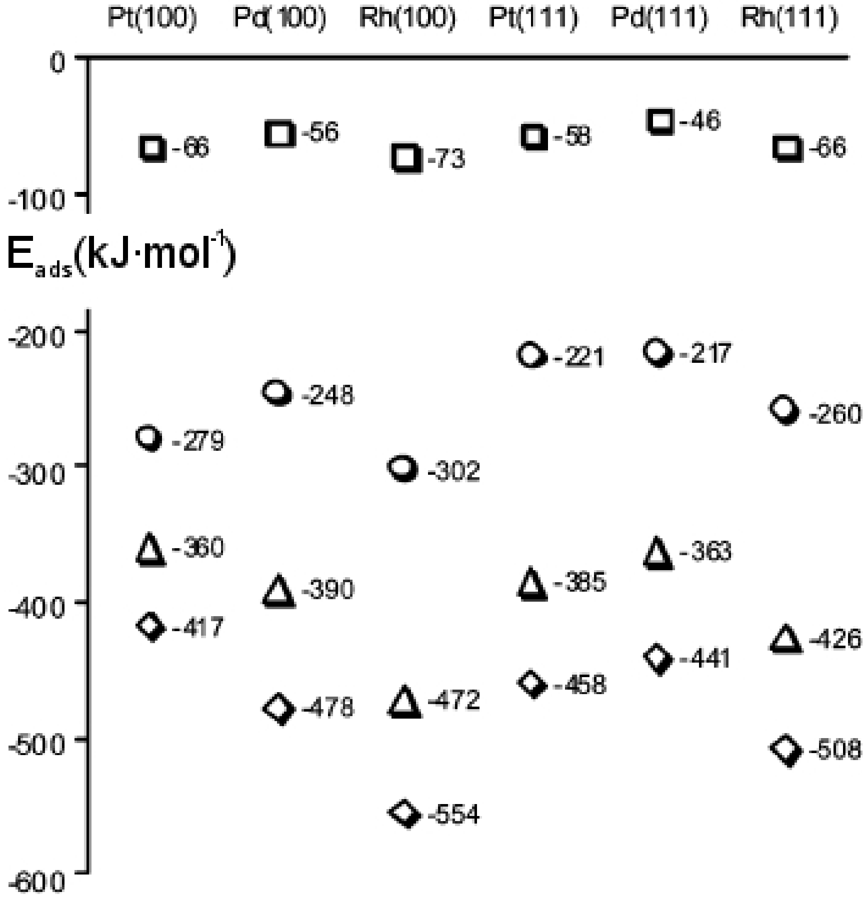

Figure 4.1: Adsorption energy (kJ·mol^{-1}, ZPE included) of the different fragments (□, NH_3; ◯, NH_2; △, NH; ◇, N) with respect to each species in the gas phase.

Table 4.2: Adsorption energy (kJ·mol^{-1}) of atomic hydrogen on the symmetric sites of the surfaces. Energies were computed with respect to the gas-phase H_2 molecule and include the ZPE correction.

	top	bridge	hollow	
Pt(100)	-35	-54	-31[a]	
Pd(100)	1[a]	-40	-50	
Rh(100)	-25[a]	-53	-60	
	top	bridge	hcp	fcc
Pt(111)	-39	-42	-42	-46
Pd(111)	-9[a]	-46[b]	-54	-58
Rh(111)	-18	-44[b]	-51	-54

[a]Second-order saddle point. [b]Firstorder saddle point.

and diffusion from a hollow site to another one should occur across the bridge sites. The picture for the (100) plane is similar. On Pt(100), the on top and bridge sites are minima, whereas the hollow site is a second-order saddle point. The bridge site corresponds to the absolute minimum. This has also been found using a semiempirical theoretical approach,[140] although no clear experimental evidence has so far confirmed this result.[141] On Pd(100) and Rh(100), the hollow site is the most stable one in agreement with previous theoretical and experimental studies.[142–145] On both metal surfaces, the top site is a second-order stationary point.

Dehydrogenation reactions

The adsorption energy of the NH_x species on the metals with respect to the same species in the gas phase increases in the order $NH_3 < NH_2 < NH < N$ (Table 4.1 and Figure 4.3). As expected, this trend coincides with the increasing instability of these species in the gas phase. We recomputed the adsorption energies using eq 4.2. The results, shown in Figure 4.3, clearly evidence that adsorbed $NH_2 + H$ is more stable than adsorbed NH_3 on Pt(100), Rh(100), and Rh(111), while the contrary applies on the other surfaces. Moreover, the NH and N moieties are strongly stabilized on Rh. In view of the relative stability of the different ammonia fragments, we can suggest that NH_2 is the predominant intermediate species during ammonia dehydrogenation on Pt(100). For Pd(100), Pt(111), and Pd(111), all of the dehydrogenated species exhibit a similar stability, and they are expected to equivalently populate the catalyst surface. In the case of Rh(100) and Rh(111), NH and N are much

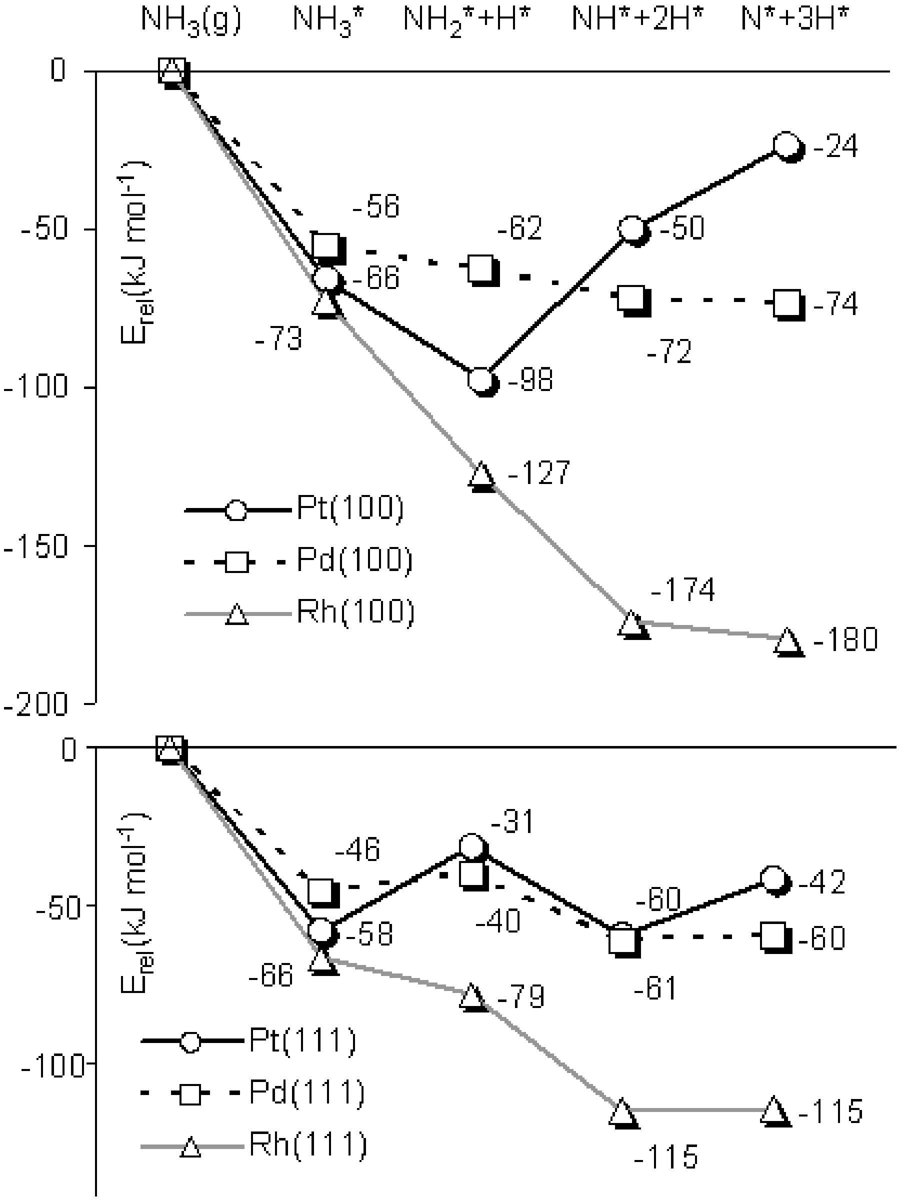

Figure 4.2: Relative adsorption energy (E_{rel} in kJ·mol^{-1}, ZPE included) of the NH$_x$ species with respect to gas-phase NH$_3$.

more stable than NH_2. Thus, rhodium surfaces strongly stabilize the presence of highly dehydrogenated products. Figure 4.3 displays the schematic reaction energy profile for the successive dehydrogenation steps. For each step, the starting point was a NH_{3-x} species (x=0-2) plus x adsorbed H atoms without lateral interactions. The final state was taken as NH_{3-x-1} plus one H atom coadsorbed on the same 2×2 unit cell in their most stable configuration and x adsorbed H atoms at infinite distance. The energy of NH_{3-x-1} plus (x+1) coadsorbed hydrogen atoms at infinite distance as the starting point for the following step was considered. The reaction profiles are similar on the (111) surfaces, although all of the species are highly stabilized on Rh. On the other hand, when considering the (100) surfaces, Pt behaves in a singular way. The NH and N species are less stabilized than expected. The difference between Pt(100) and Pt(111) and the different stability of NH_2 compared with NH and N are in very good agreement with the recent results by Rosca and Koper.[128] These authors have related the relatively high electrocatalytic activity of Pt(100) for ammonia oxidation to dinitrogen to its ability to stabilize the NH_2 adsorbate. Figure 4.3 presents the geometry of initial, transition, and final states corresponding to the most stable situation on the 2 × 2 unit cell for all of the elemental dehydrogenation reactions. Various transition states were identified for several reactions, as reported in the literature.[122,126] This is attributed to different possibilities for hydrogen migration. For the sake of conciseness, we only report here results for the most stable transition state in each reaction. Table 4.3 summarizes the geometrical parameters, the energy barriers, and the reaction energies for all of the reactions and surfaces studied. The zero point energy (ZPE) correction changes the activation barriers significantly (15-25 $kJ\cdot mol^{-1}$). This is due to the loss of a N-H bond in the transition state. The huge N-H frequency evolves to an imaginary one. Accordingly, this case further exemplifies the importance of the ZPE term in computational studies. The various elementary steps will be further analyzed below. $NH_3 \rightarrow NH_2 + H$. The lowest activation energy for the first proton abstraction of ammonia corresponds to Rh(100). The other values lie in the range 91-106 $kJ\cdot mol^{-1}$. On the (111) plane, the geometry of the transition state is different on the three metals studied. On Pt(111), both the NH_2 fragment and the H atom remain on a top position. On Pd(111) and Rh(111), the H atom is close to a bridge position. On the other hand, the final state corresponds to a NH_2 species adsorbed on a bridge position and the H atom on the neighboring fcc site. Our results on the Pt(111) surface are in line with those recently reported by Offermans *et al.*[124] and Michaelides and Hu.[96] In the case of Rh(111), the geometry of the transition state is close to the one reported by Liu *et al.*[126] These authors have studied the reverse hydrogena-

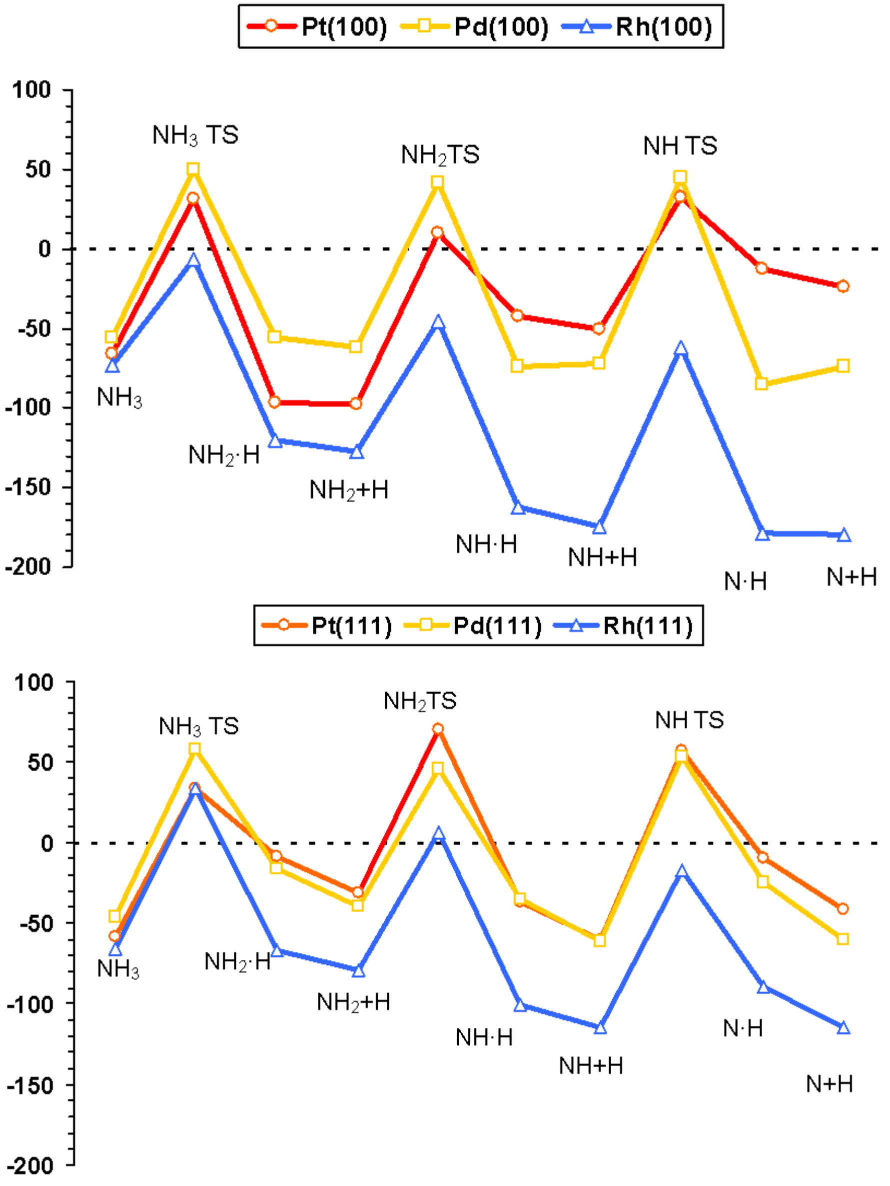

Figure 4.3: Reaction pathway for NH_3 dehydrogenation on the (100) and (111) surfaces. Energies in kJ·mol^{-1}, ZPE included.

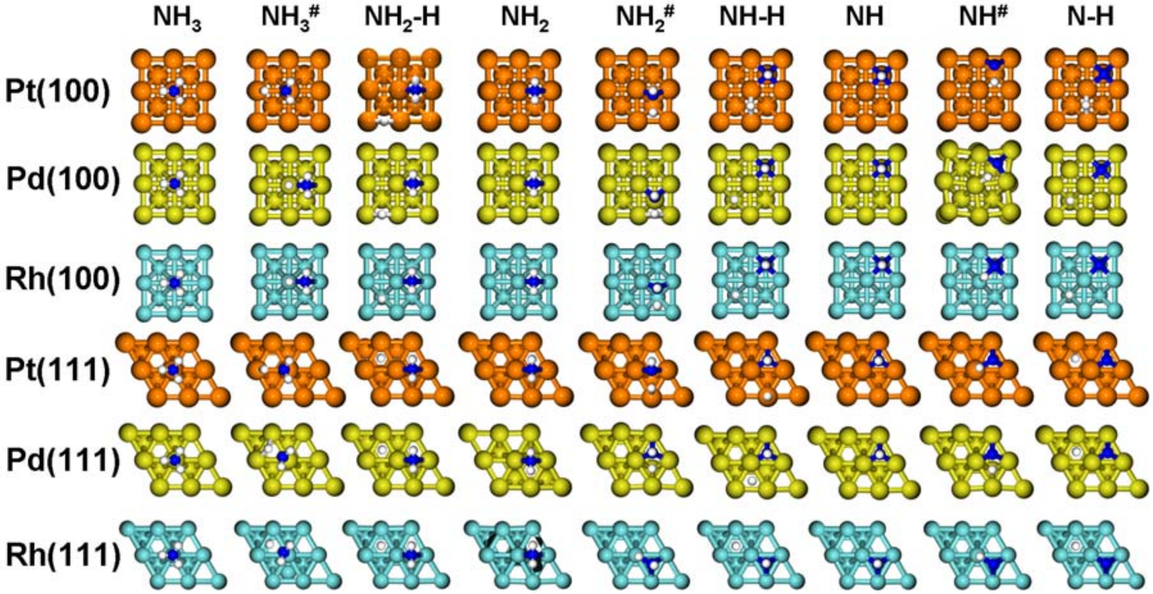

Figure 4.4: Top view of the initial, transition, and final states for the dehydrogenation reactions on the (100) and (111) metal surfaces.

tion reactions on Rh(111). They have reported a barrier of 120 kJ·mol^{-1} for the NH_2 + H → NH_3 reaction, which is coincident with the value determined from our present calculations. On the (100) surfaces, the geometry of the transition state is roughly the same for Pt, Pd, and Rh (see Figure 4.3). The NH_2 moiety is always positioned on a bridge site, while the H atom sits on top. In the final state, the NH_2 remains on the bridge site and the hydrogen atom gets adsorbed on a bridge site of Pt and Pd and on a 4-fold hollow site on Rh. NH_2 → NH + H. Similarly to the first dehydrogenation, the reaction barriers of the second dehydrogenation step lie in a narrow range (see Table 4.3). Again, the Rh(100) surface leads to the lowest activation energy. On the (100) surfaces, the geometries of the transition states are very similar, the NH fragment stays in the vicinity of a bridge site, whereas H is close to the nearest parallel bridge site. The barriers are similar for Pt and Pd and lower for Rh. The reaction is endothermic for Pt, athermic for Pd, and exothermic for Rh. On the (111) surfaces, the geometry of the lowest energy transition state is different on the three metals. On Pt, the NH species remains on the bridge position and H moves to the nearest top position. On Pd and Rh, the NH fragment moves to a fcc (Pd) or to a hcp position (Rh), whereas the H atom shifts to fcc (Pd) or top (Rh). These results find correspondence with Offermans *et al.*[124] on Pt(111), Crawford and Hu[122] on Pd(111) and Rh(111), and Liu and co-workers[126] on Rh(111). Our geometric parameters are in line with those previously reported. The only difference arises from the position of the H atom on Pd. Crawford and Hu[122] have found that H adsorbs close to a hcp position, whereas our calculations predicted a fcc adsorption site. The activation energies are also in good agreement with the results of Offermans *et al.*[124] and Liu and co-workers.[126] Unfortunately, the reaction barriers were not reported in ref.[122] NH → N + H. The activation energy of the last dehydrogenation step is the highest one for all of the metal surfaces except for Pt(100). The reaction barrier over Pt(100) is relatively low (82 kJ·mol^{-1}) as compared to the activation energies on Pd and Rh (118 and 113 kJ·mol^{-1}, respectively). On Pt(100), the transition state is similar to the one for NH_2, NH and H being close to two parallel bridge positions. However, on Pd(100) and Rh(100), the N atom reaches the hollow position with the H atom close to a top site. Interestingly, for Pd(100), a "clock" reconstruction of the surface was obtained similar to that reported for N on Ni(100).[146] For Pt(111) and Rh(111), the N fragment and the H atom in the most stable transition state lie on hollow and top positions, respectively, as reported by Offermans *et al.*[124] and Liu *et al.*[126] For Pd(111), the transition state with H in a position intermediate between hcp and bridge is the preferred one. This is also in agreement with the results from Crawford and Hu.[122]

4.4 Microkinetics

Table 4.4 gives the pre-exponential factors and rate coefficients at selected temperatures, as determined by eq 4.4. These results have to be considered semiquantitative due to the several approximations used in the theoretical treatment (the density functional, the reduced number of layers in the slab model, the harmonic approximation, and the fact that the surface phonons were neglected in the frequency calculations). On the (100) surfaces, NH_3 dissociates much easier on Rh than on Pt or Pd, the latter two being very similar. For the NH_2 dissociation, a similar trend was obtained. However, this tendency is not followed by NH. The last dehydrogenation is more favorable over Pt, followed by Rh and Pd. On the basis of these results, we can suggest that the first dehydrogenation is the rate-determining step on Pt(100) and Pd(100). On the other hand, on Rh(100), the first step is relatively fast and the $NH \rightarrow N + H$ step limits the reaction rate. On the (111) surfaces, the trends are similar. Nevertheless, the differences between the reaction rates lie in a narrow range. Interestingly, the trends that could be extracted from the simple analysis of the activation energies are modulated when including the effect of temperature, especially for the first dehydrogenation step. This illustrates the importance of taking into account the statistical thermodynamics in reactivity studies. This is because adsorbed NH_3 presents higher configurational entropy than the activated complex due to the nearly free rotation of NH_3 adsorbed on top site. As a consequence, the preexponential factors for the first dehydrogenation step are the lowest ones. The decomposition of NH_3 into N_2 and H_2 has been investigated over polycrystalline Pt, Rh, and Pd wires in a differential flow reactor, at pressures from 0.01 to 1 Torr and temperatures from 500 to 1900 K.[131] It has been found that Rh is more active than Pt and Pd and that the rate of product formation can be described by a Langmuir-Hinshelwood unimolecular model. The determined heats of NH_3 adsorption are very similar over the three metals (67-71 $kJ\cdot mol^{-1}$). However, Pd (109 $kJ\cdot mol^{-1}$) exhibited a higher apparent activation energy than did Pt and Rh (88 $kJ\cdot mol^{-1}$). Thus, the experimentally determined order of activity between the metals is excellently supported by our calculations. The higher activity of Rh over Pt and Pd is due to the lower activation barrier for the $NH_3 \rightarrow NH_2 + H$ reaction as well as to the enhanced stabilization of the various intermediates involved.

Table 4.3: Geometries of the transition states, activation energy barriers (E_{act}), and reaction energies with respect to the coadsorbed fragments on the 2×2 cell in the most stable configuration (ΔE_1), and with respect to the sum of the binding energies of the isolated fragments in their most stable adsorption site (ΔE_2). Energies in kJ·mol^{-1} include the ZPE. Distances in angstroms.

	Pt(100)	Pd(100)	Rh(100)	Pt(111)	Pd(111)	Rh(111)
			$NH_3 \rightarrow NH_2 + H$			
E_{act}	97	106	67	91	104	100
ΔE_1	-31	0	-47	49	30	0
ΔE_2	-32	-7	-54	26	6	-12
site N	bridge	bridge	bridge	top	top	top
site H	top	top	top	top	bridge	bridge
d_{M-N}	2.33	2.18	2.18	2.04	2.04	2.03
d_{N-H}	1.49	1.59	1.43	1.90	1.77	1.69
d_{M-H}	1.62	1.59	1.65	1.60	1.79	1.87
			$NH_2 \rightarrow NH + H$			
E_{act}	107	104	82	101	86	84
ΔE_1	56	-12	-35	-5	5	-22
ΔE_2	48	-10	-47	-28	-21	-36
site N	bridge	hollow	bridge	bridge	fcc	hcp
site H	bridge	bridge	bridge	top	hcp	top
d_{M-N}	2.00	2.08	1.96	2.03	2.04	2.09
d_{N-H}	1.64	1.52	1.57	1.68	1.43	1.41
d_{M-H}	1.88	1.75	1.84	1.62	2.00	1.66
			$NH \rightarrow N + H$			
E_{act}	82	118	113	116	114	98
ΔE_1	37	-13	-4	50	36	26
ΔE_2	26	-1	-5	18	1	1
site N	bridge	hollow	hollow	fcc	fcc	hcp
site H	bridge	hollow	top	top	hcp	top
d_{M-N}	1.92	1.94	2.13	2.11	1.98	2.03
d_{N-H}	1.53	1.48	1.53	1.52	1.42	1.51
d_{M-H}	1.90	1.70	1.65	1.63	1.89	1.63

Table 4.4: Pre-exponential Factors (k_0, s^{-1}), activation energies (E_{act}, kJ·mol^{-1}), and rate coefficients (k_v, s^{-1}) at 300, 500, and 700 K for the three successive elementary steps involved in ammonia dehydrogenation.

	k_0				k_v		
	300	**500**	**700**	E_{act}	**300**	**500**	**700**
Pt(100)							
$NH_3 \rightarrow NH_2 + H$	2.5×10^{11}	3.7×10^{11}	5.1×10^{11}	97	5.5×10^{-6}	36	3.6×10^{4}
$NH_2 \rightarrow NH + H$	5.0×10^{12}	9.3×10^{12}	1.4×10^{13}	107	9.8×10^{-7}	55	1.4×10^{5}
$NH \rightarrow N + H$	4.9×10^{12}	7.4×10^{12}	9.9×10^{12}	82	3.0×10^{-2}	2.2×10^{4}	8.0×10^{6}
Pd(100)							
$NH_3 \rightarrow NH_2 + H$	1.8×10^{11}	2.4×10^{11}	3.1×10^{11}	106	7.8×10^{-8}	2.3	4.1×10^{3}
$NH_2 \rightarrow NH + H$	4.9×10^{12}	7.3×10^{12}	9.5×10^{12}	104	3.8×10^{-6}	99	1.6×10^{5}
$NH \rightarrow N + H$	8.3×10^{12}	9.7×10^{12}	1.3×10^{13}	118	1.9×10^{-8}	4.9	2.2×10^{4}
Rh(100)							
$NH_3 \rightarrow NH_2 + H$	2.5×10^{11}	3.1×10^{11}	3.9×10^{11}	67	5.7×10^{-1}	3.3×10^{4}	4.1×10^{6}
$NH_2 \rightarrow NH + H$	4.3×10^{12}	6.7×10^{12}	9.3×10^{12}	82	2.6×10^{-2}	2.0×10^{4}	7.5×10^{6}
$NH \rightarrow N + H$	8.3×10^{12}	1.6×10^{13}	2.3×10^{13}	113	2.0×10^{-7}	27	9.1×10^{4}
Pt(111)							
$NH_3 \rightarrow NH_2 + H$	4.6×10^{11}	7.1×10^{11}	1.0×10^{12}	91	6.1×10^{-5}	2.1×10^{2}	1.5×10^{5}
$NH_2 \rightarrow NH + H$	5.8×10^{12}	1.1×10^{13}	1.6×10^{13}	101	1.3×10^{-5}	2.2×10^{2}	3.1×10^{5}
$NH \rightarrow N + H$	7.2×10^{12}	1.3×10^{13}	1.9×10^{13}	116	4.1×10^{-8}	9.3	3.9×10^{4}
Pd(111)							
$NH_3 \rightarrow NH_2 + H$	4.9×10^{11}	8.5×10^{11}	1.3×10^{12}	104	4.2×10^{-7}	12	2.4×10^{4}
$NH_2 \rightarrow NH + H$	4.0×10^{12}	5.8×10^{12}	7.8×10^{12}	86	3.9×10^{-3}	5.7×10^{3}	2.9×10^{6}
$NH \rightarrow N + H$	7.9×10^{12}	1.6×10^{13}	2.7×10^{13}	114	9.6×10^{-8}	9.3	7.9×10^{4}
Rh(111)							
$NH_3 \rightarrow NH_2 + H$	7.3×10^{11}	1.5×10^{12}	2.7×10^{12}	100	3.3×10^{-6}	59	9.8×10^{4}
$NH_2 \rightarrow NH + H$	5.6×10^{12}	9.0×10^{12}	1.2×10^{12}	84	1.2×10^{-2}	1.4×10^{4}	6.2×10^{6}
$NH \rightarrow N + H$	7.1×10^{12}	1.2×10^{13}	1.6×10^{13}	98	5.8×10^{-5}	6.8×10^{2}	7.8×10^{5}

UNIVERSITAT ROVIRA I VIRGILI
CATALYTIC AMMONIA OXIDATION ON NOBLE METAL SURFACES: A THEORETICAL STUDY
Gerard Novell Leruth
ISBN:978-84-692-1534-0/ DL:T-377-2009

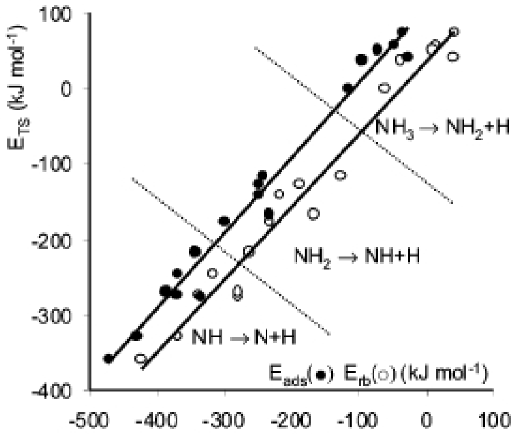

Figure 4.5: Transition state potential energy (E_{TS}) versus the adsorption energy of the reaction products (E_{ads}, ●) and rebonding energy (E_{rb}, ○) for all of the transition states computed in this work. For each point, the zero-energy reference is the one of each reacting species in the gas phase.

4.5 Energy relationships

It has long been realized that the potential energy of the transition state with respect to the adsorbed molecule in the gas phase (E_{TS}) and the adsorption energy (E_{ads}) of the final products with respect to the same reference are often correlated.[96, 113, 146–148] This Brønsted-Evans-Polany (BEP)-type relationship also applies in the present study where $E_{TS} = 0.99E_{ads} + 107$ (in kJ·mol^{-1}) with $R^2 = 0.977$ (see Figure 4.5). Interestingly, this correlation is very similar to the one found by Nørskov *et al.*[147] for N_2, CO, NO, and O_2 dissociation on several metal surfaces. These authors have proposed that this can be linked to the fact that the bond length in the transition state is quite long. Therefore, the variation in the energy of the transition state follows that of the final state, and it gives a linear relationship between these two energies with a slope close to the unity. Loffreda *et al.*[113] have found similar trends for NO dissociation. They have shown that the transition state is "late" on the reaction path and concluded that the stability of the transition state and the value of the barrier are governed by the strength of the atom surface interaction, that is, by the stability of the final coadsorbed N + O state. All of the dehydrogenation steps of the present study follow similar trends.

In all of the cases, the elongated N-H bond in the transition state is nearly broken (see Table 4.3). However, the above correlation should be taken with caution because it depends strongly on the adsorption energy of each reacting species. In fact, the correlation (R^2) for each single step is much lower than 0.9 ($R^2 = 0.584$, 0.670, and 0.783 for the consecutive dehydrogenation reactions). Interestingly, we did not obtain a significant correlation between the activation energy barriers and the reaction energies. This result has yet been reported by Offermans *et al.*[124] These authors have found a trend in the activation energy versus the reaction energy of dehydrogenation reactions on Pt(111), but a linear relationship is not applicable in an useful way. Hammer[148] has proposed another relationship between the calculated adsorption energy of the transition state and the "rebonding energy", E_{rb}, defined as the sum of the individual chemisorption energies of the final fragments in the geometry of the transition state. With this definition, $E_{TS} = E_{rb} + E_{int}$, where Eint is the intramolecular repulsive interaction of the fragments in the transition state. The correlation between E_{rb} and E_{TS} is also presented in Figure 4.5: $E_{TS} = 0.96E_{rb} + 35.8$ ($R^2 = 0.968$). This correlation shows that, although E_{int} is not constant, the variations remain small. All of these relationships represent only qualitative trends because a particular elementary step may deviate considerably from the relation. They may be useful to estimate apparent activation energies from adsorption energies. However, our results further confirm that the Brønsted-Evans-Polany relationship should be analyzed for any particular problem.

4.6 Conclusions

Using periodic slab DFT calculations, we have successfully computed the geometry, site preference, and relative stability of adsorbed ammonia and its dehydrogenated fragments (NH_2, NH, N) on the (100) and (111) surfaces of Pd, Rh, and Pt. The adsorption energy is higher on the more open (100) plane than on the (111) one for all of the metals. Moreover, the adsorption energies are stronger on Rh than on Pd or Pt. On the six metal surfaces, NH_3 adsorbs on top sites, NH_2 on bridge, and NH and N on hollow sites. The N-H and M-N distances are similar for all of the species. The differences between the three metals are more significant on the (100) than on the (111) surfaces. The transition states and reaction barriers for the successive dehydrogenation steps have also been determined. All of the barriers range between 67 kJ·mol^{-1} ($NH_3 \rightarrow NH_2 + H$ on Rh(100)) and 118 kJ·mol^{-1} ($NH \rightarrow N + H$ on Pd(100)). As a general trend, the barriers are higher for the last dehydrogenation step (except for Pt(100)). However, once the kinetic constants are computed, the rate-determining step corresponds to the first hydrogen abstraction (except for Rh(100)) due to the negative activation entropy of this step. On Pd(111) and Pt(111), all of the transition states are above the energy of NH_3 in the gas phase, while on Rh(111) all of the species are more stable than adsorbed ammonia. On the (100) surfaces, the energy of the different adsorbed intermediates and transition states is higher on Pt and Pd than on Rh. It is also seen that in the case of Rh, all of the transition states are below the energy of gas-phase NH_3. Thus, according to our calculations, Rh should be a more active catalyst for NH_3 decomposition than Pt or Pd, in agreement with experimental results reported in the literature. We have found a linear relationship between the transition state potential energy and the adsorption energy of the final state for the set of dehydrogenation reactions. However, a significant correlation between the activation energies and the reaction energies has not been obtained. Therefore, the original Brønsted-Evans-Polany relationship cannot be taken as a universal rule in heterogeneous catalysis.

Chapter 5

Ammonia Oxidation on Pt(100)

Density functional theory simulations were used to study the mechanism of ammonia oxidation over Pt(100). The conversion of NH_3 leading to NH_x intermediates upon reaction with adsorbed oxygen-containing species and ultimately forming reaction products (NO, N_2O, N_2, and H_2O), have been systematically computed. The reaction proceeds via an imide mechanism, while classical mechanisms postulating nitroxyl and hydroxylamine as reaction intermediates may be excluded. The barriers of oxidative NH_3 dehydrogenation over Pt(100) are drastically decreased with respect to the nonoxidative dehydrogenation, particularly when the number of hydrogen atoms in the NH_x fragment is decreased. Ammonia activation and subsequent NH_x dehydrogenation steps are greatly favored by O_{ads} with respect to OH_{ads} on Pt(100). This differs from calculations on Pt(111) due to the metal sharing effect and to the lower stability of adsorbed hydroxyl in the latter facet. Nitrogencontaining products are formed by recombination of chemisorbed N with N (N_2), O (NO), and NO (N_2O). Water is formed via recombination of adsorbed OH, regenerating an active O. The O-mediated abstraction of the first proton of NH_3 is the slowest dehydrogenation step, whereas NO desorption determines the rate of the overall process. Rate coefficients of the elementary steps involved in the mechanism have been calculated, enabling a microkinetic analysis of the reaction. Our simplified model predicts reasonably well the product distribution

---

This chapter is based on the following publication:
G. Novell-Leruth, J. M. Ricart, J. Pérez-Ramírez; *J. Phys. Chem. C*, *2008*, 112 (35), 13554.

obtained experimentally at different temperature, time, and NH_3/O_2 ratio.

5.1 Introduction

In 1838, i.e., two years after Berzelius coined the term "catalytic force", Kuhlmann filed a patent for the oxidation of ammonia in air over platinum sponge to form nitric oxide.[2] This formed the basis for the present-day manufacturing process of nitric acid, which was developed by Ostwald in the early 1900s and implemented on a large scale in the 1920s.[149] A major change in the catalyst occurred in the 1930s, when the beneficial effect of rhodium addition to the platinum gauzes was discovered.[5] The resulting Pt-Rh alloy, typically containing 90-95% Pt, have been used with little modifications ever since.[3]

The mechanism of ammonia oxidation on Pt has been investigated for more than 80 years. Three main theories were postulated in the period 1926-1935, making reference to the reaction intermediate leading to the final products: the nitroxyl (HNO) mechanism by Andrussow,[21] the imide (NH) mechanism by Raschig,[23] and the hydroxylamine (NH_2OH) mechanism by Bodestein.[22] However, experimental evidence of the intermediate species in question was not convincingly obtained. The development of surface science techniques under ultrahigh vacuum revitalized the interest to unravel the ammonia oxidation mechanism. Pioneering works by Fogel *et al.* using SIMS[150] and Nutt and Kapur using molecular beams[151] provided overall reaction pathways leading to NO and N_2. These were followed by a number of outstanding UHV studies with platinum single crystals (Pt(111),[84,85] Pt(100),[86,88] Pt(s)-12(111)×(111),[81] Pt(533) and Pt(433)[152,153]), which further characterized the surface reactions between oxygen, ammonia, and nitric oxide. Most of these studies have concluded that the reaction proceeds via the successive stripping of hydrogen of the ammonia molecule catalyzed by adsorbed oxygen or hydroxyl species. The sogenerated N atoms can recombine with O to form NO or with N to form N_2; the selectivity namely depends both on oxygen coverage and temperature. The mechanistic complexity is even higher, since N_2O is an additional reaction product in ammonia burner. However, nitrous oxide has not commonly been detected in UHV investigations and consequently the reaction has been categorized as biphasic.[88] Application of the temporal analysis of products (TAP) reactor, a transient pulse technique, made it possible to overcome the intrinsic pressure gap of UHV studies, uncovering the origin of N_2O at peak pressures in the reactor of 20 mbar.[16–18,97] The latter studies were carried out over commercial Pt and $Pt_{0.95}$-$Rh_{0.05}$ gauzes and enabled to study the reaction isothermally. This is the limitation of traditional approaches at ambient pressure, since phenomena like ignition, extinction, oscillations, and surface reconstruction often originate falsified kinetic data. The very fast kinetics of ammonia oxidation makes the experimental identification of elementary steps and key intermediates unfeasible. Therefore, despite substantial and long-standing efforts, a generally accepted molecular-level description of the reaction has not been attained. Achieving this knowledge will make headway for deriving microkinetic models based on elementary steps in the attempt to simulate and ultimately predict the industrial ammonia oxidation process over noble metal gauzes.

Ab initio approaches based on quantum chemical principles can complement experimental mechanistic studies, providing valuable information on the structure of the (potential) active centers and the energy of adsorbates interacting with them. In addition, detailed reaction paths can be derived, which arecharacterized by kinetic parameters of the elementary steps involved.[154] Our previous studies using periodical models have assessed the structure, stability, and reactivity of adsorbed NH_x species on the (111) and (100) surfaces of platinum-group metals (Pt, Rh, and Pd) during the nonoxidative dehydrogenation of NH_3.[123, 155] The next step of our work comprises the incorporation of oxygen in the system so as to assess the ammonia oxidation mechanism. Offermans *et al.*[124, 156, 157] investigated the energetics and dynamics of reactants, intermediates, and products of ammonia oxidation over Pt(111) and Pt(211). Kinetic parameters of the (oxidative) dehydrogenation steps were provided, although no emphasis was put on the product distribution. Imbihl *et al.*[152, 153] studied the reaction kinetics over stepped Pt surfaces combining UHV experiments and simulations. Other authors have recently conducted computational studies of NH_3 oxidation over Rh(111)[158] and Au(111).[159] Extending the calculations by Offermans *et al.*[124] to the Pt(100) surface is highly relevant, since platinum exhibits a pronounced structure sensitivity with respect to the adsorption of ammonia and its dehydrogenation,[123, 155] the adsorption of oxygen,[160] and nitric oxide dissociation.[114] Accordingly, the mechanistic picture strongly depends on the surface under consideration, having a strong influence on the performance. In this respect, Vidal-Iglesias *et al.*[127] and Rosca and Koper[128] demonstrated that the electrocatalytic oxidation of ammonia occurs principally on Pt(100), while Pt(111) is comparatively inactive.

The development and optimization of chemical processes requires accurate reaction models that are applicable over a wide range of process conditions. Computer simulation has become invaluable to complement experimental studies for achieving these goals. Microkinetic models constructed from the fundamental kinetics of the elementary reaction steps offer the ability to cover a broad range of process conditions, along with improved accuracy. In recent years, we have seen remarkable progress in the implementation of ab initio density functional theory (DFT), Monte Carlo (MC) simulations, and molecular dynamics (MD) in the development of microkinetic models in heterogeneous catalysis. Prominent examples are ammonia synthesis on Ru(001),[161] methanol synthesis on Cu(100)[162] and decomposition on Pt(111),[163,164] hydrogenation and oxidation of hydrocarbons (Pd(100), Pd(111), and Pt(111)),[165–167] decomposition of nitric oxide on Pt(100) and Rh(100),[134] and oxidation of carbon monoxide on $RuO_2(110)$.[168] Herein we study the mechanism and microkinetics of ammonia oxidation on Pt(100) by DFT. The structure, stability, and reaction pathways of the species involved have been computed and compared to the oxygen-free ammonia dehydrogenation. Classical mechanistic postulates, involving nitroxyl, imide, and hydroxylamine as reaction intermediates, have been evaluated and discriminated. Rate constants of the elementary steps involved in the mechanism have been calculated based on the transition-state theory. Factors governing the formation of NO, N_2, and N_2O, as well as H_2O are discussed. Analogies and differences between our results and those recently reported over Pt(111) and Pt(211) are addressed. A microkinetic model was developed to simulate the product distribution at relevant temperatures and feed O_2/NH_3 ratios.

5.2 Computational details

Calculations were performed in the frame of DFT using the Vienna ab initio simulation program (VASP).[54,57] This program solves the Kohn-Sham equations of the density functional theory with the development of the one-electron wave function in a basis of plane waves. The electron-ion interactions were described by the projector augmented wave (PAW) method.[99] The tight convergence of the planewave expansion was obtained with a cutoff of 400 eV. The generalized gradient approximation (GGA) was used with the functional of Perdew and Wang.[100] We considered the 2×2 unit cell associated with a molecular coverage of 0.25 ML. The 2D Brillouin integrations were performed on a **5×5×1** grid. The correct convergence of the adsorption energy by using this density of k-points was evaluated. Geometries were relaxed using the conjugate gradient algorithm until the forces on all unconstrained atoms were less than 0.01 eV/Å. For adsorbed species, a nonpolarized spin formalism was used since spin polarization effects were found to be negligible.

The Pt(100) surface was modeled by a two-dimensional slab in a three-dimensional periodic cell generated by introducing a vacuum width of ca. 12 Å in the normal direction to the surface. The slabs contained four atomic metal layers with the target molecular and atomic species (NH_3, NH_2, NH, N, O, OH, H_2O, HNO, NOH, NH_2OH, NO, N_2O, and N_2) adsorbed on one side of the slab. We used the optimized metal-metal interatomic distances for the bulk to prevent unlikely forces on the metal atoms. The resulting Pt-Pt distance is 2.82 Å, close to the value determined experimentally (2.77 Å).[129]

The energy of the bare surface was calculated by permitting relaxation of the two top layers. The geometry optimization included all degrees of freedom of the adsorbates and the two uppermost metal layers, while the two lowest metal planes were fixed at the optimized bulk geometry.

The adsorption energy (E_{ads}) for each species was computed as the difference between the energy of the adsorbed molecule ($E_{M-surface}$) and the sum of the energies of the clean surface ($E_{surface}$) and the gas-phase species ($E_{M-gas-phase}$) (eq. 5.1). A negative value of E_{ads} indicates an exothermic chemisorption process.

$$E_{ads} = E_{M-surface} - E_{surface} - E_{M-gas-phase} \tag{5.1}$$

To compare the relative stabilities of the different species, and construct the energy profiles (see, e.g., Figure 5.3) the adsorption energies were recomputed with respect to a common reference: one ammonia molecule in gas phase, three adsorbed oxygen atoms, and three adsorbed hydroxyl species.

The transition states (TS) were determined using the nudged elastic band methods (NEB and CI-NEB) and the dimer method.[70] The TS geometries were refined until a negligible value of the energy gradients was found using the quasi-Newton algorithm implemented in VASP.

A vibrational analysis was carried out in order to validate the optimized geometry of the adsorbed species and to determine transition states. All metal atoms were rigidly constrained during these calculations. The Hessian dynamical matrix was obtained by numerical differentiation of the forces and diagonalized, providing the harmonic molecular frequencies and the normal modes. These calculations made it possible to compute ZPE corrected energies and partition functions.

The rate (r) of the elementary step in the mechanism (R3-R10 in Table 5.4), was determined multiplying the coverage of reactants by the corresponding rate coefficient (k), (eq. 5.2). Rate coefficients were computed according the conventional transition-state theory of Eyring[75] and Evans and Polanyi[76] (eq. 5.3). In this equation, k_0 is the pre-exponential factor, E_a is the ZPE-corrected activation energy, and q_{IS} and q_{TS} are the partition functions of reactants and transition states, respectively, at a given temperature. In reaction steps, the partition functions only consider the vibrational modes. Equation 5.3

was also used for the calculation of desorption rates (R1, R2, and R11-R14, and R23-R26 in Table 5.4). For desorption steps, the partition function q_{IS} considers the vibrational modes, while q_{TS} includes the rotational, vibrational, electronic, and translational modes.[73, 74]

$$r = \theta_R \cdot k \tag{5.2}$$

$$k = k_0 \cdot \exp\left(\frac{-E_a}{k_B T}\right) = \frac{k_B T}{h} \cdot \frac{q_{TS}}{q_{IS}} \cdot \exp\left(\frac{-E_a}{k_B T}\right) \tag{5.3}$$

The rate of adsorption steps (R1, R2, R11-R14, and R23-R26 in Table 5.4) was calculated using the Hertz-Knudsen equation (eq. 5.4), where p_i is the partial pressure of the gas-phase species i, k_B is the Boltzmann's constant, and A_{cat} is the area of one free site. Note that we have not included the sticking coefficient in the model.

$$r_{ads,i} = p_i \cdot (2\pi m_i k_B T)^{-1/2} \cdot A_{cat} \cdot \theta_* \tag{5.4}$$

The mathematical description of the microkinetics derived from the reaction network in Table 5.4 originated a set of ordinary differential equations (ODE). Including the contour conditions for the coverage ($\theta_* = 1 - \theta_{NH_3} - 2\theta_{NH_2} - 2\theta_{NH} - 2\theta_N - 2\theta_O - 2\theta_{OH} - 2\theta_{H_2O} - \theta_{N_2} - 2\theta_{NO} - \theta_{N_2O}$), the system becomes a set of differential algebraic equations (DAE) that is solved numerically using the commercial Maple software (Maplesoft). The results lead to the temporal evolution of each species as a function of temperature and the partial pressures of NH_3 and O_2.

5.3 Results and discussion

Adsorption

The adsorption energy and structural parameters of individual species potentially participating in ammonia oxidation are presented in Table 5.1 and Figure 5.1.The adsorption energy (E_{ads}) was computed using eq. 5.1 (see Computational details) and provides information on the stability of the adsorbed species with respect to the gas phase. Results for NH_x species were discussed previously and will be considered succinctly here.[123, 155] All the NH_x species chemisorb in a N-down orientation. NH_2 preferentially adsorbs on the bridge site with the molecular C_2-axis perpendicular to the surface, being stable also on top position. Both NH and N prefer the hollow site although the bridge site is also a minimum. The difference in adsorption energies between hollow and bridge sites is of 16 kJ·mol^{-1} (this figure is as in the following ZPE corrected) for NH and 9 kJ·mol^{-1} for N. As shown in Figure 5.1, adsorbed NH has the N atom in bridge position while the H atom is tilted toward the hollow site. There is a diffusion barrier of 28 kJ·mol^{-1} for the translation of NH from hollow to bridge. In the case of N, the diffusion barrier from hollow to bridge is of 20 kJ·mol^{-1}. Atomic oxygen adsorbs preferentially on bridge sites, in agreement with previous studies.[169] The other sites, i.e. top and hollow, are maxima of the potential energy surface. The adsorption sites of ammonia and oxygen are different and this suggests that both species do not compete for the same active centre on the platinum surface during NH_3 oxidation. In agreement, Pignet *et al.*[170] showed experimentally that adsorbed oxygen did not block the ammonia adsorption over polycrystalline Pt. The dual-site concept has been used by Rebrov *et al.*[14] for kinetic modeling of ammonia oxidation over a supported polycrystalline platinum catalyst. Both NH_2 and OH species preferentially adsorb on bridge sites. However, the energy difference between the bridge and the top site for OH is much lower than for NH_2 (41 kJ·mol^{-1} versus 87 kJ·mol^{-1}). The geometry of the top configuration is characterized by Pt-OH and O-H distances of 1.92 and 1.00 Å, respectively, and a Pt-O-H angle of 109.6°. In bridge configuration, the Pt-OH and O-H distances are 2.11 Å and $d_{O-H} = 0.98$ Å, respectively, and the dihedral Pt-Pt-O-H angle is 94.7° (see Figure 5.1). H_2O is adsorbed on top (E_{ads}= -23 kJ·mol^{-1}) and exhibits a nearly flat configuration with respect to the surface. The computed adsorption energy is similar to the reported values by Michaelides and Hu[171] (-33 kJ·mol^{-1}) and Offermans *et al.*[124] (-23 kJ · mol^{-1}) on Pt(111).

Hydroxylamine (NH_2OH) and nitroxyl (HNO) have been postulated as reaction intermediates in ammonia oxidation.[21, 22] NH_2OH is adsorbed on top position through the nitrogen atom and with the OH group pointing to the hollow site. The adsorption energy of -116 kJ·mol^{-1}, i.e., considerably more stable than ammonia (-66 kJ·mol^{-1}) or water (-23 kJ·mol^{-1}). The distances N-H, O-H, and N-O in adsorbed state are 1.03, 0.99, and 1.44 Å, respectively. HNO is adsorbed with an E_{ads} = -197 kJ·mol^{-1} on two bridge sites through both the nitrogen and oxygen atoms. The adsorbed compound is not purely perpendicular to the surface; the height of the oxygen atom is 1.41 Å while for the N atom is 1.28 Å. The binding energy of HNO is -393 kJ·mol^{-1} with respect to gas-phase NO + H, similar to the result calculated by Ford *et al.*[98] (-377 kJ·mol^{-1}) on Pt(111).

N-containing products of ammonia oxidation are dinitrogen, nitrous oxide, and nitric oxide. For N_2, two local minima were characterized, one perpendicular to the surface on top of a Pt atom (E_{ads} = -30 kJ·mol^{-1}) and the other

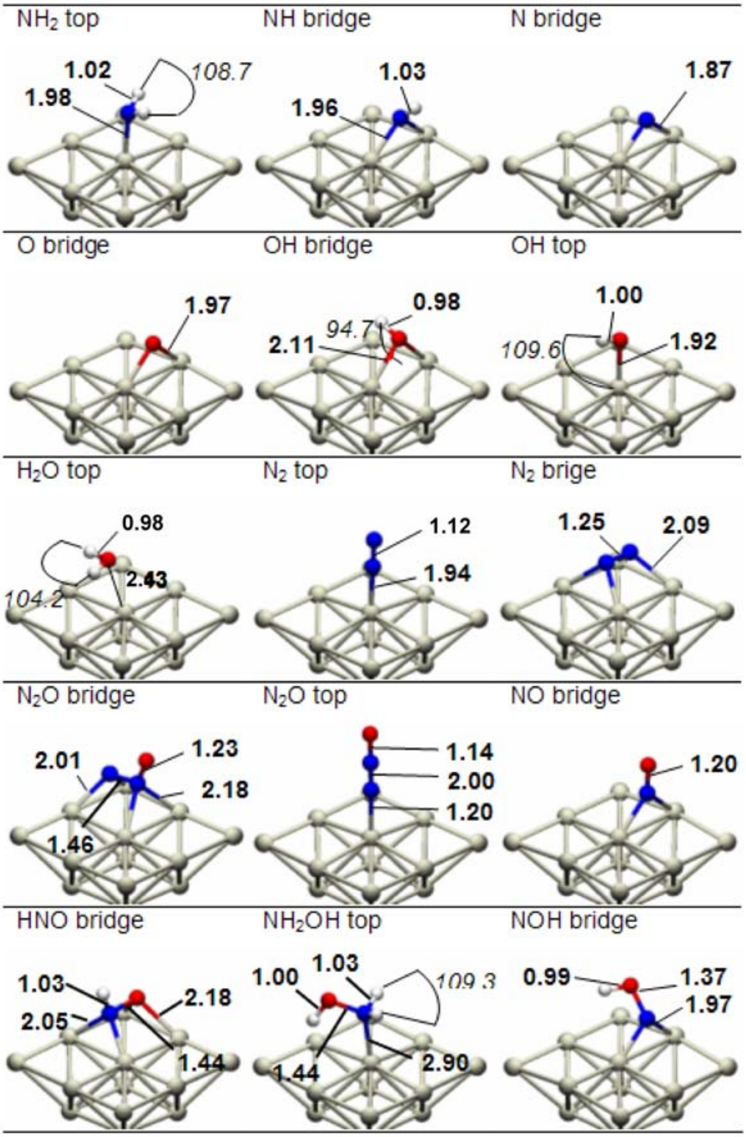

Figure 5.1: Schematic representation of the geometries of selected species adsorbed on Pt(100) at 0.25 ML. Distances (bold numbers) in Angstroms and angles (italic numbers) in degrees.

Table 5.1: Adsorption energies in kJ·mol^{-1} of the different species on Pt(100) at 0.25 ML. The energy was computed with respect to the corresponding species in the gas phase. Values in parenthesis include ZPE correction.

Species		Adsorption sites	
	top	bridge	hollow
NH_3	-76 (-66)	-	-
NH_3	-208 (-202)	-301 (-289)	-
NH	-	-359 (-345)	-378 (-361)
N	-264* (-259)	-421 (-413)	-427 (-422)
O	-298* (-298)	-410 (-403)	-366* (-364)
OH	-250 (-240)	-295 (-281)	-
H_2O	-28 (-23)	-	-
NH_2OH	-122 (-116)	-	-
HNO	-	-215 (-197)	-
NOH	-	-170 (-162)	-
N_2	-35 (-30)	7 (11)	-
NO	-	-217 (-209)	-
N_2O	-16 (-15)	-3 (-6)	-

* Stationary points corresponding to a maximum.

one parallel to the surface with the two N atoms pointing to bridge sites (E_{ads} = 11 kJ·mol^{-1}), see Figure 5.1. These values agree well with calculations by Eichler and Hafner[172] and Neurock *et al.*[134] over Pt(100). The most stable adsorption site for N_2O is on top through the N atom (E_{ads} = -15 kJ·mol^{-1}), in correspondence with values reported by Burch *et al.*[173] over Pt(111). Another minimum for this molecule was found in bridge (E_{ads} = -6 kJ·mol^{-1}), being geometrically very similar to adsorbed HNO. Finally, NO adsorbs perpendicular to the surface on bridge position through the N atom with an adsorption energy of -209 kJ·mol^{-1}, very similar to values obtained theoretically[172,174] and experimentally.[175] The NO adsorption on Pt(100) was slightly more favorable than on Pt(111), where adsorption energies of -180 kJ·mol^{-1}[98] and -203 kJ·mol^{-1}[172] have been reported.

O-assisted dehydrogenation

The nonoxidative ammonia dehydrogenation on both Pt(100) and Pt(111) was previously discussed.[124,155,156] Briefly, the barriers (E_{act}) and reaction energies (ΔE_1) for the successive dehydrogenation steps (ZPE corrected) were: $NH_3 \rightarrow NH_2 + H$ (E_{act} = 97 kJ·mol^{-1}, ΔE_1 = -31 kJ·mol^{-1}), $NH_2 \rightarrow NH + H$ (E_{act} = 107 kJ·mol^{-1}, ΔE_1 = 56 kJ·mol^{-1}), and $NH \rightarrow N + H$ (E_{act} = 82 kJ·mol^{-1}, ΔE_1 37 kJ·mol^{-1}). The barriers and reactions energies on Pt(111) were: $NH_3 \rightarrow NH_2 + H$ (E_{act} = 91 kJ·mol^{-1}, ΔE_1 49 kJ·mol^{-1}), $NH_2 \rightarrow NH + H$ (E_{act} = 101 kJ·mol^{-1}, ΔE_1 -5 kJ·mol^{-1}), and $NH \rightarrow N + H$ (E_{act} = 116 kJ·mol^{-1}, ΔE_1 50 kJ·mol^{-1}). The most noticeable difference between both facets was the high stability of adsorbed NH_2 on Pt(100) compared to Pt(111).[123,156]

Consequently, the abstraction of the first hydrogen atom of ammonia is exothermic on Pt(100) while endothermic on Pt(111). Building on these results, we consider the oxygenassisted ammonia dehydrogenation on Pt(100). Each step is initiated with both NH_x and O coadsorbed in the Pt(2×2) cell, and the reaction leads to NH_{x-1} and OH (Figure 5.2).

The full reaction pathway leading to N is shown in Figure 5.3 (black line). The NH_3+O and NH_2+O coadsorbed systems present a notable stabilization with respect to the noninteracting fragments, 45 and 42 kJ·mol^{-1}, respectively. However, the NH+O coadsorbed system is only stabilized by 3 kJ·mol^{-1} with respect to the noninteracting configuration. Some of the products of the oxidative dehydrogenation steps are stabilized when coadsorbed with respect to the fragments at infinite distance, e.g., 23 kJ·mol^{-1} for NH+OH and 3 kJ·mol^{-1} for N+OH. However, the coadsorbed NH_2 and OH system is destabilized by 7 kJ·mol^{-1} versus the noninteracting state.

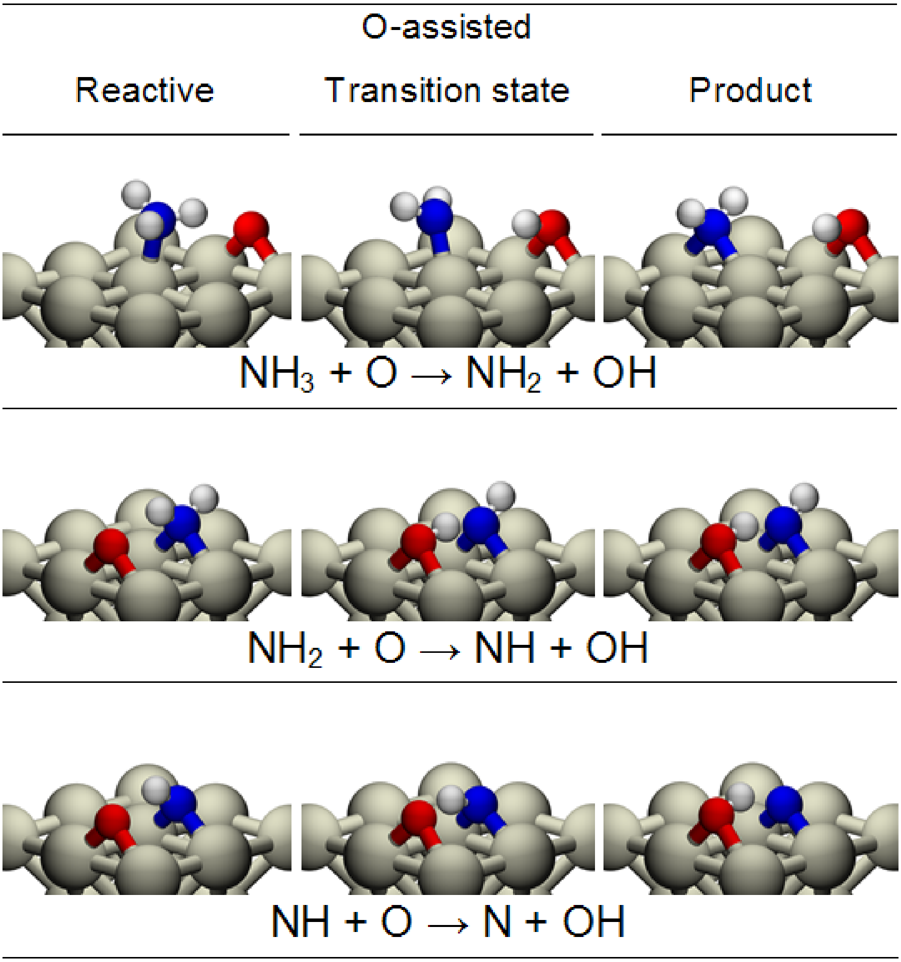

Figure 5.2: Representation of the initial, transition, and final states for the O-assisted ammonia dehydrogenation on Pt(100) at 0.25 ML.

Table 5.2: Coadsorption energy of the reactants, activation energy, reaction energies, and geometries of transition states for the O-assisted and OH-assisted of NH_3 over Pt(100). Energies are in kJ·mol^{-1} and distances in Angstroms. Reactions energies are described with respect to the coadsorbed fragments on the 2×2 cell in the most stable configuration (ΔE_1) and with respect to the sum of the binding energy of the isolated fragments in their most stable adsorption site (ΔE_2).

	O-assisted		
	$NH_3+O \rightarrow NH_2+OH$	$NH_2+O \rightarrow NH+OH$	$NH+O \rightarrow N+OH$
E_{co-ads}	-45	-42	-3
E_{act}	-58	29	0
ΔE_1	-14	29	-11
ΔE_2	-24	52	-8
site N	top	bridge	bridge
site O	bridge	bridge	bridge
d_{Pt-N}	1.99	2.02	1.92
d_{Pt-O}	2.12	2.07	2.02
d_{N-H}	2.59	1.42	1.19
d_{O-H}	0.99	1.12	1.31

Table 5.2 collects the activation energy for each elementary step in Figures 5.2 and 5.3. The calculated barriers were 30-80 kJ·mol^{-1} lower than those in the nonoxidative ammonia dehydrogenation. In the O-assisted ammonia dehydrogenation, the highest barrier corresponds to the first abstraction of hydrogen in the NH_3 molecule (58 kJ·mol^{-1}), thus being the slowest dehydrogenation step.

OH-assisted dehydrogenation

Since OH is a product of the NH_x+O reactions, a pathway with hydroxyl as the oxidative species leading to NH_{x-1} fragments and H_2O could be envisaged (Figure 5.4). This reaction network, referred to as OH-assisted NH_3 dehydrogenation, was computed and results of coadsorption energy, reaction energy, and activation energy are presented in Figure 5.3 (gray line) and Table 5.3. The corresponding initial, transition, and final states are depicted in Figure 5.4. The OH adsorbs on bridge with the exception of the NH_2 + OH step, in which OH adsorbs on top. This is attributed to the limited space available (steric effect) in the 2×2 cell. In fact, calculations us-

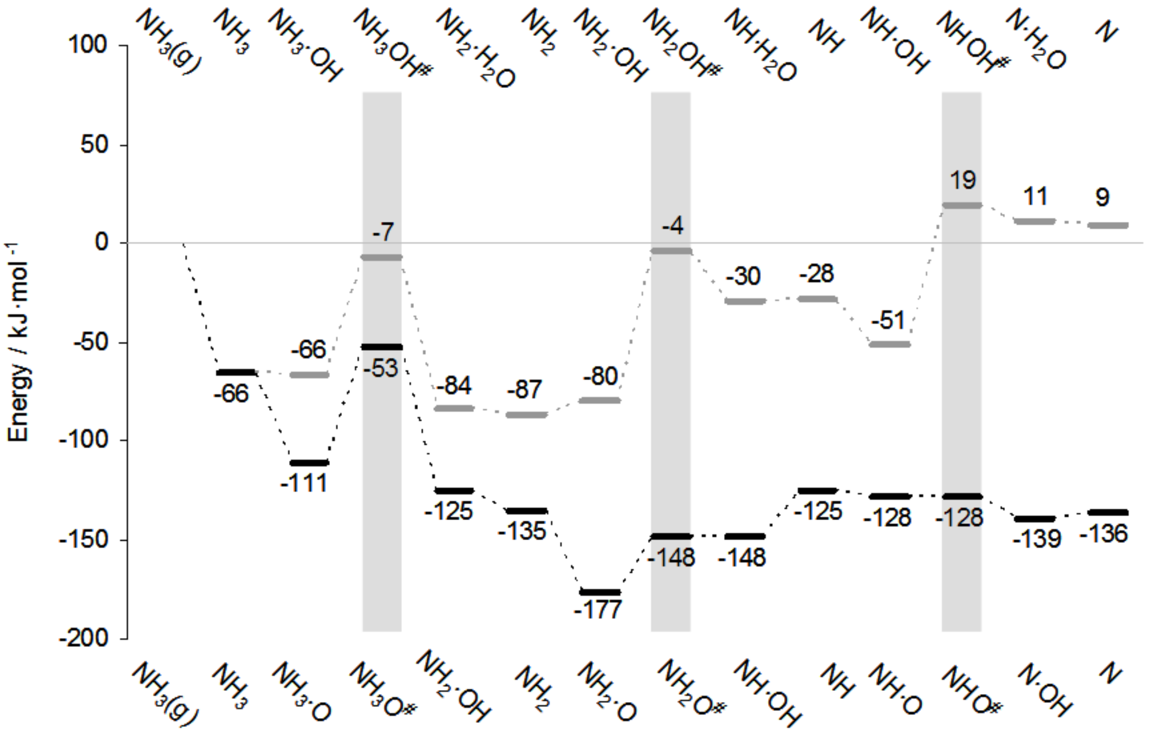

Figure 5.3: Reaction pathway for the oxidative dehydrogenation of ammonia over Pt(100) assisted by O (black line, bottom legend) and OH (grey line, top legend). Reference: $NH_3(g)+3\,O_{ads}+3\,OH_{ads}$, ZPE corrected.

Table 5.3: Coadsorption energy of the reactants, activation energy, reaction energies, and geometries of transition states for the O-assisted and OH-assisted of NH_3 over Pt(100). Energies are in kJ·mol^{-1} and distances in Angstroms. Reactions energies are described with respect to the coadsorbed fragments on the 2×2 cell in the most stable configuration (ΔE_1) and with respect to the sum of the binding energy of the isolated fragments in their most stable adsorption site (ΔE_2).

		OH-assisted	
	$NH_3+OH \rightarrow NH_2+H_2O$	$NH_2+OH \rightarrow NH+H_2O$	$NH+OH \rightarrow N+H_2O$
E_{co-ads}	0	7	-23
E_{act}	59	76	70
ΔE_1	-18	50	62
ΔE_2	-21	52	60
site N	top	bridge	bridge
site O	top	top	top
d_{Pt-N}	2.00	1.96	1.92
d_{Pt-O}	2.78	3.53	2.11
d_{N-H}	2.43	2.98	1.29
d_{O-H}	0.99	0.98	1.22

ing a 3×3 unit cell lead to OH on bridge with an interaction energy of -12 kJ·mol^{-1}. The activation and reactions energies for the successive H-abstraction steps were: NH_3+OH→NH_2+H_2O (E_{act} = 59 kJ·mol^{-1}, ΔE_1 = -18 kJ·mol^{-1}), NH_2+OH→NH+H_2O (E_{act} = 76 kJ·mol^{-1}, ΔE_1 = 50 kJ·mol^{-1}), and NH+OH→N+H_2O (E_{act} = 70 kJ·mol^{-1}, ΔE_1 = 62 kJ·mol^{-1}). The first step corresponds to the lowest activation energy and is exothermic while the following steps are endothermic and present a relatively high barrier. Once the water molecule is formed it desorbs rapidly, although maintaining some attractive interaction with the NH_x fragment except in the case of N+H_2O step, in which water remains coadsorbed with the nitrogen atom. As seen in Figure 5.4 and quantified in Table 5.3, the barriers of the OH-assisted NH_3 dehydrogenation are considerably higher than those of the O-assisted analogue, although the OH-assisted process is certainly more favorable that the nonoxidative NH_3 dehydrogenation. These results contrast with DFT calculations of ammonia oxidation over Pt(111).[124] Over the latter surface, atomic oxygen only activates the dehydrogenation of NH_3, whereas OH activates the dehydrogenation of NH_2 and NH species. This striking difference between Pt(111) and Pt(100) is discussed separately.

Comparison of Pt(100) and Pt(111)

Our previous works have stressed the marked influence of the surface topology on the reaction energies and barriers in ammonia dehydrogenation in the absence of oxygen-containing species. This was concluded from comparison of the (100), (111), and (211) facets over three metals (Pt, Rh, and Pd).[123, 155, 156] The above-noted difference between Pt(100) and Pt(111) regarding the nature of the oxidizing species in ammonia oxidation (O versus OH) can be generally explained attending to the bond order conservation principle,[176] and to the different stability of adsorbed OH on both facets. The sharing effect is induced by the direct interaction of platinum atoms of the surface by two or more adsorbates. As shown by Offermans *et al.*[124] this phenomenon is particularly pronounced in the NH_2+O→NH+OH and NH+O→N+OH steps over Pt(111). Oppositely, Pt(100) does not exhibit sharing effects and the surface reaction of NH_2 or NH with O proceeds with very low barriers. The other difference between Pt(111) and Pt(100) is the stability of OH and NH_2 species on bridge sites. For NH_2, it has been demonstrated that the distortion of the new bonds created by adsorption of the molecule is important over both surfaces.[123]

The same applies to OH. To take into account the new bonds formed upon adsorption of OH species, we hypothesized a H_3O^+ molecule with two H atoms in the same site as the Pt atoms. We have obtained an energy difference of 35

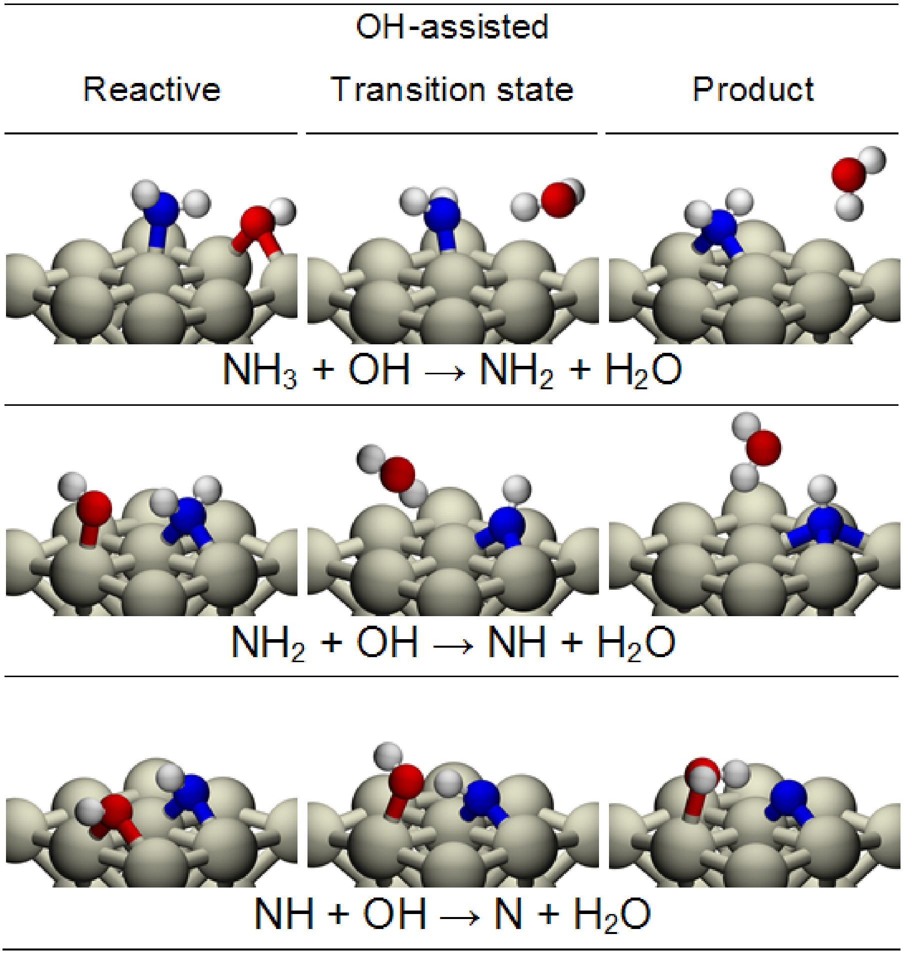

Figure 5.4: Representation of the initial, transition, and final states for the OH-assisted ammonia dehydrogenation on Pt(100) at 0.25 ML.

kJ·mol^{-1} between the structure mimicking the minimum on Pt(100) and the one on Pt(111). The difference in adsorption energy of OH on Pt(100) and Pt(111) was 48 kJ·mol^{-1}. The higher stability of OH on Pt(100) leads to higher barriers in the oxidative dehydrogenation reactions (NH_x+OH→NH_{x-1}+H_2O) on Pt(100). In the same line, the activation energy of H_2O formation (by reaction of adsorbed H and OH) increases from 20 kJ·mol^{-1} on Pt(111) to 81 kJ·mol^{-1} on Pt(100). In conclusion, the ammonia oxidation mechanism is highly sensitive to the particular topology of platinum facet.

Alternative mechanisms

Several theories have been controversially postulated to describe the ammonia oxidation reaction, namely the imide mechanism (NH)[23] considered so far in our calculations, as well as the nitroxyl (HNO)[177] and hydroxylamine (NH_2OH)[22] mechanisms. The latter two mechanisms have been revisited and rationally discarded by means of DFT calculations. The activation energy for nitroxyl formation (NH+O→HNO) is 27 kJ·mol^{-1}, higher than the NH+O→N+OH reaction (0 kJ·mol^{-1}). Thus, the oxidative dehydrogenation reaction is largely favored with respect to HNO formation. In any case, if HNO is formed, its further dehydrogenation by oxygen (HNO+O→NO+OH) is not observed, because the reaction reverts to NH+2O with an activation barrier of 11 kJ·mol^{-1}. We have also considered the intramolecular migration of the H atom in HNO to O leading to NOH, but the barrier for this process is extremely high, 73 kJ·mol^{-1}.

The hydroxylamine mechanism considers as a first step the formation of NH_2OH from NH_3+O or NH_2+OH. Hydroxylamine as reaction intermediate was ruled out by Fogel *et al.*[150] on the basis of secondary ion mass spectrometry studies over Pt. We have computed reaction energies of 129 and 153 kJ·mol^{-1} for the steps NH_3+O→NH_2OH and NH_2+OH→NH_2OH over Pt(100), respectively. The associated activation barriers should be at least equal to the reaction energies, but most likely higher. In any case, these values largely exceed reaction energies of equivalent steps in the imide mechanism, i.e., 58 kJ·mol^{-1} for NH_3+O→NH_2+OH and 76 kJ·mol^{-1} for NH_2+OH→NH+H_2O (Table 5.2). In both cases, the proton transfer from NH_3 or NH_2 species to O or OH is largely favored over the creation of an N-O bond leading to NH_2OH. Therefore, the imide mechanism properly describes the reaction.

Finally, coupling of partially dehydrogenated surface Nspecies in the mechanism have been analyzed. Rosca and Koper[128] have tentatively suggested that dimerization of adsorbed NH_2 into N_2H_4 (surface-bound hydrazine) is rate-determining step in the electrocatalytic oxidation of NH_3 to N_2 over platinum. The reaction NH_2+ $NH_2 \rightarrow N_2H_4$ in bridge sites is unfavorable due to the repulsive lateral interaction of neighboring hydrogen atoms. This repulsion is less relevant if the reaction of the NH_2 species would occur in top sites. However, moving NH_2 from bridge to top demands 107 kJ·mol^{-1} (see Table 5.1). Additionally, the barrier of the coupling $NH+NH \rightarrow N_2H_2$ is significantly higher than that of $NH+O \rightarrow NH+OH$. It should also be noted that the typical O_2/NH_3 ratio of 2 in ammonia burners leads to high surface coverage by oxygen (see Microkinetic Analysis), favoring oxidative dehydrogenation reactions over NH_x coupling. Concluding, the classical postulates (hydroxylamine, nitroxyl) and NH_x dimerization were not considered in the microkinetic model.

Formation of products

As generally known, reaction products of NH_3 oxidation are NO, N_2O, N_2, and H_2O. We have previously seen that the O-assisted dehydrogenation of ammonia ultimately leads to atomic nitrogen and hydroxyl on Pt(100). As illustrated in Figure 5.5, the nitrogen-containing products are formed by reaction of atomic N with another N (N_2), O (NO), or NO (N_2O). N_2 formation has an activation energy of 6 kJ·mol^{-1} and is very exothermic (-179 kJ·mol^{-1}). Analogously, NO formation has an activation energy of 5 kJ·mol^{-1} and a reaction energy of -77 kJ·mol^{-1}, in accordance with Eichler and Hafner.[172] The approach of N and O atoms to form NO is easier than that of two N atoms to form N_2, since the coadsorption energy in the former case (6 kJ·mol^{-1}) is lower that in the latter one (26 kJ·mol^{-1}). Finally, the reaction of N and NO to form N_2O has an activation energy of 49 kJ·mol^{-1}, i.e., higher than those for NO and N_2 formation. Besides, contrarily to N_2 and NO, the production of nitrous oxide is endothermic (50 kJ·mol^{-1}). Therefore, the reverse process, i.e., the decomposition of N_2O in N+NO is exothermic (-50 kJ·mol^{-1}) and has an activation energy of 17 kJ·mol^{-1}. Other possibility is N_2O decomposition into N_2+O. This reaction is exothermic (-152 kJ·mol^{-1}) and has an activation energy of 34 kJ·mol^{-1}. However, since the adsorption energy of N_2O on Pt(100) is very small (-15 kJ·mol^{-1}, see Table 5.1), the desorption of the molecule once formed is more favorable than its decomposition into NO+N or N_2+O. Calculations by Burch *et al.*[173] concluded that N_2O formation at low temperature on Pt(111) occurs by decomposition of a $(NO)_2$ dimer resulting from association of two NO molecules. However, we have not found any stable structure of the $(NO)_2$ dimer on Pt(100). The pathway of water formation is shown in Figure 5.6. Recombination of two hydroxyl fragments leads to H_2O and oxygen, thus regenerating an active Pt-O site. The coadsorption

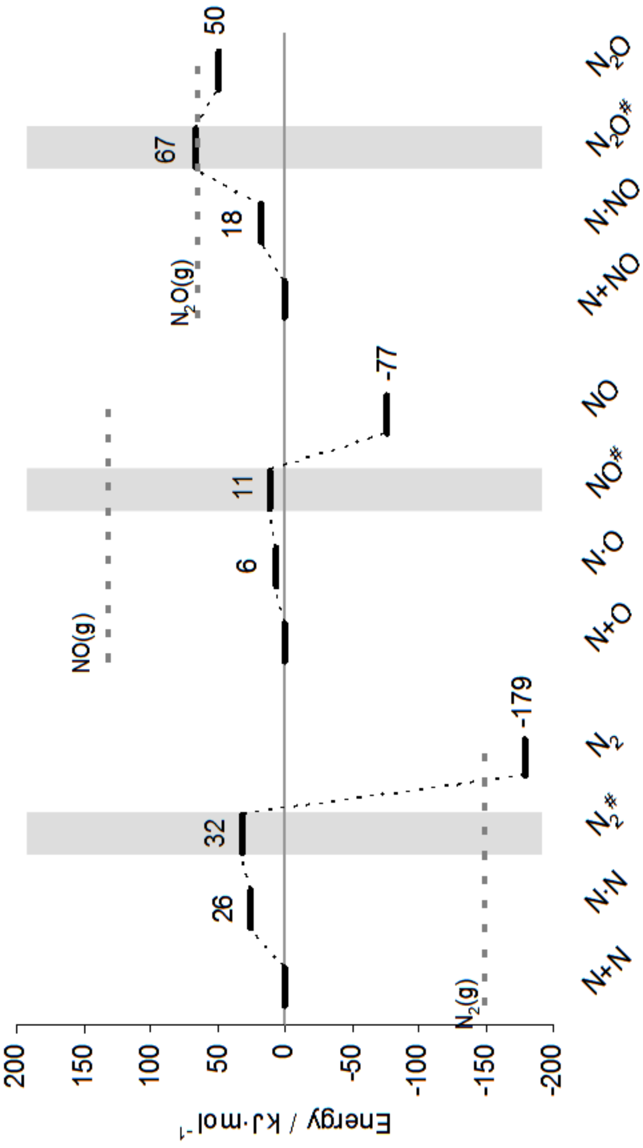

Figure 5.5: Reaction pathways for N_2, NO, and N_2O formation over Pt(100) ZPE corrected.

UNIVERSITAT ROVIRA I VIRGILI
CATALYTIC AMMONIA OXIDATION ON NOBLE METAL SURFACES: A THEORETICAL STUDY
Gerard Novell Leruth
ISBN:978-84-692-1534-0/ DL:T-377-2009

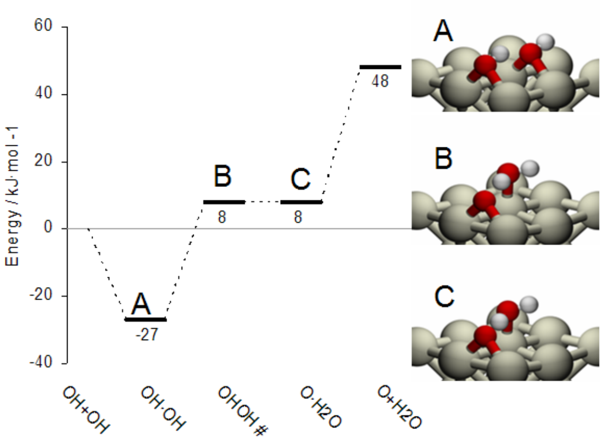

Figure 5.6: Reaction pathway for water formation via OH recombination on Pt(100) ZPE corrected.

energy is -27 kJ·mol^{-1}. The reaction is endothermic (ΔE_1 = 35 kJ·mol^{-1}) and has an activation energy of 35 kJ·mol^{-1}. The formation of water via OH recombination is more favorable than the resulting from OH-assisted NH_x dehydrogenation. This is mainly due to the lower activation energy of the latter route (in the range 59-76 kJ·mol^{-1}, depending on the NH_x fragment).

Besides, the coadsorption energy of two hydroxyls (-27 kJ·mol^{-1}) is more favorable than the coadsorption energy of NH_x+OH (0, 7, and -23 kJ·mol^{-1} for NH_3+OH, NH_2+OH, and NH + OH, respectively). As it can be expected, the reaction parameters and geometries of the OH+OH→H_2O+O and OH+NH→H_2O+N show marked similarities. Over Pt(111), the barrier of water formation via recombination of OH (13 kJ·mol^{-1})[171] is lower than via OH-assisted NH_x dehydrogenation (30-35 kJ·mol^{-1}).[124] Therefore, in this particular facet, water formation may lead to a diminished coverage of active hydroxyl species. Contrarily, water removal on Pt(100) by coupling of OH species generates an active oxygen species.

It should be highlighted that the extremely high adsorption energy of NO on Pt(100) makes NO desorption (step R11 in Table 5.4) as the rate-determining of the overall process (barrier of 209 kJ·mol^{-1}), i.e. more energetically demanding than the barriers of the first H-abstraction of NH_3 by O (58 kJ·mol^{-1}, step R3 in Table 5.3) and certainly much higher than as the desorption barriers of other reaction products (30 kJ·mol^{-1} for N_2, 15 kJ·mol^{-1}

N_2O, and 23 kJ·mol^{-1} for H_2O).

Microkinetic analysis

The ab-initio-derived reaction energies and barriers presented in previous sections were articulated into a microkinetic model in order to simulate the ammonia oxidation process varying parameters such as time, temperature, and oxygen-to-ammonia ratio. As detailed in the computational details section, the rate coefficients were computed using the transition-state theory. Initially, all adsorption, reaction, and desorption steps were included in the model, see Table 5.4. However excluding from the complete reaction network R15 to R26 and the reverse R3, R8, R10, R12, and R14 elementary steps yields a simplified model that gives results within a difference of ∼1%, with respect to the complete model. Thus these steps do not play a role in the overall reaction network and may be disregarded in the model permitting to identify the relevant reactions that explain ammonia oxidation.

For modeling purposes, the activation energy E_a was defined as the difference between the energy level of the transition state and the adsorbed reactants without interaction. The preferred adsorption site of each species and the resulting number of surface platinum atoms occupied were taken into account in order to derive the model (e.g., atomic oxygen adsorbs on bridge, thus requiring two platinum atoms, whereas ammonia adsorbs on top, thus occupying only one platinum atom). Exceptionally, we assumed that water occupies two Pt atoms despite adsorbing on top. This is due to its steric hindrance (see Figure 5.6), requiring a free neighboring Pt atom (a bridge site is equivalent to two platinum atoms). Our model is derived from DFT calculations at a fixed coverage 0.25 ML (see Computational Details).

Figure 5.7 presents the simulated profiles of ammonia conversion and selectivity to N-containing products on Pt(100) as a function of temperature and time using a feed O_2/NH_3 ratio of 2. For clarity, the profiles at $t = 0.7$ s, including the coverage of selected species are shown in Figure 5.8. The inlet partial NH_3 and O_2 pressures in the calculation were 0.1 and 0.2 bar, respectively. The selectivity to nitrogen-containing products shows a marked dependence on temperature and time. In agreement with the literature,[14, 15, 86, 152] N_2 is the main product at low temperature (<550 K), N_2O at intermediate temperature (550-850 K), and NO at high temperature (>850 K). In the low-temperature regime (<400 K), we observe the reaction of adsorbed ammonia and oxygen at 200-300 K, leading to adsorbed NO (R3-R7). This is clear attending to the drop in the oxygen coverage and the concomitant increase in the nitric oxide coverage. NO adsorption is highly favorable and inhibits oxygen adsorp-

Table 5.4: Full and simplified reaction network of NH_3 oxidation on Pt(100) derived from DFT calculations. (b) and (t) indicate bridge and top surface sites, respectively. Note that two adjacent (t) sites are equivalent to a (b) site.

Full model		Simplified model
$O_2+2(b) \rightleftharpoons 2\ O(b)$	R1	$O_2+2(b) \rightleftharpoons 2\ O(b)$
$NH_3+(t) \rightleftharpoons NH_3(t)$	R2	$NH_3+(t) \rightleftharpoons NH_3(t)$
$NH_3(t)+O(b)+(t) \rightleftharpoons NH_2(b)+OH(b)$	R3	$NH_3(t)+O(b)+(t) \rightarrow NH_2(b)+OH(b)$
$NH_2(b)+O(b) \rightleftharpoons NH(b)+OH(b)$	R4	$NH_2(b)+O(b) \rightleftharpoons NH(b)+OH(b)$
$NH(b)+O(b) \rightleftharpoons N(b)+OH(b)$	R5	$NH(b)+O(b) \rightleftharpoons N(b)+OH(b)$
$2\ OH(b) \rightleftharpoons O(b)+H_2O(b)$	R6	$2\ OH(b) \rightleftharpoons O(b)+H_2O(b)$
$N(b)+O(b) \rightleftharpoons NO(b)+(b)$	R7	$N(b)+O(b) \rightleftharpoons NO(b)+(b)$
$2\ N(b) \rightleftharpoons N_2(t)+3\ (t)$	R8	$2\ N(b) \rightarrow N_2(t)+3\ (t)$
$N(b)+NO(b) \rightleftharpoons N_2O(t)+3\ (t)$	R9	$N(b)+NO(b) \rightleftharpoons N_2O(t)+3\ (t)$
$N_2O(t)+(b) \rightleftharpoons N_2(t)+O(b)$	R10	$N_2O(t)+(b) \rightarrow N_2(t)+O(b)$
$NO(b) \rightleftharpoons NO+(b)$	R11	$NO(b) \rightleftharpoons NO+(b)$
$N_2(t) \rightleftharpoons N_2+(t)$	R12	$N_2(t) \rightarrow N_2+(t)$
$N_2O(t) \rightleftharpoons N_2O+(t)$	R13	$N_2O(t) \rightleftharpoons N_2O+(t)$
$H_2O(b) \rightleftharpoons H_2O+(b)$	R14	$H_2O(b) \rightarrow H_2O+(b)$
$NH_3(t)+OH(b)+(t) \rightleftharpoons NH_2(b)+H_2O(b)$	R15	
$NH_2(b)+OH(b) \rightleftharpoons NH(b)+H_2O(b)$	R16	
$NH(b)+OH(b) \rightleftharpoons N(b)+H_2O(b)$	R17	
$O(b)+H(b) \rightleftharpoons OH(b)+(b)$	R18	
$OH(b)+H(b) \rightleftharpoons H_2O(b)+(b)$	R19	
$NH_3(t)+3\ (t) \rightleftharpoons NH_2(b)+H(b)$	R20	
$NH_2(b)+(b) \rightleftharpoons NH(b)+H(b)$	R21	
$NH(b)+(b) \rightleftharpoons N(b)+H(b)$	R22	
$2\ H(b) \rightleftharpoons H_2+2\ (b)$	R23	
$NH_2(b) \rightleftharpoons NH_2+(b)$	R24	
$NH(b) \rightleftharpoons NH+(b)$	R25	
$OH(b) \rightleftharpoons OH+(b)$	R26	

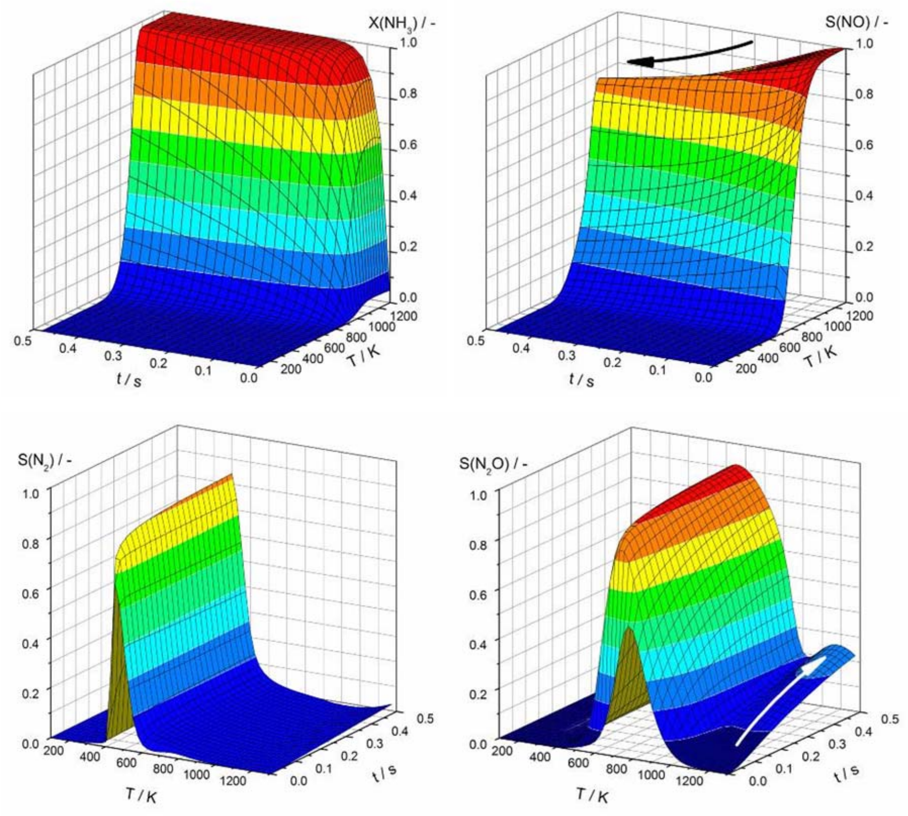

Figure 5.7: Simulated profiles of NH_3 conversion and products selectivity (NO, N_2O, N_2), and coverage of selected species (O and NO) over Pt(100) as a function of temperature and time in a mixture $O_2/NH_3 = 2$.

tion, as free bridge Pt sites are not available. The selectivity to gas-phase N_2 starts at 400 K and reaches a maximum at 500 K. In this temperature regime, the NO coverage also increases as the reaction proceeds on the surface practically without evolution of gas-phase products. Gas-phase NO is not produced in this temperature region due to the high desorption barrier (R11, 217 kJ·mol^{-1}). Significant ammonia conversion is observed above 600 K, in reasonable agreement with experimental results over platinum catalysts.[14, 153] N_2O formation starts at the maximum NO coverage at 500 K and is coupled with the progressive decrease in N_2 selectivity. Accordingly, in this temperature region, the reaction of N and NO to N_2O (R9 in Table 5.4) takes over the coupling of nitrogen atoms to N_2 (R8 in Table 5.4). The maximum of N_2O production is seen at 650 K and above this temperature, gas-phase NO evolves. Thus, the NO coverage progressively decreases, leading to lower N_2 production, and the O coverage increases since free platinum sites become available for gas-phase O_2 dissociation. Our model predicts well changes in product distribution with temperature. In addition, time has a remarkable influence on the selectivity, particularly in the high-temperature region. Increasing the reaction time above 1000 K leading to a lower selectivity of the main product NO at the expense of N_2O (see arrows in Figure 5.7). The S(NO) decreases from 100% at short reaction times to less than 80% at 0.4 s. This is due to the readsorption of nitric oxide, activating the pathway of N_2 formation (R9 in Table 5.4). This prediction is totally in line with the industrial operation of ammonia burners. This reaction operates at 1173 K in the millisecond regime ($\tau = 10^{-3}$ s) in order to minimize loss reactions of NO into N_2O and N_2.[3, 15, 17] Further validation of our model was accomplished by conducting simulations at different feed O_2/NH_3 ratios at 1173 K (Figure 5.9). It is well-known that the NO selectivity increases with the inlet O_2/NH_3 ratio.[178] In good correspondence, both the NH_3 conversion and the NO selectivity markedly increase with the oxygento to ammonia ratio. As anticipated, this correlates well with the higher oxygen coverage on the platinum surface. It should be noted that incorporation of coverage effects and lateral interactions would make it more accurate, but this is beyond the scope of the present work. Qualitatively, we believe that the influence of the coverage will not change the trends derived from the model.

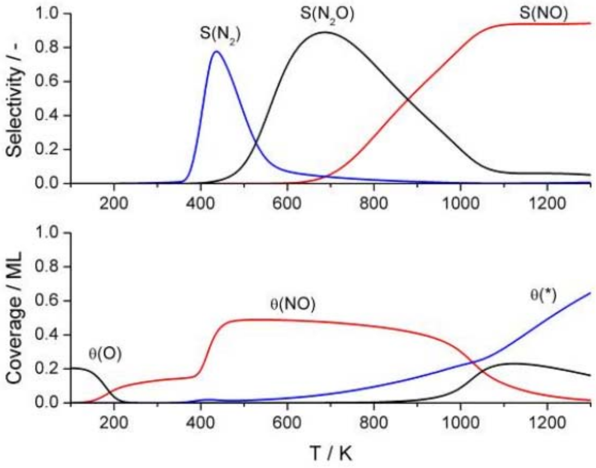

Figure 5.8: Simulated profiles of products selectivity (NO, N_2O, N_2) and coverage of O, NO, and free sites (*) over Pt(100) as a function of temperature at t = 0.1 s and $O_2/NH_3 = 2$.

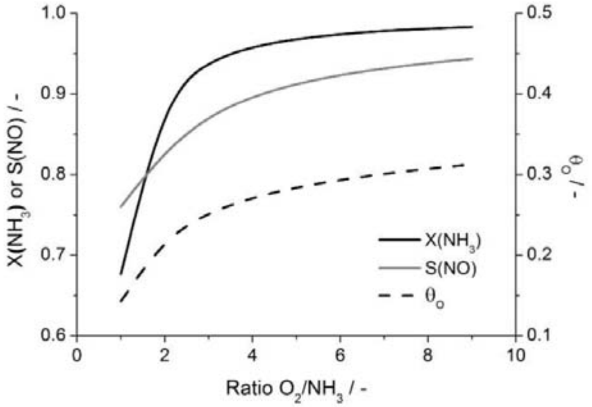

Figure 5.9: Simulated ammonia conversion, selectivity to nitric oxide, and oxygen coverage over Pt(100) at different the feed oxygen-to-ammonia ratios. Simulations were performed at 1173 K and a total pressure 1 bar, fixing the inlet partial NH_3 pressure at 0.1 bar.

5.4 Conclusions

The mechanism of ammonia oxidation over Pt(100) has been investigated to a great level of detail by density functional theory. The reaction proceeds via an imide mechanism, by which ammonia is successively dehydrogenated by atomic oxygen species. Comparatively, other mechanisms postulating nitroxyl and hydroxylamine as reaction intermediates are thermodynamically not favorable. The oxidative abstraction of the first proton of ammonia is the slowest dehydrogenation step. Interestingly, the nature of the preferred oxidizing species for NH_x dehydrogenation (O in Pt(100) and OH in Pt(111)) is determined by the platinum topology, due to sharing effects and the distinct stability of adsorbed NH_2 and OH. The formation of N_2, NO, and N_2O occurs by reaction of N+N, N+O, and N+NO, respectively, while water is formed by OH recombination, regenerating an active O. Both N_2 and NO formation have low barriers and are exothermic, whereas N_2O formation is endothermic and consequently has a higher barrier. Once formed, the barrier of NO desorption is extremely high, becoming the rate-determining step of the overall process. A simplified reaction mechanism has been derived and the rate coefficients of the elementary steps have been computed, enabling a microkinetic analysis of the reaction. Our model predicts well the product distribution obtained experimentally at different temperature, time, and O_2/NH_3 ratio.

Chapter 6

Concluding remarks

Using periodic slab DFT calculations, we have successfully computed the geometry, site preference, and relative stability of adsorbed ammonia and its dehydrogenated fragments (NH_2, NH, N) on the (100) and (111) surfaces of platinum, rhodium, and palladium. The adsorption energy of NH_x species are large on the more open (100) plane than on the (111) one for all metals. Moreover, the adsorption energies are stronger on rhodium than on palladium or platinum. On the six metal surfaces, NH_3 adsorbs on top sites, NH_2 on bridge, and NH and N on hollow sites. The N-H and M-N distances are similar for all species. The differences between the three metals are more significant on the (100) than on the (111) face. The transition states and reaction barriers for the successive dehydrogenation steps have been also determined. All barriers range between 67 $kJ{\cdot}mol^{-1}$ ($NH_3 \rightarrow NH_2+H$ on Rh(100)) and 118 $kJ{\cdot}mol^{-1}$ ($NH \rightarrow N+H$ on Pd(100)). As a general trend, the barriers are higher for the last dehydrogenation step (except for Pt(100)). However, once the kinetic constants are computed, the rate-determining step corresponds to the first hydrogen abstraction (except for Rh(100)) due to the negative activation entropy of this step. On Pd(111) and Pt(111), all transition states are above the energy of NH_3 in the gas phase, while on Rh(111) all species are more stable than adsorbed ammonia. On the (100) surfaces, the energy of the different adsorbed intermediates and transition states is higher on Pt and Pd than on Rh. It is also observed that in the case of Rh, all transition states are below the energy of gas-phase NH_3. Thus, according to our calculations, Rh should be a more active catalyst for NH_3 decomposition than Pt or Pd, in agreement with experimental results reported in the literature.

The mechanism of ammonia oxidation over Pt(100) has been also investigated at a high level of detail. The reaction proceeds via an imide mechanism, which ammonia is successively dehydrogenated by atomic oxygen species. Comparatively, other mechanisms postulating nitroxyl and hydroxylamine as reaction intermediates are energetically not favorable. The oxidative abstraction of the first proton of ammonia is the slowest dehydrogenation step. Interestingly, the nature of the preferred oxidizing species for NH_x dehydrogenation (O in Pt(100) and OH in Pt(111)) is determined by the platinum topology, due to sharing effects and the distinct stability of NH_2 and OH. The formation of N_2, NO, and N_2O occurs by the reactions of N+N, N+O, and N+NO, respectively, while water is formed by OH recombination, regenerating an active O. The formation of N_2 and NO has low barriers and there are exothermic, while N_2O formation is endothermic and consequently has a higher barrier. Once formed, the barrier of NO desorption is extremely high, becoming the rate-determining step of the overall process. A simplified reaction mechanism has been derived and the rate coefficients of the elementary steps have been computed, enabling a microkinetic analysis of the reaction. Our model predicts well the product distribution obtained experimentally at different temperature, time, and O_2/NH_3 ratio.

From the results in this thesis, it is clear that the microkinetic model is the first step to link theoretical and experimental work, although it is necessary to simulate the reaction to do an effective comparison between the theoretical results and experimental data or vice versa. We can also affirm that the theoretical works are a necessary tool to understand the reactions at the molecular level, being a complementary tool of the experimental work, because they contribute to understand the mechanisms of reaction with extra information that is not directly obtained from experimental data..

This thesis has brought a new point of view to undestand the ammonia oxidation reaction. We have not solved all questions so some points still remain opened, but we stablish the basis for future works. This work has a continuation with the study of rhodium and alloys (Pt/Rh) because the industrial catalyst has this composition. The study of alloys can be complicated because the number of arrangements is huge. One method to reduce the computational cost is simplifying the model substituting some atoms of the platinum surface by rhodium. Therefore, it is necessary to study the effect of rhodium in the bulk and in the surface at different concentrations and depths. Other considerations that are necessary to take into account are the segregation effect of Pt/Rh and the mechanism to remove platinum from the surface during the process. Another point to study is the extrapolation of the microkinetic model, presented in this thesis, to the reactor model. A model of Computational Fluid Dynamics (CFD) can be a useful tool to understand the effects of the reactor design in the process. This way opens a large path, like the comparison of experimental data, to improve the design of the reactor, etc. However it can be useful to understand the experimental results or to reaffirm the theoretical data. Although the data are obtained within a defined surface model, far from the reality, they can clarify the knowledge at a molecular level of the experimential observations. To approach the model to the reality we can do a combination of the models. Carrying a study on different models (different metals (Pt, Rh, Pt/Rh), faces, and defects) they can be combined in a suitable proportion. This proportion could be obtained by a sensibility analysis with experimental data, knowing which model has an important weight in the process and which reactions are important. In the future it is a possible technique to obtain a suitable model to do the computational study.

References

[1] Sinfelt, J. H. *Surf. Sci.* **2002**, *500*, 923–946.

[2] Kuhlmann, C. *French patent* **1838**, *11331.*

[3] Farrauto, R. J.; Bartholomew, C. H. *Fundamentals of industrial catalytic processes;* Chapman & Hall: London, 1997.

[4] Hannevold, L.; Nilsen, O.; Kjekshus, A.; Fjellvag, H. *Appl. Catal., A* **2005**, *284*, 177.

[5] Handforth, S. L.; Tilley, J. N. *Ind. Eng. Chem.* **1934**, *26*, 1287.

[6] Zemlyanov, D. Y.; Smirnov, M. Y.; Gorodetskii, V. V. *Surf. Sci.* **1997**, *391*, 37.

[7] Sun, Y. M.; Sloan, D.; Ihm, H.; White, J. M. *J. Vac. Sci. Technol., A* **1996**, *14*, 1516.

[8] Bater, C.; Campbell, J. H.; Craig, J. H. *Surf. Interface Anal.* **1998**, *26*, 97.

[9] Yamada, T.; Tanaka, K. *J. Am. Chem. Soc.* **1989**, *111*, 6880.

[10] Tanaka, K.; Yamada, T.; Nieuwenhuys, B. E. *Surf. Sci.* **1991**, *242*, 503.

[11] Yamada, T.; Hirano, H.; Tanaka, K.; Siera, J.; Nieuwenhuys, B. E. *Surf. Sci.* **1990**, *226*, 1.

[12] Yamada, T.; Tanaka, K. *J. Am. Chem. Soc.* **1991**, *113*, 1173.

[13] Herceg, E.; Mudiyanselage, K.; Trenary, M. *J. Phys. Chem. B* **2005**, *109*, 2828.

[14] Rebrov, E. V.; de Croon, M. H. J. M.; Schouten, J. C. *Chem. Eng. J.* **2002**, *90*, 61.

[15] Pérez-Ramírez, J.; Kapteijn, F.; Schöffel, K.; Moulijn, J. A. *Appl. Catal., B* **2003**, *44*, 117.

[16] Pérez-Ramírez, J.; Kondratenko, E. V.; Kondratenko, V. A.; Baerns, M. *J. Catal.* **2004**, *227*, 90.

[17] Pérez-Ramírez, J.; Kondratenko, E. V. *Chem. Commun.* **2004**, page 376.

[18] Pérez-Ramírez, J.; Kondratenko, E. V.; Kondratenko, V. A.; Baerns, M. *J. Catal.* **2005**, *229*, 303.

[19] Pérez-Ramírez, J.; Kondratenko, E. V. *Catal. Today* **2007**, *121*, 160 – 169.

[20] Zaera, F. *Surf. Sci.* **2002**, *500*, 947.

[21] Andrussow, L. *Z. Angew. Chem.* **1926**, *39*, 321.

[22] Bodenstein, M. *Z. Elektrochem. Angew. Phys. Chem.* **1935**, *41*, 466.

[23] Raschig, F. *Z. Angew. Chem.* **1927**, *40*, 1183.

[24] Zawadzki, J. *Discuss. Faraday Soc.* **1950**, page 140.

[25] Born, M.; Oppenheimer, R. *Ann. Phys.* **1927**, *84*, 0457.

[26] W.J. Hehre, L. Radom, P. S. J. A. P.; John Wiley: New York, 1986.

[27] Baerends, E. J.; Gritsenko, O. V. *J. Phys. Chem. A* **1997**, *101*, 5383.

[28] Thomas, L. H. *Math. Proc. Cambridge Philos. Soc.* **1927**, *23*, 713.

[29] Fermi, E. *Rend. Accad. Lincei.* **1927**, *6*, 602.

[30] Hohenberg, P. *Phys. Rev. B* **1964**, *136*, B864.

[31] Kohn, W.; Sham, L. J. *Phys.Rev.* **1965**, *140*, 1133.

[32] Vosko, S. H.; Wilk, L.; Nusair, M. *Can. J. Phys.* **1980**, *58*, 1200.

[33] Becke, A. D. *J. Chem. Phys.* **1986**, *84*, 4524.

[34] Becke, A. D. *Phys. Rev. A* **1988**, *38*, 3098.

[35] Lee, C. T.; Yang, W. T.; Parr, R. G. *Phys. Rev. B* **1988**, *37*, 785.

[36] Perdew, J. P. *Phys. Rev. B* **1986**, *34*, 7406.

[37] Perdew, J. P.; Yue, W. *Phys. Rev. B* **1986**, *33*, 8800.

[38] Perdew, J. P. *Phys. Rev. B* **1986**, *33*, 8822.

[39] Perdew, J. P.; Burke, K.; Ernzerhof, M. *Phys. Rev. Lett.* **1996**, *77*, 3865.

[40] Becke, A. D. *J. Chem. Phys.* **1993**, *98*, 5648.

[41] Sun, G. Y.; Kurti, J.; Rajczy, P.; Kertesz, M.; Hafner, J.; Kresse, G. *THEOCHEM* **2003**, *624*, 37.

[42] Illas, F.; Ricart, J. M. In *Química teórica y computacional;* 2001.

[43] Sauer, J. *Chem. Rev.* **1989**, *89*, 199.

[44] Ashcroft, N. W.; Mermin, N. D.; Holt: New York, 1976.

[45] Curulla, D.; Clotet, A.; Ricart, J. M.; Illas, F. *J. Phys. Chem. B* **1999**, *103*, 5246.

[46] Curulla, D.; Linke, R.; Clotet, A.; Ricart, J. M.; Niemantsverdriet, J. W. *Phys. Chem. Chem. Phys.* **2002**, *4*, 5372.

[47] Gil, A.; Clotet, A.; Ricart, J. M.; Kresse, G.; Garcia-Hernandez, M.; Rosch, N.; Sautet, P. *Surf. Sci.* **2003**, *530*, 71.

[48] Monkhorst, H. J.; Pack, J. D. *Phys. Rev. B* **1976**, *13*, 5188.

[49] Cunningham, S. L. *Phys. Rev. B* **1974**, *10*, 4988.

[50] Chadi, D. J.; Cohen, M. L. *Phys. Rev. B* **1973**, *8*, 5747.

[51] Hamann, D. R.; Schluter, M.; Chiang, C. *Phys. Rev. Lett.* **1979**, *43*, 1494.

[52] Vanderbilt, D. *Phys. Rev. B* **1990**, *41*, 7892.

[53] Blöchl, P. E. *Phys. Rev. B* **1994**, *50*, 17953.

[54] Kresse, G.; Hafner, J. *Phys. Rev. B: Condens. Matter Mater. Phys.* **1993**, *47*, 558.

[55] Kresse, G.; Hafner, J. *Phys. Rev. B: Condens. Matter Mater. Phys.* **1993**, *48*, 13115.

[56] Kresse, G.; Hafner, J. *Phys. Rev. B: Condens. Matter Mater. Phys.* **1994**, *49*, 14251.

[57] Kresse, G.; Furthmüller, J. *Phys. Rev. B: Condens. Matter* **1996**, *54*, 11169.

[58] Kresse, G.; Furthmüller, J. *Comput. Mater. Sci.* **1996**, *6*, 15.

[59] Johnson, D. D. *Phys. Rev. B* **1988**, *38*, 12807.

[60] Pulay, P. *Chem. Phys. Lett.* **1980**, *73*, 393.

[61] Methfessel, M.; Paxton, A. T. *Phys. Rev. B* **1989**, *40*, 3616.

[62] Hollins, P.; Pritchard, J. *Prog. Surf. Sci.* **1985**, *19*, 275.

[63] Ryczkowski, J. *Catal. Today* **2001**, *68*, 263.

[64] Sheppard, N. *Annu. Rev. Phys. Chem.* **1988**, *39*, 589.

[65] Imelik, B., Védrine, J. C., Eds. *Catalyst Characterization, Physical Techniques for Solid Materials;* Plenum Press: New York, 1994.

[66] Vickerman, J. C.; John Wiley: Chichester England ; New York, 1997.

[67] Niemantsverdriet, J. W.; VCH: Weinheim ; New York, 1993.

[68] McCash, E. M.; Oxford University Press: Oxford, 2001.

[69] Komornicki, A.; McIver, J. W. *J. Am. Chem. Soc.* **1976**, *98*, 4553.

[70] Henkelman, G.; Jonsson, H. *J. Chem. Phys.* **1999**, *111*, 7010.

[71] Henkelman, G.; Uberuaga, B. P.; Jonsson, H. *J. Chem. Phys.* **2000**, *113*, 9901.

[72] Jónsson, H.; Mills, G.; Jacobsen, K. W. In *Classical and Quantum Dynamics in Condensed Phase Simulations;* World Scientific, 1998; page 385.

[73] Masel, R. I.; Wiley-Interscience: New York, 2001.

[74] Laidler, K. J. *Chemical kinetics;* New York, 1987.

[75] Eyring, H. *J. Chem. Phys.* **1935**, *3*, 107.

[76] Evans, M. G.; Polanyi, M. *Trans. Faraday Soc.* **1935**, *31*, 875.

[77] Atkins, P. W. *Physical chemistry;* University Press: Oxford, 6th ed., 1998.

[78] Levine, I. N. *Quantum chemistry;* Prentice Hall: New Jersey, 5th ed., 2000.

[79] Chorkendorff, I.; Niemantsverdriet, J. W. *Concepts of modern catalysis and kinetics;* Wiley-VCH: Weinheim, 2003.

[80] Callaghan, C. A.; Fishtik, I.; Datta, R.; Carpenter, M.; Chmielewski, M.; Lugo, A. *Surf. Sci.* **2003**, *21*, 541.

[81] Gland, J. L.; Korchak, V. N. *J. Catal.* **1978**, *53*, 9.

[82] Gland, J. L.; Woodard, G. C.; Korchak, V. N. *J. Catal.* **1980**, *61*, 543.

[83] Sexton, B. A.; Mitchell, G. E. *Surf. Sci.* **1980**, *99*, 523.

[84] Asscher, M.; Guthrie, W. L.; Lin, T. H.; Somorjai, G. A. *J. Phys. Chem.* **1984**, *88*, 3233.

[85] Mieher, W. D.; Ho, W. *Surf. Sci.* **1995**, *322*, 151.

[86] Bradley, J. M.; Hopkinson, A.; King, D. A. *J. Phys. Chem.* **1995**, *99*, 17032.

[87] Bradley, J. M.; Hopkinson, A.; King, D. A. *Surf. Sci.* **1997**, *371*, 255.

[88] Kim, M.; Pratt, S. J.; King, D. A. *J. Am. Chem. Soc.* **2000**, *122*, 2409.

[89] Zemlyanov, D. Y.; Smirnov, M. Y.; Gorodetskii, V. V.; Block, J. H. *Surf. Sci.* **1995**, *329*, 61.

[90] Logadóttir, A.; Nørskov, J. K. *J. Catal.* **2003**, *220*, 273.

[91] Zhang, C. J.; Lynch, M.; Hu, P. *Surf. Sci.* **2002**, *496*, 221.

[92] Fahmi, A.; van Santen, R. A. *Z. Phys. Chem.* **1996**, *197*, 203.

[93] García-Hernández, M.; López, N.; Moreira, I. D.; Paniagua, J. C.; Illas, F. *Surf. Sci.* **1999**, *430*, 18.

[94] Jennison, D. R.; Schultz, P. A.; Sears, M. P. *Surf. Sci.* **1996**, *368*, 253.

[95] Cholach, A. R.; Bulgakov, N. N. *Catal. Lett.* **1999**, *58*, 183.

[96] Michaelides, A.; Hu, P. *J. Am. Chem. Soc.* **2000**, *122*, 9866.

[97] Baerns, M.; Imbihl, R.; Kondratenko, V. A.; Kraehnert, R.; Offermans, W. K.; van Santen, R. A.; Scheibe, A. *J. Catal.* **2005**, *232*, 226.

[98] Ford, D. C.; Xu, Y.; Mavrikakis, M. *Surf. Sci.* **2005**, *587*, 159.

[99] Kresse, G.; Joubert, D. *Phys. Rev. B* **1999**, *59*, 1758.

[100] Perdew, J. P.; Wang, Y. *Phys. Rev. B* **1992**, *45*, 13244.

[101] Gerber, R. B.; Brauer, B.; Gregurick, S. K.; Chaban, G. M. *Phys. Chem. Commun.* **2002**, *5*, 142.

[102] Irian program; universistat rovira i virgili: Tarragona. Clotet, A. **2003**.

[103] Fierro, C. *J. Phys. Chem.* **1988**, *92*, 4401.

[104] Chattopadhyay, A.; Yang, H.; Whitten, J. L. *J. Phys. Chem.* **1990**, *94*, 6379.

[105] Neurock, M.; van Santen, R. A.; Biemolt, W.; Jansen, A. P. J. *J. Am. Chem. Soc.* **1994**, *116*, 6860.

[106] Zurita, S.; Rubio, J.; Illas, F. *Electrochim. Acta* **1996**, *41*, 2275.

[107] Fisher, G. B. *Chem. Phys. Lett.* **1981**, *79*, 452.

[108] Szulczewski, G.; Levis, R. J. *J. Chem. Phys.* **1995**, *103*, 10238.

[109] Reuter, K.; Scheffler, M. *Phys. Rev. B* **2002**, *65*.

[110] Bollinger, M. V.; Jacobsen, K. W.; Nørskov, J. K. *Phys. Rev. B* **2003**, *67*, 085410.

[111] Cristol, S.; Paul, J. F.; Payen, E.; Bougeard, D.; Clémendot, S.; Hutschka, F. *J. Phys. Chem. B* **2000**, *104*, 11220.

[112] Raybaud, P.; Hafner, J.; Kresse, G.; Kasztelan, S.; Toulhoat, H. *J. Catal.* **2000**, *189*, 129.

[113] Loffreda, D.; Delbecq, F.; Sautet, P. *Chem. Phys. Lett.* **2005**, *405*, 434.

[114] Gohndrone, J. M.; Masel, R. I. *Surf. Sci.* **1989**, *209*, 44.

[115] Bassignana, I. C.; Wagemann, K.; Küeppers, J.; Ertl, G. *Surf. Sci.* **1986**, *175*, 22.

[116] Jennings, J. R. *Catalytic Ammonia Synthesis: Fundamentals and Practice;* New York, 1991.

[117] *Ullmann's Encyclopedia of Industrial Chemistry;* Wiley-VCH Verlag GMBH: Weinheim, 7th ed., 2005.

[118] Satterfield, C. N. *Heterogeneous Catalysis in Industrial Practice;* 2nd ed., 1991.

[119] Choudhary, T. V.; Sivadinarayana, C.; Goodman, D. W. *Catal. Lett.* **2001**, *72*, 197.

[120] Yin, S. F.; Xu, B. Q.; Zhou, X. P.; Au, C. T. *Appl. Catal., A* **2004**, *277*, 1.

[121] Christensen, C. H.; Johannessen, T.; Sorensen, R. Z.; Nørskov, J. K. *Catal. Today* **2006**, *111*, 140.

[122] Crawford, P.; Hu, P. *J. Chem. Phys.* **2006**, *124*, 044705/1.

[123] Novell-Leruth, G.; Valcárcel, A.; Clotet, A.; Ricart, J. M.; Pérez-Ramírez, J. *J. Phys. Chem. B* **2005**, *109*, 18061.

[124] Offermans, W. K.; Jansen, A. P. J.; van Santen, R. A. *Surf. Sci.* **2006**, *600*, 1714.

[125] Stolbov, S.; Rahman, T. S. *J. Chem. Phys.* **2005**, *123*.

[126] Liu, Z.-P.; Hu, P.; Lee, M.-H. *J. Chem. Phys.* **2003**, *119*, 6282.

[127] Vidal-Iglesias, F. J.; García-Aráez, N.; Montiel, V.; Feliu, J. M.; Aldaz, A. *Electrochem. Commun.* **2003**, *5*, 22.

[128] Rosca, V.; Koper, M. T. M. *Phys. Chem. Chem. Phys.* **2006**, *8*, 2513.

[129] Wyckoff, R. W. G. *Crystal Structures;* Interscience: New York, 1965.

[130] Frechard, F.; van Santen, R. A.; Siokou, A.; Niemantsverdriet, J. W.; Hafner, J. *J. Chem. Phys.* **1999**, *111*, 8124.

[131] Papapolymerou, G.; Bontozoglou, V. *J. Mol. Catal. A: Chem.* **1997**, *120*, 165.

[132] Ample, F.; Ricart, J. M.; Clotet, A.; Curulla, D.; Niemantsverdriet, J. W. *Chem. Phys. Lett.* **2004**, *385*, 52.

[133] Mavrikakis, M.; Rempel, J.; Greeley, J.; Hansen, L. B.; Nørskov, J. K. *J. Chem. Phys.* **2002**, *117*, 6737.

[134] Mei, D.; Ge, Q.; Neurock, M.; Kieken, L.; Lerou, J. *Mol. Phys.* **2004**, *102*, 361.

[135] Rocca, M.; Lehwald, S.; Ibach, H.; Rahman, T. S. *Phys. Rev. B: Condens. Matter Mater. Phys.* **1987**, *35*, 9510.

[136] Olsen, R. A.; Kroes, G. J.; Baerends, E. J. *J. Chem. Phys.* **1999**, *111*, 11155.

[137] Pallassana, V.; Neurock, M.; Hansen, L. B.; Hammer, B.; Nørskov, J. K. *Phys. Rev. B: Condens. Matter Mater. Phys.* **1999**, *60*, 6146.

[138] Mitsui, T.; Rose, M. K.; Fomin, E.; Ogletree, D. F.; Salmeron, M. *Surf. Sci.* **2003**, *540*, 5.

[139] Dong, W.; Ledentu, V.; Sautet, P.; Eichler, A.; Hafner, J. *Surf. Sci.* **1998**, *411*, 123.

[140] Zinola, C. F.; Arvia, A. J. *Electrochim. Acta* **1996**, *41*, 2267.

[141] Hu, X.; Lin, Z. *Phys. Rev. B: Condens. Matter* **1995**, *52*, 11467.

[142] Lovvik, O. M.; Olsen, R. A. *J. Chem. Phys.* **2003**, *118*, 3268.

[143] Eichler, A.; Hafner, J.; Kresse, G. *J. Phys.: Condens. Matter* **1996**, *8*, 7659.

[144] Pauer, G.; Eichler, A.; Sock, M.; Ramsey, M. G.; Netzer, F.; Winkler, A. *J. Chem. Phys.* **2003**, *119*, 5253.

[145] Klein, C.; Eichler, A.; Hebenstreit, E. L. D.; Pauer, G.; Koller, R.; Winkler, A.; Schmid, M.; Varga, P. *Phys. Rev. Lett.* *90*, 176101.

[146] Kirsch, J. E.; Harris, S. *Surf. Sci.* **2003**, *522*, 125.

[147] Nørskov, J. K.; Bligaard, T.; Logadóttir, A.; Bahn, S.; Hansen, L. B.; Bollinger, M.; Bengaard, H.; Hammer, B.; Sljivancanin, Z.; Mavrikakis, M.; Xu, Y.; Dahl, S.; Jacobsen, C. J. H. *J. Catal.* **2002**, *209*, 275.

[148] Hammer, B. *Surf. Sci.* **2000**, *459*, 323.

[149] Ostwald, W. *Patent* **1908**, *GB 087909 19080409.*

[150] Fogel, Y. M.; Nadykto, B. T.; Rybalko, V. F.; Shvachko, V. I.; Korobchaskaya, I. E. *Kinet. Katal.* **1964**, *5*, 496.

[151] Nutt, C. W.; Kapur, S. *Nature* **1968**, *220*, 697.

[152] Scheibe, A.; Lins, U.; Imbihl, R. *Surf. Sci.* **2005**, *577*, 1.

[153] Scheibe, A.; Hinz, M.; Imbihl, R. *Surf. Sci.* **2005**, *576*, 131.

[154] Cortright, R. D.; Dumesic, J. A.; Academic Press, 2001; pages 161–264.

[155] Novell-Leruth, G.; Valcárcel, A.; Pérez-Ramírez, J.; Ricart, J. M. *J. Phys. Chem. C* **2007**, *111*, 860.

[156] Offermans, W. K.; Jansen, A. P. J.; van Santen, R. A.; Novell-Leruth, G.; Ricart, J. M.; Pérez-Ramírez, J. *J. Phys. Chem. C* **2007**, *111*, 17551.

[157] Imbihl, R.; Scheibe, A.; Zeng, Y. F.; Günther, S.; Kraehnert, R.; Kondratenko, V. A.; Baerns, M.; Offermans, W. K.; Jansen, A. P. J.; van Santen, R. A. *Phys. Chem. Chem. Phys.* **2007**, *9*, 3522.

[158] Popa, C.; van Santen, R. A.; Jansen, A. P. J. *J. Phys. Chem. C* **2007**, *111*, 9839.

[159] López, N.; García-Mota, M.; Gómez-Diaz, J. *J. Phys. Chem. C* **2008**, *112*, 247.

[160] Winkler, A.; Guo, X.; Siddiqui, H. R.; Hagans, P. L.; Yates, J. T. *Surf. Sci.* **1988**, *201*, 419.

[161] Honkala, K.; Hellman, A.; Remediakis, I. N.; Logadottir, A.; Carlsson, A.; Dahl, S.; Christensen, C. H.; Nørskov, J. K. *Science* **2005**, *307*, 555.

[162] Askgaard, T. S.; Nørskov, J. K.; Ovesen, C. V.; Stoltze, P. *J. Catal.* **1995**, *156*, 229.

[163] Greeley, J.; Mavrikakis, M. *J. Catal.* **2002**, *208*, 291.

[164] Kandoi, S.; Greeley, J.; Sanchez-Castillo, M. A.; Evans, S. T.; Gokhale, A. A.; Dumesic, J. A.; Mavrikakis, M. *Top. Catal.* **2006**, *37*, 17.

[165] Hansen, E.; Neurock, M. *J. Phys. Chem. B* **2001**, *105*, 9218.

[166] Mei, D.; Sheth, P. A.; Neurock, M.; Smith, C. M. *J. Catal.* **2006**, *242*, 1.

[167] Saeys, M.; Thybaut, J. W.; Neurock, M.; Marin, G. B. *Mol. Phys.* **2004**, *102*, 267.

[168] Reuter, K.; Frenkel, D.; Scheffler, M. *Phys. Rev. Lett.* **2004**, *93*, 116105/1.

[169] Ge, Q.; Hu, P.; King, D. A.; Lee, M. H.; White, J. A.; Payne, M. C. *J. Chem. Phys.* **1997**, *106*, 1210.

[170] Pignet, T.; Schmidt, L. D. *J. Catal.* **1975**, *40*, 212.

[171] Michaelides, A.; Hu, P. *J. Am. Chem. Soc.* **2001**, *123*, 4235.

[172] Eichler, A.; Hafner, J. *J. Catal.* **2001**, *204*, 118.

[173] Burch, R.; Daniells, S. T.; Hu, P. *J. Chem. Phys.* **2004**, *121*, 2737.

[174] Ge, Q.; Neurock, M. *J. Am. Chem. Soc.* **2004**, *126*, 1551.

[175] Yeo, Y. Y.; Vattuone, L.; King, D. A. *J. Chem. Phys.* **1996**, *104*, 3810.

[176] Shustorovich, E.; Bell, A. T. *Surf. Sci.* **1993**, *289*, 127.

[177] Andersson, M.; Holmgren, L.; Rosen, A. *Surf. Rev. Lett.* **1996**, *3*, 683.

[178] Golodets, G. I.; Elsevier ; Distributors for the U.S. and Canada Elsevier Science Pub. Co.: Amsterdam ; New York, N.Y. New York, 1983.

[179] Zaera, F.; Gopinath, C. S. *J. Chem. Phys.* **2002**, *116*, 1128.

Resum

Antecedents històrics

El terme "catàlisi" va ser introduït el 1836 per Berzelius per a descriure "*la propietat d'algunes substàncies per a despertar afinitats que estan dormides a una temperatura particular, només per la pròpia presència del catalitzador*" Avui en dia, la definició de catàlisi és la que proposà Ostwald (1894) basada en la velocitat de reacció: "*Catàlisi es l'acceleració d'una reacció precedent lenta gràcies a la presència d'una substància externa, que pot participar en la reacció però, que no es consumeix en la mateixa*".

La producció d'àcid nítric (Procés Ostwald; premi Nobel 1909) és un dels processos industrials més importants, conjuntament amb la síntesi d'amoníac (Procés de Haber-Bosh; premis Nobel 1918 i 1931, respectivament), la síntesi de Fisher-Tropsch, la polimerització Ziegler Natta; premis Nobel 1963) o l'oxidació de diòxid de sofre en la producció d'àcid sulfúric, entre d'altres.[1] El procés Ostwald va ser un dels primers processos catalítics introduïts a escala industrial.

La reacció d'oxidació d'amoníac fou descoberta i patentada per Kuhlmann el 1838,[2] però no és fins el 1906 quan Ostwald i Brauer van dissenyar una planta industrial aplicant-hi la reacció d'oxidació d'amoníac. Òbviament, aquest procés no hagués estat possible sense l'existència del procés Haber-Bosh, ja que un dels reactius del procés Ostwald és l'amoníac, el producte del procés anteriorment esmentat.

La primera etapa del procés Ostwald és l'oxidació catalítica d'amoníac, que és una de les reaccions químiques no explosives més ràpides i més estudiades que es coneixen. S'estima que el temps de contacte dels reactius (NH_3 i O_2) amb el catalitzador (Pt/Rh) és de tan sols 1 ms, obtenint-se NO, N_2, N_2O i H_2O.

El problema del procés original d'Ostwald era la gran quantitat de Platí necessària per a realitzar la reacció. Ben aviat, K. Kaiser, de la Technische Hochschule a Charlottenburg, patentà la utilització de xarxes de platí (gauzes) i, des de llavors, s'ha millorat el catalitzador utilitzant aliatges de Pt i Rh, tot i que també s'empra Pd per a recuperar el Pt que es perd durant el temps de vida del catalitzador.[3] Actualment, la composició és aproximadament d'un 95% de Pt i un 5% de Rh, encara que aquesta proporció pot variar amb el preu dels metalls al mercat internacional.

S'han dedicat molts anys a estudiar aquesta reacció, tant per millorar-la, com per entendre-la, com es pot veure reflexat en la bibliografia (Figura 1.3). Pels voltants de 1910, quan apareix el procés Ostwald, ja existeixen diverses publicacions, principalment sobre el desenvolupament de diferents catalitzadors que procuren millorar el procés. A partir dels anys 30 es millora el rendiment del catalitzador afegint una petita quantitat de rodi, concretament entre un 5 % i un 10 %.[3] Aquest descobriment el realitzà l'empresa DuPont (Hansforth i Tilley, 1934).[5] Des de llavors no s'ha variat la relació platí/rodi. Un altre punt interessant és la recuperació del platí que es perd durant la reacció, això va generar més publicacions per la dècada dels 60. Fins que no aparegueren les noves tècniques associades a la ciència de superfícies actual i els mètodes computacionals, no s'han tornat a incrementar les publicacions sobre aquesta temàtica. Així, cal destacar que és un procés que encara roman obert a la discussió, pels mecanismes proposats, per la millora del catalitzador, per les espècies intermèdies o per la simple comprensió de la reactivitat implicada.

Tots aquests estudis han aportat molta informació sobre el procés o parts d'aquest. En alguns casos aporten informació sobre el comportament del catalitzador, en d'altres sobre les possibles espècies adsorbides a la superfície o la cinètica de les reaccions implicades, etc. Destaquen tres tipus d'experiments. Els primers són els realitzats en ultra alt buit (UHV) que solen aportar informació de la naturalesa de les espècies adsorbides a la superfície, com els realitzats amb les espècies NH_x. Existeixen moltes tècniques englobades dintre d'aquest grup, com l'espectroscòpia de desorció tèrmica (TDS), espectroscòpia de pèrdua d'energia electrònica (EELS), espectroscòpia electrònica d'Auger (AES) o la difracció d'electrons de baixa energia (LEED), etc.[6–13] Aquestes tècniques normalment es realitzen sobre monocristalls, en condicions de ultra alt buit. Per aquesta raó, les dades obtingudes poden no ser extrapolables a les condicions industrials, encara que aporten una important informació de les espècies adsorbides i llur reactivitat en unes condicions determinades. El segon grup d'experiments a destacar són els realitzats en microreactors. Aquests experiments solen analitzar els productes de sortida en diferents condicions de temperatura, pressió i reactius d'entrada. Principalment s'han emprat per a conèixer el rendiment d'algun tipus de catalitzador. Les dades obtingudes es poden emprar per a ajustar un model cinètic com ha fet Rebrov *et al.*[14] Aquest experiment ens dóna informació sobre el comportament del catalitzador en funció de les variables d'operació del reactor. Finalment cal destacar la tècnica d'Anàlisi Temporal de Productes (TAP)[15–19] que com el seu nom indica, analitza els productes de sortida en funció del temps respecte a un pols de reactius a l'entrada del reactor. Aquesta tècnica aporta informació sobre la cinètica de reacció, ja que ja que te en compte els productes de sortida i la proporció d'aquests en funció del temps. Cada experiment n'explica una part del procés. Així, els experiments realitzats sobre cristalls en ultra alt buit (UHV) aporten informació sobre les espècies adsorbides i llur reactivitat, però ho fan en unes condiciones llunyanes a les que es troben en el procés industrial, que es realitza a pressió atmosfèrica o superiors i amb materials amorfs. L'existència d'aquesta diferència material i de pressió (anomenades "materials gap" i "pressure gap")[19,179] dificulta l'extrapolació dels resultats als processos reals. Altres mètodes com el "Temporalry Analisis of Products" (TAP) permeten l'estudi a pressions més altes però sense arribar a la pressió de treball dels reactors industrials (1-12 bar), tot i eliminar el GAP material, ja que pot emprar el mateix tipus de catalitzador industrial.[19] Els mètodes computacionals permeten estudiar els diferents processos que es produeixen a la superfície del catalitzador, podent conèixer la reactivitat de cada espècie sobre la superfície, i determinar els estats de transició. Així, es poden estudiar tots el possibles camins de reacció, i discriminar el camí de mínima energia per a cada etapa de la reacció global. És equivalent a disposar dels fotogrames importants de la pel·lícula del procés sobre un model de superfície. El model de superfície és generalment un cristall ideal, amb què no s'elimina el gap material. De fet, amb els mètodes de càlcul i la potència dels ordinadors actuals es podria generar un model més proper al catalitzador real, nogensmenys amb un elevat cost computacional, lluny dels objectius d'aquesta tesi.

La reacció d'oxidació d'amoníac és molt complexa, pel gran nombre de variables implicades, entre elles la superfície del catalitzador. Durant el procés la composició del catalitzador va canviant, ja que es perd Pt i s'enriqueix en Rh (segregació). Aquest canvi químic comporta un canvi físic, un augment de la l'àrea superficial fins la formació de col-i-flors.[4] Segons la composició tenim unes activitats, unes selectivitats i unes conversions determinades. Una altra variable a tenir en compte són les condicions de reacció, ja que segons la temperatura o les pressions parcials dels reactius, obtindrem uns productes o altres.

A causa de la complexitat de la reacció, qualsevol experiment al respecte ens donarà informació esbiaixada del funcionament de la reacció. Els mètodes computacionals ens donen una informació basada en un model, així que els resultats obtinguts també son dades limitades al model. L'oportunitat que ens brinden els mètodes DFT és la possibilitat de dissenyar tots els models necessaris per a definir tots els moments del procés, podent afegir totes les diferents variables anomenades anteriorment.

Com ja s'ha comentat inicialment amb l'anàlisi de les publicacions, es porta molt de temps investigant l'oxidació d'amoníac. Les tècniques emprades per a conèixer el procés d'oxidació d'amoníac tenen les seves avantatges i desavantatges. Per aquest motiu encara roman obert a debat com transcorre la reacció. Un dels debats oberts és el mecanisme de reacció. Durant molts anys s'han mantingut tres possibles mecanismes per a descriure el procés. En aquesta tesis s'han estudiat els tres possibles mecanismes, com veurem més endavant.

1. Mecanisme del nitroxil (HNO), descrit per Andrussow:[21]
   - $NH_3 + O_2 \rightarrow HNO(a) + H_2O$
   - $2\ HNO(a) + 1/2\ O_2 \rightarrow 2\ NO + H_2O + 2\ *$
   - $HNO(a) + NH_3 \rightarrow N_2H_4(a) + H_2O$
   - $N_2H_4(a) + 1/2\ O_2 \rightarrow 2\ N_2 + H_2O + *$
   - $HNO_3(a) + NH_3 \rightarrow NH_4NO_3(a)$
   - $NH_4NO_3(a) \rightarrow N_2O + 2\ H_2O + *$
2. Mecanisme de la hidroxilamina (NH_2OH), descrit per Bodenstein:[22]
   - $NH_3 + O(a) \rightarrow NH_2OH(a)$
   - $NH_2OH(a) + O_2 \rightarrow HNO_2(a) + H_2O$
   - $HNO_2(a) + O_2 \rightarrow HNO_4(a)$
   - $HNO_4(a) \rightarrow NO + O_2 + OH(a)$
   - $NH_2OH(a) + O(a) \rightarrow HNO(a) + H_2O + *$
   - $NH_2OH(a) + HNO(a) \rightarrow N_2 + 2\ H_2O + 2\ *$
   - $HNO(a) + HNO(a) \rightarrow N_2O + H_2O + 2\ *$
3. Mecanisme de la imida (NH), descrit per Raschig i Zawadzki:[23, 24]
   - $NH_3 + O(a) \rightarrow NH(a) + H_2O$
   - $NH(a) + O(a) \rightarrow HNO(a) + *$
   - $NH(a) + NH_3 \rightarrow N_2H_4(a)$
   - $HNO(a) + NH_3 \rightarrow N_2H_4(a) + 1/2\ O_2$
   - $N_2H_4(a) + O_2 \rightarrow N_2 + 2\ H_2O + *$

Objectius

Els objectius que s'han abordat en aquesta Tesi són els següents:

1. Estudi estructural de l'adsorció de les espècies NH_x (x=0-3) sobre les superfícies (100) i (111) de platí. Aquest estudi inclou la geometria i el lloc d'adsorció, les propietats electròniques, la influència del recobriment i l'estabilitat relativa de les espècies.

    (a) Estudi de l'efecte de la temperatura i la pressió sobre l'adsorció d'amoníac sobre Pt(100) i Pt(111).
    (b) Anàlisi espectroscòpic de les espècies NH_x (x=0-3) adsorbides sobre Pt(100) i Pt(111).
    (c) Estudi de la reacció de dissociació de les espècies NH_x (x=0-3) sobre les superfícies anteriors.

2. Estudi comparatiu de la deshidrogenació d'amoníac sobre les cares (100) i (111) de platí, rodi i pal·ladi. Es fa èmfasi sobre la determinació de constants de velocitat de les diferents etapes.

3. Estudi de l'oxidació d'amoníac sobre Pt(100).

    (a) Caracterització de totes les especies adsorbides (NH_3, NH_2, NH, O, OH, H_2O, NH_2OH, HNO, NOH, N_2, NO, N_2O).
    (b) Estudi de la deshidrogenació amb oxigen adsorbit.
    (c) Estudi de la deshidrogenació amb hidroxil adsorbit.
    (d) Comparació amb els resultats sobre la superfície (111).
    (e) Anàlisi de la viabilitat dels mecanismes proposats a la bibliografia.
    (f) Estudi dels productes finals de reacció (NO, N_2, N_2O, H_2O).
    (g) Anàlisi microcinètic del procés global i identificació de les etapes limitants.

Aquest és el contingut fonamental d'aquesta tesi, però com en tot, hi ha un moment per acabar i queden punts oberts. Resta pendent finalitzar l'estudi sobre rodi i aliatges Pt-Rh, de composició variable, que ens aproparien més al procés industrial. També es podrien traslladar els resultats a un model de reactor, per a conèixer com transcorren les reaccions dins del reactor i millorar-ne llur disseny. També es podria simular els experiments TAP per a aprofundir en el coneixement d'aquesta tècnica i de facilitar l'anàlisi dels resultats. Encara

UNIVERSITAT ROVIRA I VIRGILI
CATALYTIC AMMONIA OXIDATION ON NOBLE METAL SURFACES: A THEORETICAL STUDY
Gerard Novell Leruth
ISBN:978-84-692-1534-0/ DL:T-377-2009

queda molt camí per a recórrer, no solament amb treballs teòrics, també experimentals. La finalitat d'aquesta tesi és donar un pas endavant per a entendre i millorar el procés d'oxidació d'amoníac.

Conclusions

Utilitzant càlculs basats en la teoria del funcional de la densitat, hem calculat les geometries, llocs d'adsorció, i l'estabilitat relativa de l'amoníac adsorbit, així com dels seus fragments deshidrogenats (NH_2, NH, N) sobre les cares (100) i (111) del platí, rodi i pal·ladi. L'energia d'adsorció és més elevada sobre el pla més obert (100) que sobre el pla més compacte (111) per a tots els metalls. A més, les energies d'adsorció són més grans sobre rodi que sobre pal·ladi o platí. A les sis superfícies, el NH_3 s'adsorbeix a la posició top, el NH_2 sobre la posició bridge i el NH i el N ho fan sobre la posició hollow. Les distancies N-H i M-N són similars per a totes les espècies. Les diferències entre els diferents metalls son més significatives sobre la cara (100) que sobre la cara (111). S'han determinat els estats de transició i les barreres de reacció per als successius passos de la deshidrogenació d'amoníac. Les barreres de reacció es troben entre els 67 $\mathrm{kJ \cdot mol^{-1}}$ ($NH_3 \rightarrow NH_2 + H$ sobre Rh(100)) i 118 $\mathrm{kJ \cdot mol^{-1}}$ ($NH \rightarrow N + H$ sobre Pd(100)). Com a tendència general, les barreres són més altes per a l'últim pas de la deshidrogenació, excepte per al Pt(100). Tanmateix, una vegada calculades les constants cinètiques, l'etapa limitant de la velocitat de reacció correspon a l'abstracció del primer hidrogen de l'amoníac (amb l'excepció de Rh(100)) a causa de l'entropia d'activació negativa d'aquesta etapa. En Pd(111) i Pt(111) tots els estats de transició estan per sobre de l'energia del NH_3 en la fase de gas, mentre que en Rh(111) totes les espècies són més estable que l'amoníac adsorbit. A les cares (100), les energies de les diferents espècies adsorbides, intermedis de reacció i estats de transició són més altes sobre platí i pal·ladi que sobre rodi. En el cas del rodi, tots els estats de transició estan per sota l'energia del NH_3 en la fase de gas. Així, segons els nostres càlculs, el Rh hauria de ser el catalitzador més actiu per a la descomposició de l'amoníac, per sobre del Pt o Pd. Això concorda i ratifica els resultats experimentals de la literatura.

El mecanisme d'oxidació d'amoníac sobre Pt(100) també s'ha investigat en detall. El procés es realitza a través del mecanisme de la imida, pel qual l'amoníac és deshidrogenat successivament per l'oxigen atòmic. Comparativament, els altres mecanismes proposats, com el mecanisme de nitroxil o de la hidroxilamina com a intermedis de reacció són termodinàmicament desfavorables. L'abstracció oxidativa del primer protó de l'amoníac és el pas més lent en la deshidrogenació del NH_3. La natura de l'espècie oxidativa per a la deshidrogenació de les espècies NH_x (O per a Pt(100) i OH per a Pt(111)) està determinada per la topologia de platí, a causa del repartiment dels àtoms de la superfície i de l'estabilitat del NH_2 i el OH. La formació de N_2, NO i N_2O transcorre per les reaccions elementals de N+N, N+O i N+NO, respectivament. L'aigua es forma per la recombinació d'OH, regenerant un O actiu. Tant la formació del N_2 com el NO tenen barreres baixes i són reaccions exotèrmiques, en canvi la formació de N_2O és una reacció endotèrmica i conseqüentment té una barrera més alta. Una vegada s'ha format el NO, la barrera de desorció és extremadament alta, convertint-se en el pas que determina la velocitat de reacció del procés global. S'ha obtingut un mecanisme de reacció simplificat, derivat del càlcul dels coeficients de velocitat de reacció de les diferents etapes elementals, permetent una anàlisi microcinètic del procés. El nostre model microcinètic pronostica bé la distribució de productes obtinguda experimentalment a diferents temperatures, temps, i relació d'entrada de O_2/NH_3.

En aquesta tesi queda patent que el model microcinètic és el primer pas per a enllaçar el treball teòric amb els experimentals, encara que és necessari arribar a la simulació del reactor per a poder comparar d'una manera més efectiva les dades teòriques amb les dades experimentals o viceversa. També podem afirmar que els treballs teòrics són una eina necessària per a entendre les reaccions a nivell molecular, éssent una eina complementària per a entendre els mecanismes de reacció de molts treballs experimentals, car aporten una informació extra que no s'obté directament de les dades experimentals.

Aquesta tesi ha aportat un nou punt de vista a la reacció d'oxidació d'amoníac. Tampoc hem resolt totes les qüestions que romanen obertes, no n'era l'objectiu, però sí a assentat les bases per un futur treball. Aquest treball continua amb l'estudi sobre rodi i els aliatges (Pt/Rh), ja que el catalitzador industrial té aquesta composició. Els aliatges presenten complicacions, car el nombre de combinacions de situacions reactives inicials pot ser molt gran. Una manera de simplificar el model per reduir el cost computacional és substituir algun/s àtom/s de la superfície de platí per rodi. Tanmateix, s'hauria de comprovar l'efecte que pot tindre el rodi en el bulk i a la superfície en diferents proporcions i profunditats. Altres consideracions a tindre en compte serien l'estudi de la segregació Pt/Rh, així com el mecanisme pel qual es volatilitza el platí de la superfície durant el procés. Un altre punt a seguir és l'extrapolació de les dades microcinètiques, com les presentades a la tesi, a un model de reactor. Un model computacional de fluid dinàmic (CFD) pot ser una bona eina per a entendre els efectes del disseny del reactor. Aquesta via obre un camí molt ampli, com la comparació de dades experimentals, àdhuc millorar el disseny del reactor, etc. Tanmateix, tant pot servir per a entendre els resultats experimentals com per a reafirmar les dades teòriques. Encara que les dades siguin sobre un model concret, allunyat de la realitat, poden aclarir el coneixement del comportament molecular de les observacions experimentals. Per a aproximar-se a la realitat es pot combinar diferents models. Si l'estudi es realitza sobre diversos models (diferents metalls, cares i defectes), es poden combinar en una proporció adequada. Aquesta proporció es podria obtenir per un anàlisi de sensibilitat amb les dades experimentals, coneixent-se quin model és el que té un major pes o quines reaccions són les més importants. En un futur podria ser una manera de procedir, ja que podríem saber quin és el model més adequat per realitzar l'estudi computacional.